Università Degli Studi di Napoli Federico II

Dottorato di Ricerca in Fisica Fondamentale ed Applicata
18°ciclo

Dott.ssa Virginia D'Auria

Dynamics and Behaviour of Triply Resonant OPOs below the threshold

Il coordinatore
Prof. **Arturo Tagliacozzo**

Novembre 2005

Acknowledgments

My deep gratitude is addressed to my Advisor, Prof. Salvatore Solimeno for his continuous support in the research work undertaken in this thesis. Continuous, stimulating and lively discussions with him have been precious for my professional and human growth. I'm grateful to Alberto Porzio and Matteo G.A. Paris, for their intensive supports and exchanges since the very beginning of my work. Their professional advises but also their great kindness have been strongly encouraging and helped me to overcome many difficulties.

I would like to thank Antonino, Maddalena, Iolanda, Martina, Fabio G., Genni and Simona; they have been first of all friends more than simple colleagues.. I'll always feel very grateful for their constant and patient help in running my bad moods as well as my good days.

Eventually, I wish to express my gratitude to Raffaele Rocco and the technicians of the mechanical workshop and to Bruno Piccirillo from the non linear optics laboratory. Their gentleness and helpfulness have been crucial in many "experimental emergencies".

Introduction

For a monochromatic plane wave oscillating at frequency ω, the electric field can be decomposed in two *quadrature* components: one with the time dependence $\cos \omega t$ (*amplitude quadrature* X) and the other one with $\sin \omega t$ (*phase quadrature* Y). These quantities represent the analogous for the electromagnetic field of the position and momentum of a mechanical oscillator.

Due to quantum nature of light, the precision relative to a quadratures measurement is intrinsically limited. For classical light beams, as generated by a laser source, the fluctuations on the two quadratures are equal to each other and minimize the uncertainty product given by Heisenberg's relation. The corresponding quadrature noise is called *standard quantum limit* (SQL) since it represents the minimum optical noise allowed by quantum mechanics for classical light. Heisenberg relation only states a lower bound to the variance product with no restriction to the single quadrature noise. In principle, one of the field quadrature can have reduced quantum fluctuations at expense of a noise enhancement of the other one so to satisfy the uncertainty relation. When the light fluctuations are distributed in such an asymmetric manner, the e.m.field is said to be in a *squeezed state*. Since the quadratures can be distinguished by introducing a suitable phase, the squeezing is a phase-dependent property. It offers the possibility of beating the SQL affecting traditional optical measurements, by performing phase-sensitive measurements using only the quadrature with reduced quantum fluctuations.

The generation of squeezed state requires a non linear phase-dependent interaction. First experimental realization of squeezing was obtained in 1985 by R.E. Slusher by means of four waves mixing in atomic sodium [1] . Since then many experiments have been performed by and parametric interaction in a non-linear crystal has been theoretically shown to be a very efficient source of nonclassical states of light ([2] , [3] , [6] , [7] , [8]).

Among non linear processes, the most versatile for generating squeezed light is parametric down-conversion [2] . In this case a *pump* photon at frequency ω_p splits in

two photons at different frequencies ω_s and ω_i (*signal* and *idler*) such that $\omega_p = \omega_i + \omega_s$. The effect is called *parametric fluorescence*, the spontaneous emission being driven by the vacuum fluctuations of the e.m. field. Signal and idler photons are produced in pairs, and show strong correlation of energy and momentum.

Light emission in down conversion can be enhanced by using a classical beam of frequency ω_s (*seed*) to assist the pump action inside the non linear crystal. In this way the emission at ω_s is strongly stimulated and the input beam undergoes amplification. Due to the pair production in down conversion, an intense idler beam also appears. This effect is known as optical parametric amplification (OPA). If the active medium is put into an optical cavity, under appropriate conditions, the parametric interaction can overcome the effect of possible losses (i.e. absorption, diffraction..). In this case the system undergoes an oscillation and intense output beams are obtained without any injected seed. Such a device is called an Optical Parametric Oscillator (OPO). The OPO introduces a threshold condition; for pump intensity above a certain value, bright signal and idler beams will be generated (*twin beams*), otherwise no macroscopic beams are emitted. Experimentally the threshold can be lowered by setting the cavity to simultaneously resonate on the signal, the idler and the pump beam (*triply resonance condition*).

Twin beams generated by above threshold OPOs exhibit non classical noise reduction in the intensity difference ([9] , [10] , [11] , [12] and [13]). The spectrum difference of the two beams is shaped like a Lorentzian with noise suppression below the classical value at zero frequency and within a bandwidth of the order of cavity linewidth. Following the seminal idea highlighted in Re.. [9] , twin beams have been used to enhance performances of optical setup for spectroscopy ([14] , [15] , [16]).

In this thesis are discussed the cases of OPOs working below threshold and generating signal and idler photons with the same frequency ($\omega_s = \omega_i$, *frequency degeneration*) [2] .

Much interest is paid to unseeded OPOs working in *degeneration* (DOPO), say emitting signal and idler with both the same polarizations and frequencies. In this case, the two generated beams are not distinguishable and collapse into a single one; never-

theless, the mark of quantum correlation is still somehow visible and this unique beam exhibits squeezing in one of its quadrature. Since it is generated by processing an input vacuum state, the light state for the output of a DOPO is referred to as a *squeezed vacuum state* [17] .

Vacuum squeezed light has found many applications in enhancing the performances of traditional optical devices. C.M.Caves first proposed to combine coherent and squeezed vacuum radiation for overcoming the quantum limit in gravitational wave antennas [18] . Following this original suggestion Grangier et al. [19] up-graded a polarization interferometer by injecting a squeezed vacuum through an empty port. By choosing the phase of the squeezed light so that the quantum fluctuation entering the empty port were reduced below the SL, they observed an enhanced visibility of the interference fringes. In 1992, Polzik et al. [20] provided stunning evidence that a gain of some dB over the standard quantum limit can be achieved in the resonant interaction of atoms with squeezed light. Their experiment was performed by combining in a well defined phase relation a coherent field with the output of an optical parametric amplifier.

Due to its interest for application, the DOPO have been the subject of many experimental and theoretical works ([21] , [22] , [23] , [7]). The features of an OPO depend on several parameters, namely, cavity damping coefficients, degree of excitation below threshold, spurious losses, deviation from resonance condition (detuning), and pump amplitude/phase fluctuations. Many theoretical model have investigated the effect of all these factors on the emitted squeezed radiation ([21] , [9]). In particular when extralosses (due to crystal absorption, diffraction etc.) are present in the OPO cavity, it has been shown that its output state is not a pure vacuum squeezed and does not show minimum uncertainty on the quadrature product [21] . Much attention has also been paid to phase transition from below to above threshold regime [24] and to the region very close to threshold [25] , showing, under limiting conditions, the importance of non linear contribution to the dynamic of the system.

In the first part of the thesis, these thematics are reproposed by performing and analyzing, in proximity of the threshold, squeezed vacuum measurements relative to dif-

ferent OPO cavity conditions with continuous waves (CW) radiation. Being a critical point, the OPO threshold is strongly unstable for its own nature; moreover, it is affected by residual noises on experimental parameters that determine its value. The effect of threshold fluctuations on the statistic of the output beam is analyzed, highlighting deviations from the Gaussian behaviour expected for ideal squeezed vacuum state. These deviations are experimentally observed by means of tomographic reconstruction of the state together with a direct measurement of the quadrature distributions [26] . Starting from the characteristics of the used experimental set-up, it is proposed a theoretical model to reproduce the observed behaviour as a function of both OPO and detection parameters.

With regard to application of squeezed light, a method for measuring the transmittivity of optical samples is illustrated [27] . In this scheme a squeezed vacuum field generated by a below–threshold OPO is propagated through a nondispersive medium and its quadratures are detected; the variance of the detected quadratures are used for measuring the transmittivity. With this method it is drastically reduced the number of photons passing through the sample during the measurement interval, so providing an useful tool for measuring the transmittivity of highly photosensible materials. The results of some experimental tests performed to assess the scheme feasibility are reported.

The photons pair generated in parametric down conversion also carry quantum correlations of the Einstein-Podolsky-Rosen type [28] . First suggestion along this direction, dates from the end of the 1980s, when Reid and Drummond pointed out the possibility of demonstrating the EPR paradox via quadrature-phase measurements on the beams outing a non degenerate parametric amplifier (NOPA) [29] . In this case, the two beams originating from the pump photon splitting, can be distinguished because of their polarization and in turn spatially separated. Due to quantum correlation, both the beams are needed to see the squeezing effect so that their state is usually referred to as a *two modes squeezed state*. Under limiting conditions the quadratures of the output beams become quantum copies of one other so that the results for the signal quadratures can be inferred by probability 1 from the measurement of the idler's ones.

An experimental demonstration of the EPR paradox with continuous variables refers to Kimble in 1992 ([30] , [31]) .

In developing quantum information science, nonlocal quantum entanglement plays a determining role ([32] [33] [34]). Unconditional quantum teleportation has been demonstrated by using continuously entangled EPR pairs resulting from two-mode squeezed vacuum states [35] . The dense coding for continuous variables has been experimentally demonstrated [36] on bright EPR beams with anticorrelation of amplitude quadratures and correlation of phase quadratures, generated from a seeded NOPA operating at deamplification. Many cryptographic schemes for secure information sharing have been proposed and experimentally realized [37] , [38] [39] . In these scheme, informations are written on the signal (usually by means of phase/amplitude modulation); the entanglement permits to check by observing the idler beams if any eavesdropping attempt has been performed.

Besides mean values of the field operators, the most relevant quantity needed to characterize an EPR state is its covariance matrix $\boldsymbol{\sigma}$ [40] . The form of this matrix gives reason of the involved kind of entanglement and the mutual correlation degree between the interested observable pair. Once the covariance matrix is known the entanglement of the state can be evaluated and, in turn, the performances of the state itself as a support for quantum information protocols. Moreover since entanglement is generally corrupted by the interaction with the environment it becomes crucial to establish whether or not it has survived the environmental noise. As a consequence, besides being of fundamental interest, a simple characterization technique for bipartite states is needed for experimentally check the accessible entanglement in a noisy channel ([41] , [42] , [43] , [44]) as well as the corresponding state purity and nonclassicality ([45] , [46]).

The second part of the thesis is devoted to the NOPA analysis and its realization.

It is proposed a novel scheme for measuring $\boldsymbol{\sigma}$ for the NOPA output by means of a single quadrature detector plus a polarizing beam splitter (PBS) and a polarization rotator ($\lambda/2$) [47] . By means of the system $\lambda/2$+PBS, beside the signal and idler modes, some linear combinations of them are selected for detection. Moreover together with the

quadrature X and Y, also their rotation by $\pm\pi/4$ are measured. By introducing these extra quantities in is possible to express $\boldsymbol{\sigma}$ as the sum of the variances for the single modes quadratures. This scheme can be used to fully characterize bipartite Gaussian states and to extract relevant informations on generic states.

The experimental implementation of a NOPA is eventually discussed in the last part of the thesis.

Since the degree of EPR correlation is linked to the distance from threshold, in experimental realization, threshold must be stabilized as much as possible. This suggests the use of low noise sources as the Nd:YAG (@1064nm) diode pumped and frequency duplicated lasers able to minimized pump laser residual noise. At the same time, to generate cross polarized idler and signal beams type II crystals are required.

For the KTP [48] , the type II crystal with the best optical performances, the frequency degeneration condition for pump at 532nm (Nd:YAG second harmonic) corresponds to cryogenic working temperatures. In order to avoid this problem, the NOPA implementations has been based up to now on custom laser sources or custom crystals ([49]). In this thesis it is proposed an alternative and more convenient experimental set up based on the use of a Nd:Yag source together with a periodically poled KTP crystal (PKTP) [50] . PKTP can be designed to set the frequency degeneration at a desired temperature, in the present case $T_{\mathrm{deg}} \approx 35^{\circ}C$. First tests on the crystal and measurement of the actual T_{deg} are reported and discussed.

The thesis is structured as follows.

In the first chapter the theory of parametric amplifiers degenerate and non degenerate is provided, to show the squeezing properties of the output beams.

In the second chapter the case of degenerate parametric oscillator below threshold is discussed and it is provided an alternative description for the output state, taking into account the effect of OPO detuning and extra losses.

In the third chapter the technique for quadrature detection and the basics of quantum state tomography are discussed.

The following three chapters (4th, 5th and 6th) are devoted to DOPO experimental realization and relative results. In particular, the experimental setup together with the homodyne detector are presented in a detailed manner in chapter 4. Chapter 5 is devoted to the study both experimental and theoretical of the deviation from Gaussianity observed close to threshold. Eventually chapter 6 reports the discussion of accuracy and reliability absorption measurement based on squeezed vacuum, together with relative experimental results.

Chapter 7 and 8 concern with the NOPA theory and realization. In the 7th chapter the theory of seed NOPA is illustrated together with its application in measurement of bipartite state covariance matrix. In the last chapter the principle of poled crystal are reported and the first experimental results are discussed.

Chapter 1:
Introduction to non linear optical phenomena and squeezed light

Non linear optical phenomena occur when a material system, usually a crystal, responds in a non linear manner to the presence of light. More specifically it can be considered the dipole moment per unit volume, or polarization $P(t)$ and its dependence on the amplitude $E(t)$ of the applied optical field. In linear optics $P(t)$ depends upon the electric field as:

$$P(t) = \chi^{(1)} E(t) \tag{1.1}$$

being the constant of proportionality $\chi^{(1)}$ the linear susceptibility. In non linear optics, the optical response is described by generalizing Eq. (1.1) and expressing $P(t)$ as a power series of $E(t)$ as:

$$P(t) = \chi^{(1)} E(t) + \chi^{(2)} E^2(t) + \chi^{(3)} E^3(t) + ..$$

The term $P^{(i)}(t) \equiv \chi^{(i)} E^i(t)$ is the i^{th}-order induced polarization and $\chi^{(i)}$ ($i \geq 2$) the non linear optical susceptibilities. Macroscopically, when a light beam at frequency ω_p is sent to a non linear crystal, beside a beam at the same frequency, originate other light beams at different frequencies (for instance multiple or submultiple of ω_p) depending on the amplitude of $\chi^{(i)}$ coefficient.

Among $\chi^{(2)}$ processes, an interesting case is that of the difference frequency generation, also known as *parametric down conversion* [1] [2] . A strong beam E_p at frequency ω_p and a weak beam E_s at frequency ω_s (*seed*) are injected into the non linear crystal. Due to non linear effect, the two fields "mix" inside the crystal and a macroscopic wave

[1] The parameter is represented by the non linear interaction strenght expressed by $\chi^{(2)}$ coefficient.

at frequency $\omega_i = \omega_p - \omega_s$ is generated by the induced $P^{(2)}$ polarization:

$$P^{(2)}(\omega_p - \omega_s) = 2\chi^{(2)} E_p E_s^*$$

The applied field E_p is called *pump* beam, the generated beams respectively *signal (E_s)* and *idler (E_i)*.

From the quantum point of view, the entire process can be depicted according to the photon energy-level description. Due to absorption of a photon at frequency ω_p an atomic virtual level is excited. This level decays by a two photon emission process that is stimulated by the presence of ω_s field.

Two photon spontaneous emission occurs even if the ω_s-field is not applied. In this case the pump energy is spread over more signal/idler pair so that the generated fields are very much weaker. To obtain macroscopical signal and idler beams without any initial seed, the down conversion process is usually enhanced by placing the crystal in an optical resonator. By setting the device into resonance at the desired frequencies ω_s and/or ω_i, a selective feedback is applied, thus consenting to build up the fields E_s and/or E_i to large values. Such a device is known as *Optical Parametric Oscillator* (OPO).

1.1 Non linear Hamiltonian

A simple mathematical quantum description of non linear phenomena can be given for the crystal without the optical resonator. In this case, since no oscillations at all, but only single pass phenomena occur, the system acts as a *parametric amplifier*; by pumping the crystal with a beam at ω_p, an input seed at ω_s is amplified.

Parametric down conversion process can be schematically depicted as the annihilation of a (pump) photon at frequency ω_p, into two photons at frequency ω_s and ω_i. The energy and momentum conservation require the generated photons to satisfy the

relations:

$$\begin{aligned} \omega_p &= \omega_s + \omega_i \\ \vec{k}_p &= \vec{k}_s + \vec{k}_i \end{aligned} \tag{1.2}$$

where $\vec{k}_\xi$ are the wave vector[2] for the ξ-field.

The Hamiltonian $\mathcal{H}_{NL}$ describing the quantum evolution of the involved fields can be written as [3] :

$$\mathcal{H}_{NL} = \sum_\xi \hbar\omega_\xi a_\xi^\dagger a_\xi - i\hbar\chi^{(2)}\left(a_p a_s^\dagger a_i^\dagger - a_p^\dagger a_s a_i\right) \tag{1.3}$$

with a_ξ the bosonic annihilation operator for the electromagnetic field ξ-mode ($\xi = p, s, i$) oscillating at frequency ω_ξ with $[a_\xi, a_l] = 0$ and $\left[a_\xi, a_l^\dagger\right] = \delta_{\xi,l}$. Hamiltonian $\sum_\xi \hbar\omega_\xi a_\xi^\dagger a_\xi$ describes the three independent harmonic oscillators describing the free evolution for the involved modes. Non linear interaction Hamiltonian $-i\hbar\chi^{(2)} a_p a_s^\dagger a_s^\dagger + h.c.$ expresses the non linear process of annihilation of a pump photon into two signal and idler photons.

In many cases, the pump beam is a strong coherent one provided by a laser source. For weak $\chi^{(2)}$ interaction the pump amplitude is not significantly depleted by photon conversion in non linear interaction. This allows substituting the bosonic operator a_p with a classical field amplitude A_p. This approximation is valid in the limit

$$\chi^{(2)}\tau \to 0, \quad A_p \to \infty, \qquad \chi^{(2)}\tau\, A_p = constant$$

being τ the interaction time with the non linear medium [51] .

[2] Relations (1.2) express the conditions for constructive interference of the fields generated by the atomic dipoles stimulated by the pump through the crystal.

1.2 Degenerate Parametric Amplifier

Modes a_s and a_i can in principle have different frequencies and electric field polarizations. If they share the same frequency ($\omega_p/2$) and polarization, the system is said to work in *degeneration* condition. In this case the two fields are no longer mutually distinguishable and collapse into a single one (a) exhibiting the common polarization and frequency. The Hamiltonian (1.3) reduces to:

$$\mathcal{H}_{NL} = \hbar\frac{\omega_p}{2}a^\dagger a - i\hbar\frac{\chi^{(2)}}{2}A_p\left(a^{2\dagger} - a^2\right) \tag{1.4}$$

corresponding to the Heisenberg equations:

$$\begin{aligned}\frac{da}{dt} &= \frac{1}{i\hbar}\left[a, \mathcal{H}_{NL}\right] = \mathcal{E}\ a^\dagger \\ \frac{da^\dagger}{dt} &= \frac{1}{i\hbar}\left[a^\dagger, \mathcal{H}_{NL}\right] = \mathcal{E}\ a\end{aligned} \tag{1.5}$$

where $\mathcal{E} = \chi^{(2)}A_p$.

Most interesting results concern with the field quadrature $X_\theta = \frac{1}{2}\left(e^{i\theta}a^\dagger + e^{-i\theta}a\right)$. Because of commutation relation for a, each pair of orthogonal quadratures X_θ and $X_{\theta+\pi/2}$ satisfies:

$$\left[X_\theta, X_{\theta+\pi/2}\right] = \frac{i}{2}$$

Quadrature corresponding to $\theta = 0$ and $\theta = \pi/2$ are known respectively as *amplitude* (X) and *phase quadrature* (Y). In terms of X and Y equations (1.5) diagonalize into:

$$\frac{dX}{dt} = \mathcal{E}X \qquad \frac{dY}{dt} = -\mathcal{E}Y \tag{1.6}$$

Equations (1.6) demonstrate that the parametric amplifier is *phase sensitive*: it amplifies or de-amplifies the quadratures depending on their phase θ. At the crystal output X and Y become:

$$X(\tau) = e^{\mathcal{E}\tau}X(0);\ Y(\tau) = e^{-\mathcal{E}\tau}Y(0)$$

with $X(0)$ and $Y(0)$ the input field quadrature and τ the interaction time inside the crystal.

The parametric amplifier also acts on the quadrature noise. It is interesting to consider the case of a seed initially in a coherent state with quadrature variances $\Delta X(0)^2 = \Delta Y(0)^2 = 1/4$ corresponding to the *shot noise* level. This case accomplishes for both a seed from a laser source (seed in a bright coherent state [2]) and no seed at all (seed in a coherent vacuum state). For the output beam one has:

$$\Delta X(\tau)^2 = \frac{1}{4}e^{2\mathcal{E}\tau};\ \Delta Y(\tau)^2 = \frac{1}{4}e^{-2\mathcal{E}\tau} \tag{1.7}$$

It is worth observing that the quadrature variance product is:

$$\Delta X(\tau)^2 \Delta Y(\tau)^2 = \frac{1}{16}$$

thus showing that the state inherits from the input one the property of a minimum uncertainty for the quadrature variance product.

Equations (1.7) show that there is a reduction, or *squeezing*, of phase quadrature fluctuations below the shot noise level $1/4$. A corresponding enhancement of the amplitude quadrature fluctuations (anti-*squeezing*) is required by Heisenberg uncertainty relation. Since only one field is generated by non linear interaction the degenerate parametric amplified is a source of *one mode* squeezing.

The squeezing size $\mathcal{E}\tau = \chi^{(2)}A_p\tau$ depends on the non linearity of the crystal (via $\chi^{(2)}$), on the pump amplitude (via A_p) and on the interaction time (τ). Once $\chi^{(2)}$ is assigned by the choice of the non linear crystal, an enhancement of the squeezing is obtained by increasing A_p and τ. In particular the interaction time is usually raised by the use of the resonant cavity.

Other squeezed state properties can be described by introducing the evolution operator linked to the field Hamiltonian:

$$S(r) = \exp\left[\frac{r}{2}\left(a^2 - a^{\dagger 2}\right)\right]$$

with $r = \mathcal{E}\tau$. The mean value of the operator under scrutiny can be obtained by applying $S(r)$. In particular for an initial coherent state described by the projector $|A\rangle\langle A|$, the state density matrix for the squeezed state is:

$$\rho(r) = S(r)\,|A\rangle\langle A|S^{\dagger}(r)$$

Correspondingly the number operator $n = a^{\dagger}a$ and its variance $\Delta n^2 = (n - \langle n\rangle)^2$ are readily calculated to satisfy relations:

$$\begin{aligned} \langle n\rangle &= \sinh^2 r + |A|^2 \\ \left\langle \Delta n^2 \right\rangle &= |A\cosh r - A^{*}\sinh r|^2 + \frac{1}{2}\sinh^2 2r. \end{aligned}$$

If the system is initially in a coherent vacuum state ($|A\rangle = |0\rangle$), the vacuum fluctuations are amplified by the non linear interaction and after a time τ, $\sinh^2 r$ photons are generated. Interesting results concern with the photon number distribution p_n for $|A\rangle = |0\rangle$ [17] :

$$\begin{aligned} p_{2n+1} &= 0 \qquad\qquad\qquad m = 0, 1, 2, .. \\ p_{2n} &= \left(\begin{array}{c} 2n \\ n \end{array} \right) \frac{1}{2^{2n}\cosh r}\,(\tanh r)^{2n} \end{aligned}$$

The suppression of all odd terms in photon number distribution express the physical result that the squeezed vacuum originates from a two photon process and it thus contains only pairs of photons.

From the ρ density matrix it is also possible to show that the marginal distribution for a generic quadrature X_θ is a Gaussian given by:

$$p(x, \theta) = \frac{1}{\sqrt{2\pi\Delta X_\theta^2}} e^{-\frac{x^2}{2\Delta X_\theta^2}}$$

with $\Delta X_\theta = \frac{1}{2}\sqrt{e^{2r}\sin^2\theta + e^{-2r}\cos^2\theta}$.

1.3 Non degenerate Parametric Amplifier

The *non degeneracy* condition is achieved when the two fields generated by means of the non linear interaction are mutually distinguishable. This correspond to the case of signal and idler at different frequencies or at the same frequency but cross polarized; in the following the second case will be considered.

The Hamiltonian describing the system is:

$$\mathcal{H}_{NL} = \hbar\frac{\omega_p}{2}\left(a_s^\dagger a_s + a_i^\dagger a_i\right) - i\hbar\frac{\chi^{(2)}}{2}A_p\left(a_i^\dagger a_s^\dagger - a_s a_i\right) \tag{1.8}$$

The corresponding Heisenberg equations are:

$$\frac{da_s}{dt} = \mathcal{E}\ a_i^\dagger; \qquad \frac{da_i^\dagger}{dt} = \mathcal{E}\ a_s \tag{1.9}$$

In the case of non degenerate parametric amplifier, the system exhibits a *two mode* squeezing since both signal and idler beams are needed to observe the squeezing properties. At this purpose it can be defined the generalized quadratures [3] :

$$X_\pm(\theta) = \frac{1}{\sqrt{2}}\left(X_s(\theta) \pm X_i(\theta)\right)$$

For signal and idler both in initial coherent states ($\Delta X_\xi^2(0) = \Delta Y_\xi^2(0) = 1/4, \xi = s, i$), it can be shown that [3] :

$$\Delta X_\pm(\theta)^2 = \frac{1}{4}\left(\cosh 2r \pm \cos 2\theta \cdot \sinh 2r\right) \tag{1.10}$$

so that:

$$\Delta X_\pm^2 = \frac{1}{4}e^{\pm 2r}; \qquad \Delta Y_\pm^2 = \frac{1}{4}e^{\mp 2r} \tag{1.11}$$

The squeezing is due to the quantum correlations which build up in the signal and idler modes; it possible to show that the individual modes are not squeezed. Equation (1.11) can be interpreted by saying that the fields actually squeezed are not a_s and a_i but their

combinations $d_+ = (a_s + a_i)/\sqrt{2}$ and $d_- = (a_s - a_i)/\sqrt{2}$ [3]. In this context, results obtained for the degenerate parametric amplifier apply to the fields $d_\pm$ and their quadratures.

A quantum interpretation of the two modes squeezing is given by considering that in parametric down conversion the pump photon is split into a pair of photons so that its noise can be imagined to be equally distributed on generated signal and idler photons.

Results for the non degenerate parametric amplifier can be obtained by introducing the two modes squeezing operator:

$$S_2(\zeta) = \exp\left[\frac{1}{2}\left(\zeta^* a_s a_s - \zeta a_s^\dagger a_i^\dagger\right)\right]$$

The state wave function, as well as the ρ density matrix or other operator for the output field are obtained by application of $S_2(\zeta)$ to the initial states for the signal and idler modes.

1.4 Gaussian States

Squeezed states make part of the larger class of Gaussian states, say states characterized by a Gaussian wave function. This result is readily demonstrated by applying evolution operator $S(\zeta)$ and $S_2(\zeta)$ to the input state and examining the state wave function. As an example, the wave function associated to the squeezed vacuum is given by $S(\zeta)|0\rangle$ where $|0\rangle$ represents the ground state for an harmonic oscillator. In the position representation q, $|0\rangle$ has Gaussian wave function $\psi_0(q) = \frac{1}{\sqrt[4]{\pi}} e^{-\frac{q^2}{2}}$ and $S(\zeta)|0\rangle$ becomes $\psi_\zeta(q) = \frac{1}{\sqrt[4]{\pi}} e^{-\frac{\zeta}{2}} e^{-\left(e^{-2\zeta}\frac{q^2}{2}\right)}$ [17]. For Gaussian states, quadrature distributions along each direction θ is Gaussian shaped.

This result is quite general. Gaussian state are obtained each time harmonic oscillators in their ground states are subjected to particular kinds of time-dependent potentials or interaction Hamiltonians. The most general N-mode Gaussian state can be formally expressed as $U_N|0\rangle$ with $U_N \equiv \exp\left[-\frac{i}{\hbar} H_N\, t\right]$ unitary operator with Hermitian gener-

[3] In this way $X_+(\theta) = \frac{1}{2}\left(d_+ e^{-i\theta} + d_+^\dagger e^{i\theta}\right)$ is the θ-quadrature for the field d_+ and analogously $X_-(\theta)$ the θ-quadrature for d_-.

ator H_N. It is possible to show that the requirement of Gaussian shaped wave function implies that H_N consists only of linear and bilinear combinations of annihilation and creation operators a_ξ ($\xi = 1, ..N$) with no further restrictions [52] . U_N factorizes into unitary operators whose generators are *linear* combinations of a_ξ and $a_\xi^\dagger$ and unitary operators whose generators are *bilinear* combinations of a_ξ and $a_\xi^\dagger$.

Single and two modes squeezing operator are part of the unitary operator whose generators are bilinear combination of the annihilation and creation (see Eqs (1.4-1.8)). Unitary operators whose generator only depends on linear combination of a_ξ and $a_\xi^\dagger$ are called *displacement operators* for the ξ^{th} mode. These are the operators that applied to an initial vacuum state give rise to coherent states.

Chapter 2:
Squeezed radiation from degenerate OPOs

2.1 OPO and input output relations

So far an open ended model of parametric amplifier has been considered. When the non linear medium is placed within an optical cavity acting as resonator, oscillation builds up inside and the system becomes an optical parametric oscillator (OPO). Confining the light in a cavity helps to obtain a sizable effect by increasing considerably the interaction time [2] so that squeezing can be generated even if non linear interaction is very weak.

In order to describe the effect of the OPO cavity, the whole system has to be imagined as merged into an heat bath made up of infinite harmonic oscillators representing different modes of the electro-magnetic field [51] . At zero, or ambient temperatures, the harmonics oscillator can be considered in their ground states since at involved frequencies, the mean photon number for thermal states are negligible. The heat bath acts as a passive system with whom the system inside the cavity tends to balance. The coupling between the two systems is provided by imperfect cavity mirrors or losses. These mechanisms act as ports allowing the photons inside the cavity to escape and the vacuum noise outside it to enter inside.

For each loss, the Hamiltonian describing the interaction of the external bosonic modes $b(\omega)$ with a single mode a inside the cavity is:

$$\mathcal{H}_{in-out} = i\hbar \int_{-\infty}^{+\infty} d\omega \, \kappa(\omega) \left(b^{\dagger}(\omega) \, a + b(\omega) \, a^{\dagger} \right)$$

with $\kappa(\omega)$ describing the strength of the interaction. $\kappa(\omega)$ can be considered approximately frequency independent for a wide interval around the cavity resonance frequency where it reaches its maximum. The effect of $\mathcal{H}_{in-out}$ on the a mode evolution, is sum-

marized by the *Langevin Equations* for the mode inside the cavity [3] :

$$\frac{da}{dt} = -\frac{i}{\hbar}\left[a\left(t\right), \mathcal{H}\right] - \gamma a\left(t\right) + \sqrt{2\gamma}a^{in}\left(t\right) \tag{2.12}$$

with $\mathcal{H}$ the Hamiltonian for the system inside the cavity. The term $-\gamma a\left(t\right)$ represents the damping due to loss ($\gamma \sim \kappa\left(\omega\right)$ is the *photon damping rate*), while the driving term $\sqrt{2\gamma}a^{in}\left(t\right)$ describes the input vacuum modes entering into the cavity from the environment. The field $a^{in}\left(t\right)$ can be expressed in terms of the heat bath modes $b_0\left(\omega\right)$ at the initial instant, as $a^{in}\left(t\right) = \int_{-\infty}^{+\infty} d\omega e^{-i\omega t} b_0\left(\omega\right)$ and represents an additional noise term. In the frequency domain its commutation rules are:

$$\begin{aligned} \left[a^{in}\left(\omega\right), a^{in\dagger}\left(\omega'\right)\right] &= \delta\left(\omega + \omega'\right) \\ \left[a^{in}\left(\omega\right), a^{in}\left(\omega'\right)\right] &= 0 \end{aligned} \tag{2.13}$$

thus indicating that input vacuum at different frequencies are mutually uncorrelated [4]. At zero or ambient temperature the field described by a^{in} can be depicted as a coherent vacuum state with Gaussian quadrature distribution.

The mode a and its trasmitted outside the cavity a^{out} are linked by the *input-output relation* [3] :

$$a^{out}\left(t\right) + a^{in}\left(t\right) = \sqrt{2\gamma}\, a\left(t\right) \tag{2.14}$$

2.2 Linearization Procedure

Equation (2.12) can be applied to the case of a non linear Hamiltonian $\mathcal{H} \equiv \mathcal{H}_{NL}$ as described in the previous chapter. The quantum Langevin equation for the pump (a_p)

[4] a^{in} presence is mathematically required to preserve the commutation rules for a and it is an expression of the fluctuation-dissipation theorem.

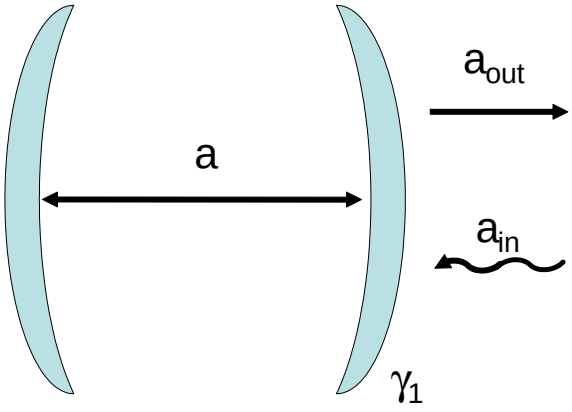

Figure 2.1. A schematic representation of the cavity field and the input output fields for a single-ended cavity. The only loss mechanism is due to the input mirror (with damping γ_1)

and signal (a_s) and idler (a_i) modes can be written as:

$$\begin{aligned} \frac{da_\xi}{dt} &= -\gamma a_\xi + \chi^{(2)} a_p a^\dagger_{\xi'} + \sqrt{2\gamma} a^{in}_\xi (t) \qquad (\xi, \xi' = s, i) \\ \frac{da_p}{dt} &= -\gamma_p a_p - \left(\chi^{(2)}\right)^* a_\xi a_{\xi'} + \sqrt{2\gamma_p} a^{in}_p (t) + A_p \end{aligned} \tag{2.15}$$

where A_p represent the external coherent pump field and losses for signal and idler modes have been considered equal. These equations are non linear in the bosonic operator and are usually solved by *linearization* of operators $\hat{a}$ around the stationary values, $\hat{a} \longrightarrow \alpha + \delta\hat{a}$ [53] . The steady state complex amplitudes α [5] are retrieved by (2.15) when considering $da/dt = 0 = a^{in}(t)$. Letting $\mathfrak{r} = \alpha_s = \alpha_i$, the algebraic system for the signal and idler αs can be reduced to equation:

$$0 = \mathfrak{r}^3 - \frac{\chi^{(2)} A_p - \gamma\gamma_p}{\left(\chi^{(2)}\right)^2} \mathfrak{r} \tag{2.16}$$

By analyzing (2.16) it can be seen that its solutions depend on the pump amplitude A_p. For $A_p \leq A_{th} \equiv \gamma_p\gamma/\chi^{(2)}$, it admits one stable solution, corresponding to $\mathfrak{r} = 0$. In this case the system is said to be *below threshold* and the pump stationary amplitude is $\alpha_p = A_p/\gamma_p$. If $A_p \geq A_{th}$ the system undergoes a phase transition; the steady state values for α_s and α_i exhibit a pitchfork bifurcation and Eq. (2.16) admits non null stable solutions describing the amplitude of the classical signal and idler beams built up in parametric oscillation. The existence of a threshold condition express the fact that in presence of losses, the pump has to be strong enough for the effect of parametric interaction to exceed the losses effect and bright signal and idler mode to be visible.

In the following the system below threshold will be considered. In this case the non linear Eqs. (2.15) are linearized by considering the pump as a classical undepleted beam of amplitude $\alpha_p = A_p/\gamma_p$ and neglecting the quantum equation for the mode a_p.

[5] It is worth stressing that the amplitude is no longer an operator, the operator character in $\hat{a}$ is only preserved in the fluctuating part $\delta\hat{a}$.

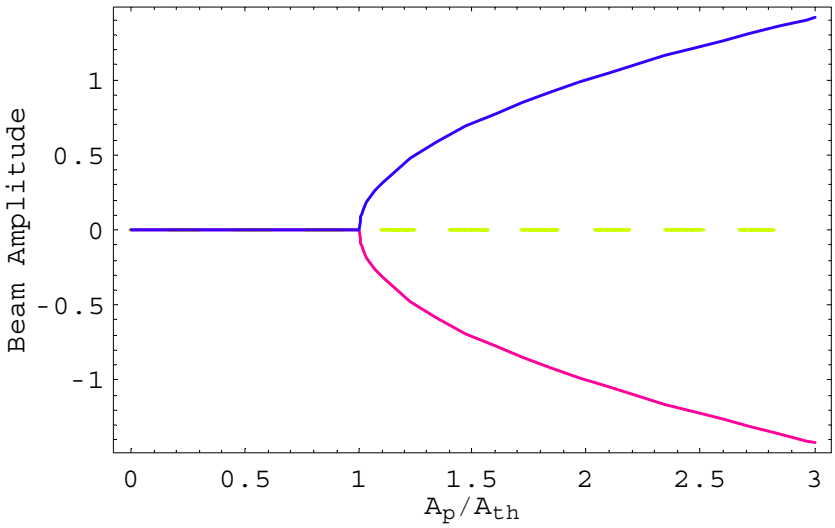

Figure 2.2. Steady state solutions of the intracavity amplitude for the DOPO as a function of the pump coherent amplitude normalized to the threshold (A_p/A_{th}). For $A_p/A_{th} \leq 1$, the sole stable solution is the one corresponding the $\alpha_s = \alpha_i = 0$. Above threshold the null solution is no longer stable (dashing line) and the system admits two stable positive (blu) and negative (red) solutions corresponding to the classical amplitudes of bright signal and idler beams. The plot refers to unit such that $\gamma_p\gamma/\left(\chi^{(2)}\right)^2 = 1$

Since $\alpha_\xi = 0$, equations for the operator a_ξ and those for their fluctuations coincide:

$$\frac{da_\xi}{dt} = -\gamma a_\xi + \mathcal{E} a^\dagger_{\xi'} + \sqrt{2\gamma_\xi} a^{in}_\xi (t) \qquad (\xi, \xi' = s, i) \tag{2.17}$$

with $\mathcal{E} = \chi^{(2)} A_p / \gamma_p$.

2.3 Squeezing at the degenerate OPO output

In case of degenerate OPO (DOPO) equation for a_s and a_i become indistinguishable as previously discussed.

An ideal cavity with only one loss mechanism, as considered up to now, is called *single-ended cavity.* Obtained results can be extended to a more realistic *double-ended cavity* where more losses are present. In the following γ_1 will indicate the damping associated to cavity input mirror and γ_2 the damping associated to other losses mechanisms (other mirror transmission or crystal absorption and diffraction). Langevin Eq. (2.17) generalizes into [21] :

$$\frac{da}{dt} = \mathcal{E} a^\dagger - (\gamma_M + i\psi)\, a(t) + \sqrt{2\gamma_1} a^{in}(t) + \sqrt{2\gamma_2} b^{in}(t)$$

being $\gamma_M = \gamma_1 + \gamma_2$ the overall loss rate, ψ the detuning of mode a with respect to perfect cavity resonance and a^{in} and b^{in} the input fields due to γ_1 and γ_2. In the frequency domain the Langevin equations for a and $a^\dagger$ turn into algebraic equations and are easily solved.

Experimentally the field actually measured is the one outside the cavity. By making use of (2.14) with $\gamma \equiv \gamma_1$, the solution for the field a^{out} outing the cavity through the input mirror is shown to be [21] :

$$\begin{aligned} a^{out}(\omega) \;=\; & \frac{\left[(\gamma_1 - i\psi)^2 - (\gamma_2 - i\omega)^2 + \mathcal{E}^2\right] a^{in}(\omega) + 2\mathcal{E}\gamma_1 a^{in\dagger}(-\omega)}{(\gamma_M - i\omega)^2 + \psi^2 - \mathcal{E}^2} \\ & + 2\sqrt{\gamma_1\gamma_2}\frac{(\gamma_M - i\omega - i\psi)\, b^{in}(\omega) + \mathcal{E} b^{in\dagger}(-\omega)}{(\gamma_M - i\omega)^2 + \psi^2 - \mathcal{E}^2} \end{aligned} \tag{2.18}$$

2.4 Quadrature Properties

The squeezing properties are discussed by looking at the field quadrature $X_\theta(\omega)$. By making use of commutation relations, it is possible to rewrite $\langle \Delta X_\theta \rangle^2$ as:

$$\langle \Delta X_\theta \rangle^2 = \frac{1}{4}\left(1 + 4\langle :\Delta X_\theta^2: \rangle\right) \tag{2.19}$$

the symbol :: indicates the normal ordering. For a coherent vacuum state, as the one at cavity input (a^{in} or b^{in}), $\langle :\Delta X_\theta^2: \rangle = 0$ and the quadrature noise reduces to the *shot noise* $\langle \Delta X_\theta \rangle^2 = 1/4$. For fields generated by non linear interaction, $\langle :\Delta X_\theta^2: \rangle$ can be both positive or negative, thus giving rise to a non classical modulation below and above the shot noise [6].

By exploiting (2.13) and (2.18), amplitude and phase quadrature spectra are calculated for the output field. For zero detuning ($\psi = 0$) it is possible to show that [21] :

$$\begin{aligned} \left\langle \Delta X^{out}(\omega) \right\rangle^2 &= \frac{1}{4}\left(1 + 4\frac{\gamma_1 \mathcal{E}}{\left(\gamma_M - \mathcal{E}\right)^2 + \omega^2}\right) \\ \left\langle \Delta Y^{out}(\omega) \right\rangle^2 &= \frac{1}{4}\left(1 - 4\frac{\gamma_1 \mathcal{E}}{\left(\gamma_M + \mathcal{E}\right)^2 + \omega^2}\right) \end{aligned} \tag{2.20}$$

with the quadrature variance product:

$$\left\langle \Delta X^{out}(\omega) \right\rangle^2 \left\langle \Delta Y^{out}(\omega) \right\rangle^2 = \frac{1}{16}\left(1 + \frac{16\gamma_1\gamma_2\mathcal{E}^2}{\left(\left(\gamma_M - \mathcal{E}\right)^2 + \omega^2\right)\left(\left(\gamma_M + \mathcal{E}\right)^2 + \omega^2\right)}\right) \tag{2.21}$$

For $\mathcal{E} = 0$ (i.e. $A_p = 0$) the non linear interaction is not switched on and the quadrature variances as well as their product simply reduce to those for the input coherent vacuum ($\langle \Delta X^{out}(\omega) \rangle^2 = \langle \Delta Y^{out}(\omega) \rangle^2 = 1/4$ and $\langle \Delta X^{out}(\omega) \rangle^2 \langle \Delta Y^{out}(\omega) \rangle^2 = 1/16$). Otherwise, previous equations show that for the field outside the cavity exhibits noise enhancement on the amplitude quadrature (*anti-squeezing*) and noise reduction on the

[6] It is worth stressing that below the oscillation threshold the quadrature mean value is $\langle X_\theta \rangle = 0$ for each angle θ and the quadrature variances simply reduce to $\langle \Delta X_\theta \rangle^2 = \langle X_\theta^2 \rangle$. The normally ordered spectrum $\langle :X_\theta^2(\omega): \rangle = \int e^{i\omega t} \langle :X_\theta(t) X_\theta(0): \rangle dt$ represents the Fourier transform of the two time autocorrelation function for the operator X_θ. It can be equivalently obtained by performing the integration $\int \langle :X_\theta(\omega) X_\theta(\omega'): \rangle d\omega'$.

phase quadrature (*squeezing*). Condition of minimum uncertainty is satisfied only for $\gamma_2 = 0$. Best noise modulation is achieved for pump amplitude equal to threshold, say for $\mathcal{E} = \gamma_{_M}$. The corresponding squeezing spectrum is Lorentzian shaped with width $2\gamma_M$ and maximum height $\frac{1}{4}\left(1 - \frac{\gamma_1}{\gamma_M}\right)$. Optimal noise reduction corresponds to $\omega = 0$, say to cavity resonance, where fluctuations on the antisqueezed quadrature X^{out}. For the ideal case of single ended cavity ($\gamma_2 = 0$), the OPO output is perfectly phase squeezed with complete noise suppression $\left\langle \Delta Y^{out}(0) \right\rangle^2 \Big|_{\mathcal{E}=\gamma_1} = 0$. Since below threshold no macroscopic (coherent) amplitude is exhibited by the OPO output, the state can be described as an ideal squeezed vacuum one (see first chapter). The corresponding squeezing parameter is linked to the distance from the threshold $\mathcal{E}/\gamma_1$ as $r = \ln\left(\frac{1+\mathcal{E}/\gamma_1}{1-\mathcal{E}/\gamma_1}\right)$. This description is consistent with the observation that for $\gamma_2 = 0$, $\left\langle \Delta X^{out} \right\rangle^2 \left\langle \Delta Y^{out} \right\rangle^2 = \frac{1}{16}$ and the state reduces to a minimum uncertainty one.

In case of double ended cavity, squeezing is optimized for $\gamma_1 = \gamma_2 \neq 0$ (*symmetrical* cavity) where it reaches the maximum value of $\frac{1}{8}$, say one half of the input state noise $\frac{1}{4}$. This result can be shown to be the best obtainable for the field inside the cavity, given any choice of γ_1 and γ_2.

For non perfect resonance, the effect of detuning ψ must be considered and the expression for the field quadrature variances are:

$$\begin{aligned}
&\left\langle \Delta X^{out}(\omega) \right\rangle^2 \\
&= \frac{1}{4}\left(\frac{\left|(\gamma_1 - i\psi)^2 - (\gamma_2 - i\omega)^2 + \mathcal{E}(\mathcal{E} + 2\gamma_1)\right|^2 + 4\gamma_1\gamma_2\left|\gamma_M - i\omega + \mathcal{E} - i\psi\right|^2}{\left|(\gamma_M - i\omega)^2 + \psi^2 - \mathcal{E}^2\right|^2}\right) \\
&\left\langle \Delta Y^{out}(\omega) \right\rangle^2 \\
&= \frac{1}{4}\left(\frac{\left|(\gamma_1 - i\psi)^2 - (\gamma_2 - i\omega)^2 + \mathcal{E}(\mathcal{E} - 2\gamma_1)\right|^2 + 4\gamma_1\gamma_2\left|\gamma_M - i\omega - \mathcal{E} - i\psi\right|^2}{\left|(\gamma_M - i\omega)^2 + \psi^2 - \mathcal{E}^2\right|^2}\right)
\end{aligned} \tag{2.22}$$

For double ended cavity the effect of detuning is overcome by extra losses; the greater γ_2 the less influential is ψ. When $\gamma_2 \ll \gamma_1$ the low frequencies behaviour for

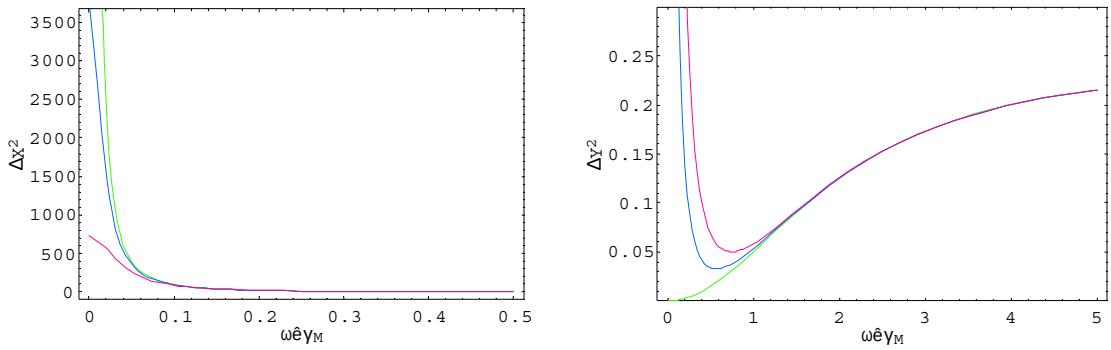

Figure 2.3. Spectral behaviour of the output field quadratures for single ended cavity for different detuning ($\phi = 0$ [green], $\phi = 0.15$ [blu] and $\phi = 0.25$ [red]). Plor refer to the system very close to threshold ($\mathcal{E}$ =0.995γ_M). The effect of detuning is significant only in the low frequency region of the spectrum.

$\langle \Delta X^{out} \rangle^2$ and $\langle \Delta Y^{out} \rangle^2$ is spoiled by the introduction of ψ. In the limit of single ended cavity, at the threshold $\langle \Delta X^{out}(0) \rangle^2$ is no longer diverging and decreases for increasing ψ while $\langle \Delta Y^{out}(0) \rangle^2$ deviates from zero and sharply increases with ψ. When $\mathcal{E}/\gamma_1 \lesssim 1$ for both $\gamma_2 = 0$ and $\neq 0$, the closer the system is to the threshold the stronger is the effect of ψ. The same behaviour is shown by the uncertainty product, where deviations from minimum ($\langle \Delta X^{out} \rangle^2 \langle \Delta Y^{out} \rangle^2 = 1/16$) are strongly sensitive to ψ for $\gamma_2 \approx 0$ and $\mathcal{E}/\gamma_1 \approx 1$.

Shown results are obtained by means of linearized theory. An evident drawback of the linear approximation is the prediction of zero noise level at threshold for single ended cavities with zero detuning. This is an unphysical result since it implies an infinite amount of phase information, which is impossible since the coherent pump that drives the parametric oscillator can only supply a finite quantity of phase information. Many investigations based on correction to linear theory have been performed to establish the ultimate limit to the noise reduction of a parametric oscillator near the threshold. In Re. [25] it is shown that the best squeezing in the zero-frequency part of the squeezing spectrum scales like $N^{-2/3}$ just below threshold provided the two field have similar damping rates being N the number of photon inside the cavity. It is worth stressing that non linear correction become evident only in the region extremely close to the threshold.

2.5 Double ended cavity and STV

Equations (2.21) and (2.22) show that deviations from minimum uncertainty increase with the size of extra losses γ_2 and with the detuning ψ and when approaching the threshold ($\mathcal{E} \rightarrow \gamma_M$). This result makes no longer satisfactory the output of real OPOs, the ideal squeezed vacuum description.

The most general description of squeezed Gaussian[7] vacuum state is provided by *squeezed thermal vacuum* state (STV) [54] . Corresponding quadrature variances are given by $\Delta X_\theta^2 = \Delta X^2 \sin^2\theta + \Delta Y^2 \cos^2\theta$ with:

$$\begin{aligned} \Delta X^2 &= \frac{1}{4}\left(2n_{th}+1\right)e^{2r} \\ \Delta Y^2 &= \frac{1}{4}\left(2n_{th}+1\right)e^{-2r} \end{aligned} \tag{2.23}$$

where parameters n_{th} (average thermal photons) and r (squeezing coefficient) mutually independent.. It is worth stressing that as for the output of real DOPOs the quadrature variances product do not satisfy the minimum uncertainty. By assuming the OPO output state to be in a STV, Eqs. (2.23) and (2.20) allow writing n_t and r. In the simple case $\psi = 0$:

$$\begin{aligned} n_{th} &= \frac{1}{2}\sqrt{\left(1+16\frac{\gamma_1\gamma_2}{\gamma_M^2}\frac{\left(\mathcal{E}/\gamma_M\right)^2}{\left(1-\left(\mathcal{E}/\gamma_M\right)^2\right)^2}\right)}-1 \\ r &= \frac{1}{2}\ln\left(\frac{1+\mathcal{E}/\gamma_M}{1-\mathcal{E}/\gamma_M}\sqrt{\frac{\left(1-2\left(1-\frac{2\gamma_1}{\gamma_M}\right)\frac{\mathcal{E}/\gamma_M}{1+\mathcal{E}/\gamma_M^2}\right)}{\left(1+2\left(1-\frac{2\gamma_1}{\gamma_M}\right)\frac{\mathcal{E}/\gamma_M}{1+\mathcal{E}/\gamma_M^2}\right)}}\right) \end{aligned}$$

For non zero detuning the behaviour of n_t and r is affected in a sensible manner by ψ only close to threshold and for $\gamma_2 \ll \gamma_1$. The expression for n_{th} and r as a function of ψ are obtained by Eqs. (2.23) and (2.22) for $\omega = 0$.

[7] It is worth reminding that also in case of detuning or extra losses the form of the process Hamiltonian preserves state gaussianity.

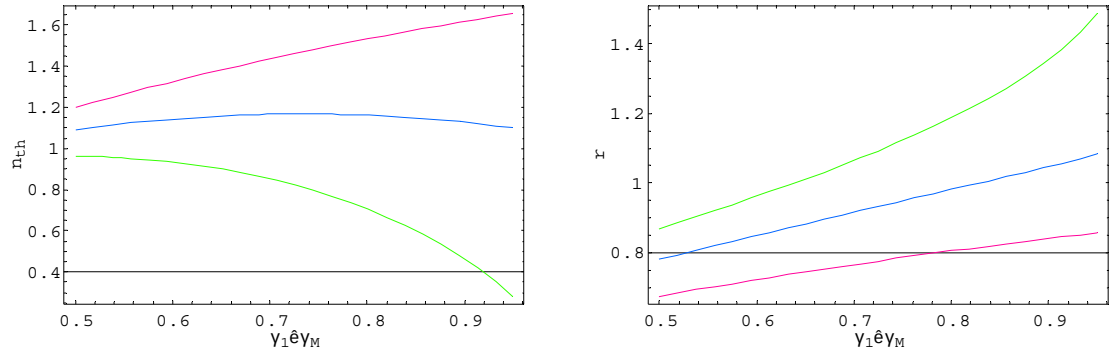

Figure 2.4. Parameters n_{th} and r as functions of the ratio γ_1/γ_M for three different detunings ($\psi = 0.0$ [green], 0.15 [blu], 0.25 [red]). Plot refers to $\mathcal{E}$ =0.7γ_M. The detuning plays a more significant role in proximity of $\gamma_1/\gamma_M \simeq 1$, that is for a single-ended cavity configuration.

n_{th} and r parameters are increasing function of γ_2 and the distance from threshold $\mathcal{E}/\gamma_M$. Once again, when $\gamma_2 = 0$, $n_{th} = 0$ and the state reduces to a pure squeezed one.

The state density matrix for a STV is:

$$\varrho = S(r)\nu S^{\dagger}(r) \tag{2.24}$$

where $\nu = (n_{th}+1)^{-1}\left[n_{th}/(n_{th}+1)\right]^{a^{\dagger}a}$ is a thermal state (n_{th} average photons). Expression (2.24) allows deriving all the state properties. In particular, the total photon number is given by:

$$N_{tot} = [\varrho\, a^{\dagger}a] = \sinh^2 r + n_{th} + 2n_{th}\sinh^2 r$$

The photon number distribution is:

$$p_n = \frac{C^n}{A^{n+\frac{1}{2}}} P_n\left(\frac{B}{C}\right) \tag{2.25}$$

being $P_n(x)$ the n-th Legendre function of the first kind and

$$\begin{aligned} A &= (1+n_{th})^2 - (2n_{th}+1)\sinh^2 r \\ B &= n_{th}(1+n_{th}) \end{aligned}$$

$$C = \sqrt{n_{th}^2(1+n_{th})^2 - (2n_{th}+1)^2 \sinh^2 r \cosh^2 r}$$

Analysis of (2.25) shows that conversely to pure squeezed vacuum states, the odd terms in p_n are no longer suppressed. This is consistent with the interpretation of STV as originated from pure squeezed vacuum when introducing OPO extra losses. Absorption or diffraction could destroy one photon of the couple generated by the non linear (two photon) process, thus originating single photons outside the cavity.

Chapter 3: Quantum State Detection

3.1 Homodyne Detector

The squeezing behaviour shown by below threshold OPOs, can be observed by detecting the output field quadratures in a balanced homodyne detector. This device is based on controlled interference of the field under scrutiny (homodyne *signal field*) with a strong coherent beam called *local oscillator (* LO*)* with the same frequency and spatial properties. The emerging beams are detected by linear response photodetector; the difference of relative photocurrents yields the signal quadrature amplitude X_θ in unit of the LO amplitude.

The optical mixing between the signal and LO fields is provided by a 50:50 beam splitter (BS), splitting each impinging beam in two equal parts (1/2 of the intensity is trasmitted, 1/2 is reflected). In the Heisenberg representation, its action on two orthogonally propagating fields (a_s, a_{LO}) is described as [17] :

$$\begin{pmatrix} a'_s \\ a'_{LO} \end{pmatrix} = \begin{pmatrix} \sqrt{\mathfrak{t}} & -\sqrt{1-\mathfrak{t}} \\ \sqrt{1-\mathfrak{t}} & \sqrt{\mathfrak{t}} \end{pmatrix} \cdot \begin{pmatrix} a_s \\ a_{LO} \end{pmatrix} \tag{3.26}$$

with the transmission coefficient $\mathfrak{t}$ equal to $1/2$.

Expression (3.26) shows that the BS is a four-port device with two inputs and two outputs; to preserve bosonic commutator for output beams, in case a single input beam is sent to the BS, the presence of a coherent vacuum field, acting as a second input, is required. Althrought not acting on the amplitude mean value, the vacuum field introduces additional noise, linked to the size of the input field attenuation. This is a consequence of fluctuation-dissipation theorem [40] .

For strong enough LO, a_{LO} can be substituted with the complex amplitude $A_{LO} = |A_{LO}|\, e^{i\theta}$, with the result:

$$\begin{aligned} a'_s &= (a_s - A_{LO})/\sqrt{2} \\ a'_{LO} &= (a_s + A_{LO})/\sqrt{2} \end{aligned}$$

Beams a'_s and a'_{LO} outing the BS are each directed to a photodetector measuring the field intensity. The interference term between the LO and the signal is actually contained in the photocurrents difference $\mathbf{I}_{s'-LO'}$ that is in turns proportional to the photon number difference $n'_s - n'_{LO}$:

$$\begin{aligned} n'_s - n'_{LO} &= A^*_{LO} a_s + A_{LO} a^\dagger_s \\ &= 2\,|A_{LO}|\, X_\theta \end{aligned} \tag{3.27}$$

This expression shows that subtracting the two photocurrents relative to a'_s and a'_{LO} the detection the quadrature X_θ of the signal is obtained. The reference phase θ is provided by the LO phase that can be experimentally driven providing measurements of the quadratures at different angles. The quantity X_θ in (3.27) is multiplied by the LO amplitude $|A_{LO}|$. Homodyne detector amplifies coherently the scale of the signal so that linear response detector are significantly influenced also by single photons of the signal. This provides an important technical advantage since, provided a LO strong enough, there is no need for single photon detector even in the measurement of vacuum fields.

3.2 Mode mismatch and homodyne efficiency

Since the LO serves as coherent amplifier, it also acts as an optical gate and picks out for detection only the signal mode whose spatial temporal profile matches the local oscillator's one. This gate can be very localized in space and time and its shape can be tailored to allow the investigation of a desired quantum field.

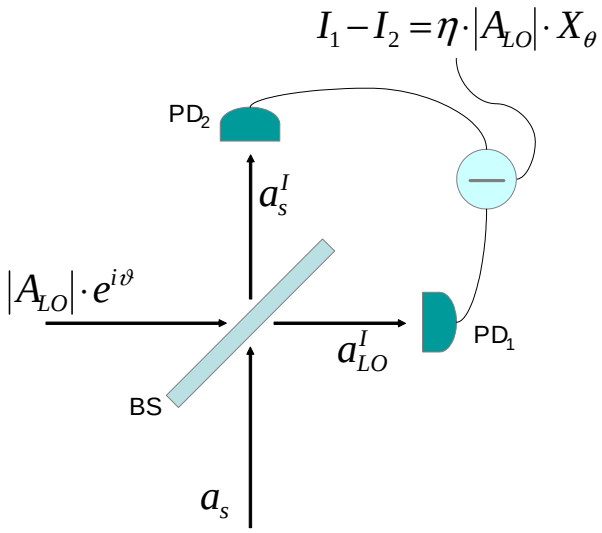

Figure 3.1. Schematic scheme of homodyne detector. The signal and the local oscillator beams are mixed on the beam splitter (BS). The output beams are detected by linear photodiodes (PD_1 and PD_2) and the relative photocurrent are subtracted to yield the signal quadrature X_θ

For single mode light beams, the actual field amplitude, including spatial-temporal contributions, is $\phi(\mathbf{x},t) = u(\mathbf{x},t) \cdot a$ where a is the field bosonic operator and $u(\mathbf{x},t) = v(\mathbf{x})\, e^{-i\omega t}$ with ω field frequency and $v(\mathbf{x})$ solution of the (spatial) Helmholtz equation [17] . The photocurrent $\mathbf{I}_{PD}$ provided by the detector, is given by the photon flux integrated on the acquisition time τ and on the sensible region area D. When including these effects, Eq. (3.27) turns into [17] :

$$\mathbf{I}_{s'-LO'} \propto A^*_{LO} a_{MM} + A_{LO} a^\dagger_{MM} \tag{3.28}$$

where the field a_{MM} can be expressed in terms of the signal operator a_s as:

$$a_{MM} = \eta_M^{1/2} a_s + (1-\eta_M)^{1/2} a_V$$

The *mode matching* coefficient

$$\eta_M^{1/2} = \int_0^\tau dt \iint_D \mathbf{u}^*_{LO}(\mathbf{x_D},t)\mathbf{u}_S(\mathbf{x_D},\mathbf{t}) dx_D dy_D$$

describes spatial-temporal superposition of the signal and LO modes as described in classical optical interference. Overall field phases can be chosen so that $0 \leq \eta_M \leq 1$, with $\eta_M = 1$ when the two beams perfectly overlap (*perfect mode matching*). The additional term

$$(1-\eta_M)^{1/2}\, a_V = \int_0^\tau dt \iint_D \phi_0(\mathbf{x_D},t) u^*_{LO}(\mathbf{x}_D,t) dx_D dy_D$$

physically represent the superposition between the LO and a vacuum field ϕ_0 accounting for other potential modes included in ϕ_s.

The mode mismatch effect can be described by imagining an effecting beam splitter of transmittivity $\mathfrak{t} = \eta_M$ before the homodyne detector: the transmitted beam is de-

tected, the reflected is lost. The meaning of η_M is that the possibility for the signal beam to be trasmitted and hence detected is linked to the size of its matching with the LO.

Other disturbs are introduced by non perfect photodetectors. For non unitary quantum efficiency ($\eta_{PD} < 1$), a fraction $1 - \eta_{PD}$ of the photons impinging on homodyne photodiodes is lost. The statistic of the fields actually measured is affected by this effect and additional noise is introduced. This situation can be reproduced by representing each (real) photodetector as an ideal photodetector ($\eta_{PD} = 1$) preceded by a beam splitter of transmittivity $\mathfrak{t} = \eta_{PD}$. Provided the two photodetectors have the same η_{PD}, the overall effect can be described by introducing a single beam splitter of transmittivity η_{PD} just before an ideal homodyne detector.

The effect of *mode mismatch* and non perfect detector can be combined by substituting the cascade of the BSs with transmittivity η_M and η_{PD} with a single BS whose transmittivity is the overall quantum efficiency $\eta = \eta_{PD}\eta_M$.

3.3 Quantum Homodyne Tomography

If the LO phase θ is spanned over a 2π interval, homodyne detector can also be used to reconstruct the Wigner function $W(x, y)$ and the state density matrix of the signal field. Marginal distributions $p(x, \theta)$ for quadratures X_θ are projections of the Wigner function on the plane in the quantum phase space, orthogonal to the (x, y) plane and individuated by the angle θ. The collection of all these "shadows" for different θ can be used to obtain the whole 3-dimensional Wigner function. More specifically the $p(x, \theta)$s are connected to $W(x, y)$ through the *Radon transform* [17] :

$$p(x, \theta) = \int_{-\infty}^{+\infty} W(x\cos\theta - y\sin\theta, x\sin\theta + y\cos\theta)dy \tag{3.29}$$

By exploiting this relation, experimental histograms for the quadrature measurement results ($\theta \in [0, 2\pi]$) can be processed by filtered back-projection algorithm to reconstruct the quantum Wigner function. The procedure is called *quantum homodyne tomography* (QHT).

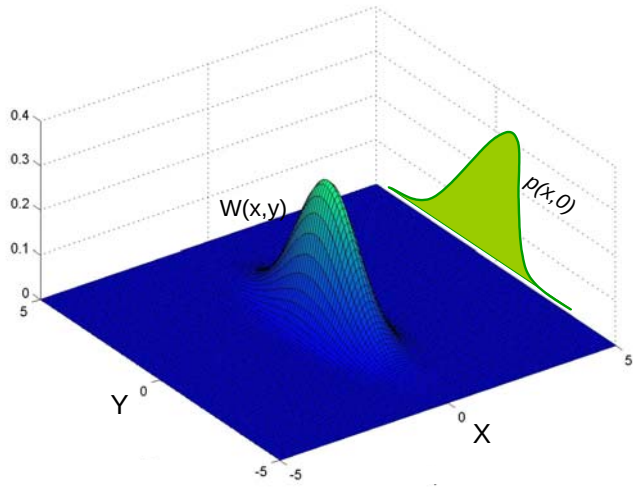

Figure 3.2. Principle of homodyne detection. The quadrature distribution $p(x,\theta)$ is retrieved as projection of the Wigner function $W(x,y)$ on the plane at angle θ with respect to the X axes ($\theta = 0$ in the present picture). The collection of $p(x,\theta)$ for different θ allows reconstructing the 3-dim shape of $W(x,y)$.

First attempts to access the Wigner function where based on inversion of Eq. (3.29) [17] . Unfortunately, in order to be applied to experimental discrete values, the technique requires the introduction of regularization procedure and a cutoff on the Kernel for the inverse Radon operator. Imposing a cutoff is equivalent to make *a priori* hypotheses on the state with bad effect on the Wigner function recostruction. Moreover, once $W(x,y)$ has been reconstructed, it has to be integrated with respect to certain functions to obtain the density matrix, ρ and the observable mean values.

The entire QHT procedure is simplified by skipping the intermediate passage through the Wigner function and reconstructing directly ρ and the mean values of interesting quantities[8]. The method is called *pattern functions QHT* [55] . The expectation value $\langle\hat{O}\rangle$ of field operator $\hat{O}$ is obtained as *statistical* average of an appropriate kernel function over experimental homodyne data expressed by $p(x,\theta)$. For non unitary homodyne efficiency ($\eta < 1$), $\langle\hat{O}\rangle$ is retrieved as [56] :

$$\langle\hat{O}\rangle = \int_0^{\pi} \frac{d\theta}{\pi} \int_{+\infty}^{-\infty} dx p_{\eta}(x,\theta)\, R_{\eta}[O](x;\theta) \tag{3.30}$$

where the *pattern function* $R_{\eta}[\hat{O}](x;\theta)$ is state independent and $p_{\eta}(x,\theta)$ is the marginal distribution for X_{θ} corrected by the effect of non perfect detector. In particular for Gaussian state, $p_{\eta}(x,\theta)$ reads [17] :

$$p_{\eta}(x,\theta) = \frac{1}{\sqrt{\pi(1-\eta)}} \int_{-\infty}^{+\infty} dq\, p(q,\theta) \exp\left(-\frac{\eta}{1-\eta}(q-\sqrt{\eta}x)^2\right) \tag{3.31}$$

that is a convolution of $p(x,\theta)$ with a Gaussian distribution of width $\sigma = \frac{1}{2}\sqrt{(1-\eta)/\eta}$.

The mean value $\langle\hat{O}\rangle$ described in (3.30) is experimentally retrieved by averaging the kernel $R_{\eta}\left[\hat{O}\right]$ over the experimental homodyne data $(x_i;\theta_i)$ as:

$$\langle\hat{O}\rangle = \overline{R\left[\hat{O}\right]} = \frac{1}{N}\sum_{i=1}^{N} R_{\eta}\left[\hat{O}\right](x_i;\theta_i)$$

[8] Basic idea is that since density matrix elements ρ_{nm} can be expressed as linear integral transformation of the $W(x,y)$ and the inverse Radon trasform is also a linear integral transformation, there is a linear expression for the density matrix in terms of the quadrature distributions $p(x,\theta)$.

where N is the total number of samples. Every datum (x_i, θ_i) individually contributes to the average, so that the operator mean value is gradually built up, till statistical confidence in the sampled quantity is sufficient. The procedure allows determining expectation values of observables inaccessible to direct homodyne detection including ρ matrix elements. It can be shown that regularization procedure of the inverse Radon transform is avoided [56] . Since the method does not require any filter it allows avoiding *a priori* hypotheses on the state, but as a counterpart it is more sensitive to statistical errors [56] .

The kernel function for the normal ordered product of power of a and $a^\dagger$ is:

$$R_\eta \left[a^{\dagger n} a^m\right](x;\theta) = e^{i(m-n)\theta} \cdot \frac{H_{n+m}\left(\sqrt{2}x\right)}{\sqrt{(2\eta)^{n+m}} \begin{pmatrix} n+m \\ n \end{pmatrix}} \tag{3.32}$$

where H_l is the l-order Hermite polynomial. It can be shown that, for this formula to be valid, η has to satisfy the lower bound $\eta > 1/2$ [56] .

From (3.32), it is possible to obtain:

$$\begin{aligned}
R_\eta \left[a^\dagger a\right](x;\theta) &= 2x^2 - \frac{1}{2\eta} \\
R_\eta \left[\left(a^\dagger a\right)^2\right](x;\theta) &= \frac{8}{3}x^4 - 2x^2 \\
R_\eta \left[\hat{X}_\phi\right](x;\theta) &= 2x\cos\left(\phi - \theta\right) \\
R_\eta \left[\hat{X}_\phi^2\right](x,\theta) &= \frac{1}{4}\left\{1 + \left(4x^2 - \frac{1}{\eta}\right)\left[4\cos^2\left(\phi-\theta\right) - 1\right]\right\}
\end{aligned}$$

3.4 Added noise in tomographic measurements

The tomographic measurement of a quantity $\hat{O}$ is defined as the average of the kernel $R\left[\hat{O}\right]$ over the homodyne data. In principle, a precise knowledge of the density matrix would require an infinite number of measurements on identical preparations of radiation. However, in real experiments one has only a finite number N of data at his disposal, and thus statistical analysis and errors estimation are needed. Provided that the kernel function satisfied the hypotheses of the central limit theorem, the confidence

interval on the tomographic reconstruction of $\left\langle \hat{O} \right\rangle$ is ([57] [58]):

$$\delta O = \frac{1}{\sqrt{N}} \overline{\Delta R_\eta \left[\hat{O} \right]}$$

where $\overline{\Delta R_\eta \left[\hat{O} \right]}$ represents the precision of the measurement and it is the variance of the kernel over the tomographic data:

$$\overline{\Delta R_\eta \left[\hat{O} \right]} = \sqrt{\int_0^\pi \frac{d\phi}{\pi} \int_{-\infty}^{+\infty} dx \; p\left(x, \phi\right) R_\eta^2 \left[\hat{O} \right] \left(x, \phi\right) - \langle \hat{O} \rangle^2} \tag{3.33}$$

It is worth saying that $\overline{\Delta R_\eta \left[\hat{O} \right]}$ depends on η.

An example of application of (3.33) is provided in Re.. [55] where the error for diagonal density matrix elements ρ_{nn} is computed to be:

$$\sigma_n = \frac{2}{\sqrt{N}}$$

When the quantity $\hat{O}$ can also be directly measured by a specific setup, the tomographic precision $\overline{\Delta R_\eta \left[\hat{O} \right]}$ can be compared with the corresponding quantum fluctuation $\sqrt{\langle \Delta \hat{O}^2 \rangle_\eta}$. It is worth noticing that for $\eta < 1$, due to the smearing effect of non unit quantum efficiency, the noise $\sqrt{\langle \Delta \hat{O}^2 \rangle_\eta}$ is larger than the ideal quantum fluctuation. It is possible to show [57] that the tomographic measurement is always more noisy than the corresponding direct measurement for any observable and any value of the detector quantum efficiency η.

For the field quadrature, the confidence interval on direct measurement of the quadrature, according with Eq. (3.31), reads:

$$\left\langle \Delta \hat{X}_\theta^2 \right\rangle_\eta = \left\langle \Delta \hat{X}_\theta^2 \right\rangle + \frac{1 - \eta}{4\eta}$$

This can be compared with the error for the tomographic reconstruction:

$$\Delta R_{\eta}\left[\hat{X}_{\theta}\right](x,\phi)^{2}=\left\langle \Delta\hat{X}_{\theta}^{2}\right\rangle +\frac{1}{2}\left\langle n\right\rangle +\frac{2-\eta}{4\eta}$$

corresponding to an extra noise:

$$N\left[\hat{X}_{\theta}\right]=+\frac{1}{2}\left(\left\langle n\right\rangle +\frac{1}{2\eta}\right)$$

Chapter 4: Experimental realization of DOPO and homodyne detection

4.1 Threshold and frequency degeneration

In this chapter, the implementation of the degenerate optical parametric oscillator (DOPO) and the homodyne detector are described. The OPO is controlled to work below threshold and in condition of frequency and polarization degeneration by choosing a proper non linear crystal and suitably setting its working point. At the same time the homodyne detector has to be set to optimize the detection of the DOPO output.

Since the ability of an OPO to squeeze the input quantum noise is linked to the distance from threshold, a stable and well controlled threshold is required.

DOPO results reported in previous chapters refer to the ideal case of plane wave and do not take into account the spatial temporal distribution for the interacting fields. Light beams actually involved in the process are *Gaussian beam*, whose transverse profile, is [9] [2] :

$$v(\mathbf{x}) = \frac{w_{\min}}{w(z)} e^{-r^2\left[\frac{ik}{2R(z)}+\frac{1}{w^2(z)}\right]}\, e^{-i(kz-\beta(z))} \tag{4.34}$$

where z is the propagation direction, $r^2 = x^2 + y^2$ and $k = 2\pi/\lambda$ is the wavevector. Quantities $w(z)$ and $R(z)$ respectively represent the *spot size* and the radius of curvature of the beam in z:

$$\begin{aligned} w^2(z) &= \frac{\lambda}{\pi}\left[b + \frac{(z-z_{\min})^2}{b}\right] \\ R(z) &= z\left[1 + \frac{b^2}{(z-z_{\min})^2}\right] \end{aligned}$$

[9] It is possible to show that beams generated from a traditional laser source or from a generic optical cavity are Gaussian beams.

where b is called *confocal parameter* and $z_{\min}$ corresponds to the position of the minimum spot size $w_{\min} = \lambda b/\pi$ (*beam waist*). The phase $\beta(z) = \arctan\left(\frac{z-z_{\min}}{b}\right)$. The confocal parameter b is strictly determined by the geometry of the cavity from which the Gaussian beam is emitted [10]. Modes described by (4.34) are in the so-called *TEM* $_{00}$ (*transverse electro-magnetic mode*) and correspond to minimum diffraction loss.

When considering beam Gaussian profile in the equations ruling signal, idler and pump modes evolution, the effective size of non linear effect depends on superposition integral of the three fields [59] . A full detailed analysis taking into account the effect of diffraction and different refraction indexes seen by the waves is reported in reference [59] ; the most interesting result concerns with the expression for the pump threshold power:

$$P_{th} = \frac{\pi^2}{4\mathcal{F}_s\mathcal{F}_i B_{up} E_{NL}} \tag{4.35}$$

In (4.35) $\mathcal{F}_{s/i}$ is the cavity finesse at the signal/idler wavelength $\lambda_{s/i}$ [11] and B_{up} the build up parameter for the pump at λ_p [12]. The non linear conversion coefficient, E_{NL}, depends on $\chi^{(2)}$, on the ratio of the non linear crystal length L over the pump confocal parameter b_p and on the *phase matching parameter* Δk :

$$\Delta k = k_p - k_s - k_i$$

being k_ξ the wavevector for the mode ξ. The function $E_{NL}(\Delta k)$ is bell-shaped with the maximum for $\Delta k \equiv \Delta k_{opt}$ and the half-height width given by $|\Delta k| \lesssim \frac{\pi}{L}$. For the OPOs discussed in this thesis, $\Delta k_{opt} \approx 0$ so that in the following the E_{NL} optimization will be considered as corresponding to a *perfect phase matching* $\Delta k = 0$. The quantity Δk expresses the phase mismatch between the three waves propagating inside the crystal, due to differences in the optical paths; since $\lambda_p \neq \lambda_{i,s}$ the wave inside the crystal travel at different phase velocities because of normal dispersion in the material. Requiring

[10] In case of laser outputs the cavity is the one in which the active medium is pumped

[11] For degenerate OPO the equation simplifies in $P_{th} = \frac{\pi^2}{4\mathcal{F}^2 B_0 E_{NL}}$ as long as all the cavity parameter for the signal coincide with those for the idler.

[12] The build up parameter is defined as the ratio of the power circulating inside the cavity over the input power.

a perfect phase matching is equivalent to impose the condition for constructive interference between the suharmonic optical waves generated in the different points of the crystal. Among all possible pair of signal and idler waves satisfying the energy conservation condition ($\omega_p = \omega_i + \omega_s$), the most favoured and in turn the actually generated one, is that satisfying the relation $\Delta k = 0$ (corresponding to the lower threshold).

Since the pump power is experimentally limited by the used laser source, the best way to reduce the OPO threshold is to adjust parameters $\mathcal{F}_\xi$, B_{up} and E_{NL} in (4.35). Finesses are determined by a proper choice of the cavity mirror trasmittances while the build up is enhanced by setting cavity resonance on pump mode. In the present setup P_{th} is addictionally lowered by ensuring triple resonance on pump, signal and idler modes (see following sections). Eventually, the non linear coupling is optimized by a suitable cavity geometry (mirrors radius of curvature and relative distance) and ensuring $\Delta k = 0$ at the desired wavelengths..

Degeneracy condition is obtained by using a type I non linear crystal, generating signal and idler beams with the same polarization, and by properly setting the OPO working point. The frequency degeneration condition is equivalent to requiring an optimum non linear coupling for signal and idler modes at $\lambda_s = \lambda_i = 2\lambda_p$. For experimentalist, this translates into the phase matching condition:

$$\Delta k\left(\boldsymbol{\lambda}, T\right) = \frac{2\pi}{\lambda_p}\left[n\left(\lambda_p, T\right) - n\left(2\lambda_p, T\right)\right] = 0 \tag{4.36}$$

with $\boldsymbol{\lambda} = (\lambda_p, \lambda_s, \lambda_i)$. In previous equation, it is stressed the dependence of refraction indexes n on both the beam wavelength and the crystal temperature T. Since $n\left(\lambda, T\right)$ is a strictly monothonic function of λ, the phase matching condition is achieved by choosing a suitable temperature $T = T_d$ so to satisfy Eq. (4.36). The *degeneration temperature* T_d is strictly determined by the crystal thermal properties. An active temperature control is required to guarantee $T = T_d$ against the environment temperature fluctuation.

4.2 OPO experimental set up

The entire experimental setup is based on a continuous wave (CW) commercial Nd:Yag laser (*LightWave model 142* dual wavelength) internally frequency doubled. The source emits both the fundamental (≈50mW @1064nm), used as homodyne LO, and the second harmonics (≈150mW @532nm), employed as DOPO pump. In this condition, the DOPO output beam at frequency degeneracy are generated exactly at 1064nm.

Just after leaving the laser head, the pump beam passes through an electro-optical phase modulator (EOM) and a Faraday rotator (FR) [62] . Phase modulation is necessary to the control of the cavity length, implemented by a standard Pound-Drever technique [63] . The insulator (FR) protects the source from cavity back-reflected light by sending it to a photodiode whose photocurrent is electronically processes to generate the Drever Pound error signal.

An half-wave plate, $\lambda/2_1$ together with a polarizing BS just before the FR, allows controlling the pump intensity sent to the OPO cavity. A second half-wave plate, $\lambda/2_2$, at the FR output is used to adjust the polarization of the injected pump beam (see fig. (4.1)).

Before entering the cavity, the beam impinges on a beam steering (HR@532) for the fine alignment of the injection axis. The following dichroic mirror DCR is transparent @532 nm and reflecting @1064 nm. On it impinges, together with the pump, a fraction of the laser output @1064nm that is used as IR seed for the cavity. The seed is obscured while the quadrature measurement on the DOPO output are performed.

An injection lens f_2 matches the pump beam TEM_{00} to the TEM_{00} mode of the cavity, say to the TEM_{00} whose b is given by the DOPO cavity geometry. This ensures that the available pump power is utilized to the maximum extent.

4.2.1 OPO cavity properties

The squeezed light source that has been implemented is a triply resonant DOPO (below threshold), based on a type I *Lithium Niobate* non-linear crystal ($LiNbO_3$:MgO)

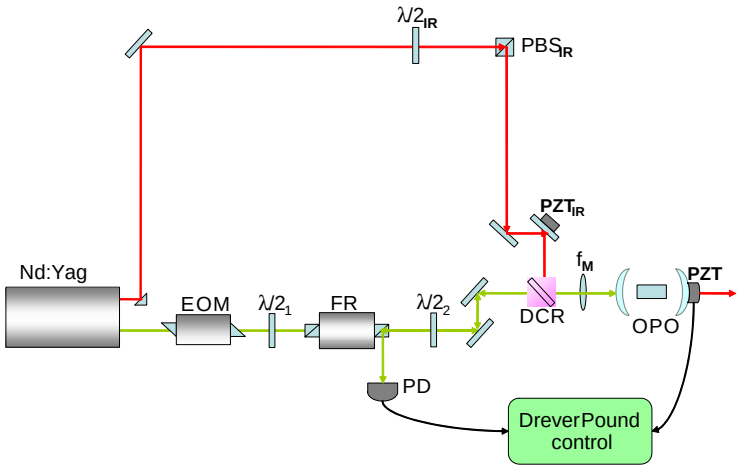

Figure 4.1. Experimental set-up for the OPO implementation. The laser output @532nm is used as OPO pump. The electro-optic modulator (EOM) introduces on the pump beam the phase modulation needed for the Drever Pound control. The half wave plate ($\lambda/2_1$) and the first PBS of the Faraday Rotator (FR) form a variable attenuator controlling the pump power sent to the OPO. The $\lambda/2_2$ and the matching lens (f_M) adjust the pump polarization and geometry. The laser output @1064nm is split by the system $\lambda/2_{IR}$+PBS$_{IR}$: the transmitted beam is used as LO for the homodyne detector (*not reported*), the reflected one as seed for the OPO cavity. The seed is sent to a beam streering, driven by a piezoelectric crystal (PZT$_{IR}$) to provide small changes in the optical path. Eventually it is injected into the OPO after reflection on the dicroic (DCR) beam splitter. The OPO back-reflected beam is sent by the FR to the phodiode PD connected to the Drever Pound system.

placed inside a two mirrors optical resonator. This configuration has been chosen instead of more stable monolithic or seminimonolithic configurations in order to achieve the maximum extent of versatility of the device. OPO cavity is made up of two mirrors with curvature radius $R = 51.68$ mounted on Aluminium plates spaced by Super-INVAR rods for mechanical isolation from the environment acoustic noise. Input mirror is HR at degenerate wavelength T_{in} (@1064nm)= $0.75^0/_{00}$, with T_{in} (@532nm)= 0.163%. Two choices are possible for the output mirror with T^I_{out} (@1064nm)= 2.9% or T^{II}_{out} (@1064nm)= 4.6%; in both cases T_{out} (@532nm) $\approx 1^0/_{00}$. Considering the total measured loss per pass inside the crystal (A =2% $@1064nm$), the corresponding cavity couplings for the two configurations are respectively $\eta^I_{out} = \frac{T_{out}}{(T_{out}+T_{in}+2A)} = 0.4$ and $\eta^{II}_{out} = 0.5$ with cavity linewidth@1064nm of 15MHz and 18MHz. The cavity length is set at $\sim$102.5 mm, not far from the concentric configuration to exploit the best condition for the non-linear interaction, expressed by E_{NL}.

The pump resonance condition, needed to enhance the build up, is ensured by the Drever Pound active control of the cavity length [63] . The loop actuator is provided by a piezoelectric crystal mounted behind the cavity output mirror. The obtained length stability is 0.7nm.

The OPO cavity is aligned by adjusting the geometry in order to transfer all pump power into the TEM_{00} mode, by minimizing the other orders TEM by reducing the asymmetries and properly setting the matching lens f_2. Resonance is achieved by locking the OPO cavity to the pump TEM_{00}: this reduces diffraction effects and maximize the coupling of the pump beam with the crystal.

The obtained threshold for the system for the mirror configurations employing T^I_{out} is 48mW with for the DOPO with T^I_{out} it is 68mW. The observed quadrature squeezing for η^I_{out} is 2.4dB.

4.2.2 Temperature control

Due to LNB properties, the frequency degeneration temperature is $T_d \approx$112°C. To work stably at this temperature the non-linear crystal is holded in an Aluminium oven,

temperature stabilized by means of an active control. The heater is a thermoresistor wire (*Thermocoax*) winded around the holder. The system is fitted with two temperature sensors. The first one, an AD590 chip, delivers a current proportional to the measured temperature. The difference between such an output and a reference value provides the error signal. The control is based on a PID (proportional integrative derivative) filter implemented digitally by a VME station.

The AD controller is assisted by a finer one, based on a Negative Thermistor Coefficient sensor (NTC), inserted in a resistive Wheatstone-like bridge. Temperature fluctuation induces changes in the NTC resistance and turns out in a deplacement of the bridge working point with respect to perfect balance. The current flowing through the unbalanced bridge is used as a signal error and is sent to a PID implemented by the VME.

Residual temperature fluctuations are $< 1\text{m}^{\circ}\text{C}$ over one hour.

4.2.3 Triply Resonance condition

The temperature control is also used to achieve triply resonance of the pump and the signal/idler modes. This configuration offers the advantage of a lower threshold for parametric oscillation and provides additional frequency selectivity in the OPO operation.

The resonance condition translates into a precise choice of the cavity length; since the Drever-Pound system locks the cavity to the pump mode TEM_{00}, small adjustments for triply resonance are obtained by finely tuning the crystal temperature around T_d while preserving the pump locking. Since signal and idler become indistinguishable, at degeneracy the triply resonance condition is equivalent to a double resonance one.

For a given temperature the width of the function $E_{NL}(\Delta k)$ is given by the condition $|\Delta k| \lesssim \frac{\pi}{L}$ [59] . This introduces a certain tolerance on phase matching condition: all the signal/idler frequencies satisfying the energy conservation and the phase matching within a domain $2\pi/L$ can oscillate. The maximum of the $E_{NL}(\Delta k)$ curve corresponds to the pair $\lambda_{s/i}$ satisfying exactly the phase matching condition for given λ_p and crystal

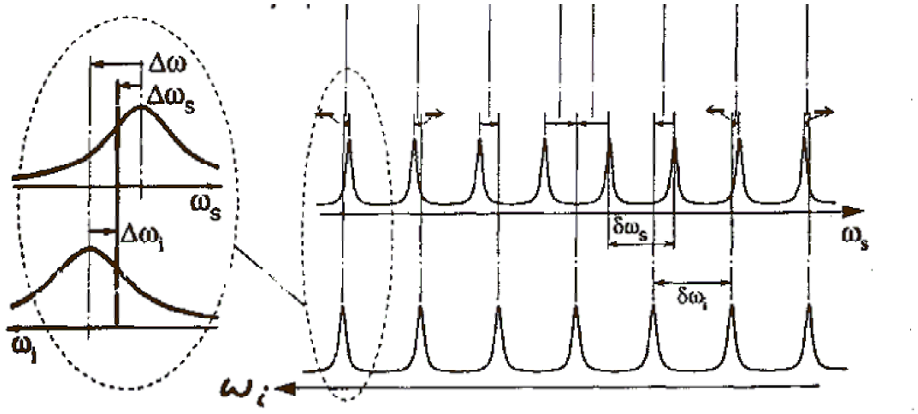

Figure 4.2. Giordmain and Miller diagram. Signal resonances are plotted as a function of signal frequency ω_s on ordinary linear scale, with frequency increasing from left to right. Idler frequency scale is determined by the signal one through the energy conservation realtion so to have $\omega_p = \omega_i + \omega_s$ along each vertical line. Idler resonances are diplayed as increasing from right to left. A signal-idler pair with both resonances centered on the same vertical line, together with energy conservation, will satisfy double resonance condition. Resonance superposition must occur within the linewidth (insert on the left).

temperature T. For $T \approx T_d$ this pair is the one with $\lambda_s = \lambda_i = 2\lambda_p$. When the pump level is above the threshold the most favourite pair of signal and idler is the one below the gain curve with the frequencies closest to the maximum gain.

When the crystal is inserted in a cavity, a further selection on the beam frequencies is introduced and only the frequency corresponding to cavity resonances can oscillate [13]. Since the signal/idler optical length is function of the index of refraction, the position of the signal resonances as well as the free spectral range are different from those for the idler. Small changes of T determines a replacement of the resonances and free spectral ranges. Experimentally by adjusting the temperature the two "combs" are mutually shifted until the signal and idler resonances are superimposed. In this case both signal and idler will oscillate at the same frequency inside the cavity and the simultaneous resonance condition will be satisfied [60] . This situation is explained in the Giordmaine Miller diagram [61] ; signal and idler cavity resonances are plotted against the respective frequencies, with free spectral ranges (FRS) $\delta\omega_s$ and $\delta\omega_i$. The ω_s and ω_i axes are set so to

[13] It is worth stressing that for the cavities used in the present set up the E_{NL} width expressed in frequency is two orders of magnitude greater that the cavity FSR for both the signal and idler beams. This implies that there are more FSRs for the IR beams that can exploit the effect of the non linear interaction.

have the signal frequency increasing from left to right and the idler's one in the opposite direction with scales adjusted to have the frequency conservation relation ($\omega_s + \omega_i = \omega_p$) satisfied along each vertical line. If a signal-idler resonance pair lies on the same vertical line it satisfies the simultaneous resonance condition. When the temperature is changed the position of the resonance will advance along the scales, one to the left the other to the right at slightly different rates because of dispersion, but the scale will not change.

Condition for the triply resonance must be satisfied within the cavity linewidths, that are in turns function of the cavity finesse for the signal and idler. By taking into account the properties of $n(\lambda, T)$, cavity linewidths can be expressed in terms of the crystal temperature. For the present case, assuming perfect degeneracy for the signal and idler beams, minimum width of the cavity resonance for the IR is $\approx 1.5\text{m}^{\circ}\text{C}$. This values, imposing the ultimate limit for the crystal temperature stability, is well above the one obtained with the used controller.

4.3 Parametric gain measurement

An estimation of the squeezing degree and in turn of the distance from threshold is provided by the study of parametric gain for the system below threshold. This measurement is based on phase dependent amplitude amplification/deamplification experienced by an input seed at degeneracy wavelength (i.e. 1064 nm). Experimentally, the seed amplification is measured as a function of the phase relative to the pump. At this purpose the seed optical path is linearly scanned in time by reflection on a piezoelectric (PZT) mounted mirror driven by a linear ramp. As a reference for the seed amplitude, it is taken the value relative to the infrared beam transmitted by the cavity in absence of the pump (say when the non linear process is completely switched off).

The parametric gain oscillatory behaviour is directly seen by sending the DOPO output to a linear photodiode. The minimum of the gain curve, corresponding the best deamplification, is independent on the seed power and is linked to the distance from

threshold by relation [64] :

$$G_{\min} = \left[1 + \sqrt{\frac{P}{P_{th}}}\right]^{-2} \tag{4.37}$$

where $G_{\min}$ is the curve minimum and P is the pump input power. The limiting value for $G_{\min}$ corresponds to 0.25 for $P = P_{th}$. By inverting formula (4.37), from the measured $G_{\min}$, it is possible to obtain the DOPO working point. The maximum $G_{\max}$ shows a sharper dependence on P/P_{th} and increases when the threshold is approached of an amount inversely proportional to the seed power [64] .

For a certain OPO working point, $G_{\min}$ also provides an estimation of the best obtainable squeezing $\mathcal{S}$, say the spectral noise at zero frequency for the DOPO output normalized to shot noise:

$$1 + \mathcal{S} = 1 - 4\sqrt{G_{\min}}\left(1 - \sqrt{G_{\min}}\right)$$

At the threshold perfect squeezing at zero frequency is achieved.

Parametric gain is also used to determine the degeneracy temperature. Since the gain itself depends on the non linear interaction size, it is optimized when Δk is set to zero at the frequency of the seed, say, in the present case, at $T = T_d$. The search for T_d is performed by checking the amplification and deamplification of the seed at different temperature and choosing the one ensuring the best $G_{\min}$ for the same P_{ω_p}.

At $T \approx T_d$, the best $G_{\min}$ experimentally obtained with the used setups is $G_{\min} = 0.275,$ corresponding to 82% of distance from threshold and a theoretical optimum squeezing of -26 dB. Approaching more closely the threshold the parametric gain measurement becomes unreliable due to resolution problems of the photodiode signal. In this case the measurement of P_{ω_p}/P_{th} is done by directly measuring the threshold and the green power injected inside the DOPO.

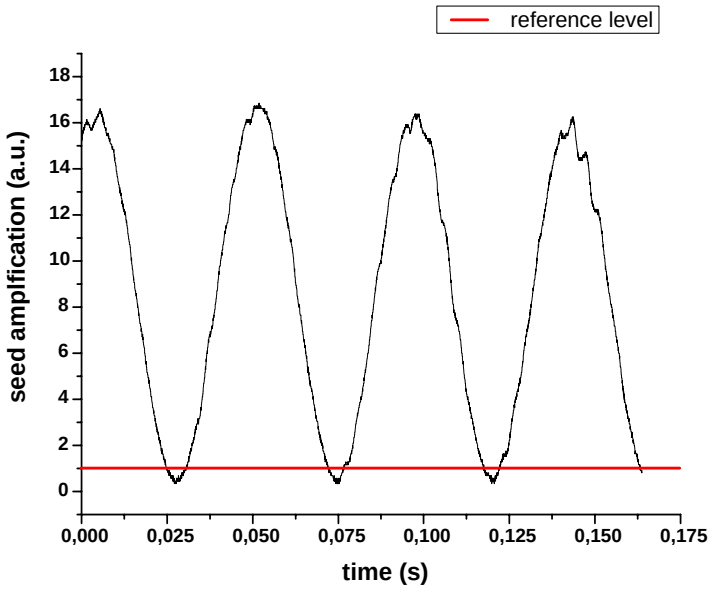

Figure 4.3. Seed amplification and deamplification normalized to the reference value (seed transmitted by the cavity in absence of the pump). Time variation linearly corresponds to seed phase variation. The curve refers to a minimum $G_{\min}$ =0.33 ($P/P_{th} \approx 0.55$).

4.4 The Homodyne detector

The DOPO output is sent to an homodyne detector. It consists of a beam splitter (BS), two focusing lenses and a pair of high quantum efficiency photodiodes (*Epitaxx ETX300*, indicated as PD_1 and PD_2). Each photodiode is matched to a low–noise trans–impedance AC ($>$ few kHz) amplifiers based on CLC425. The two AC outputs are connected to an hybrid power splitter/combiner giving both sum and difference of the incoming signals. The difference photocurrent is further amplified by a low noise high gain amplifier (*Miteq AU1442* G=34dB, noise figure 1.2) [26] . The DC components of each photocurrent are sent to an additional output used to check the homodyne balancing.

The homodyne local oscillator (LO), propagating orthogonally to the signal, is provided by the laser output @1064nm.

Electronics has been carefully checked for what concerns extra-noise sources and RF pick-up. In particular, the photodiodes and all the amplifiers are powered by low noise isolated DC voltage generators.

The overall detection efficiency depends on detector balancing (i.e. how equal are the two photocurrents) and mode matching between signal and LO. Accordingly many efforts are required to reach these conditions.

4.4.1 Detector balancing

To optimize the detection, electrical signals for the two BS outputs must have the same amplitude. This task is achieved by matching the two homodyne photodiodes and their downstream electronics and by aligning the BS so to have trasmittivity $\mathfrak{t} = 1/2$ (balanced BS)

First of all, it is chosen a pair of photodiode heads with the closest quantum efficiencies η_{PD_j} (η_{PD1} $\approx$0.91 , η_{PD2} $\approx$0.90 for the used pair) and dark currents I_{PD_j} (I_{PD_1}=15nA, I_{PD_1}=11nA). Moreover electronic components in the two photodiode transimpedance amplifiers are matched: a characterization of the response for different power of the input radiation has given for the photodiodes DC conversion coefficient

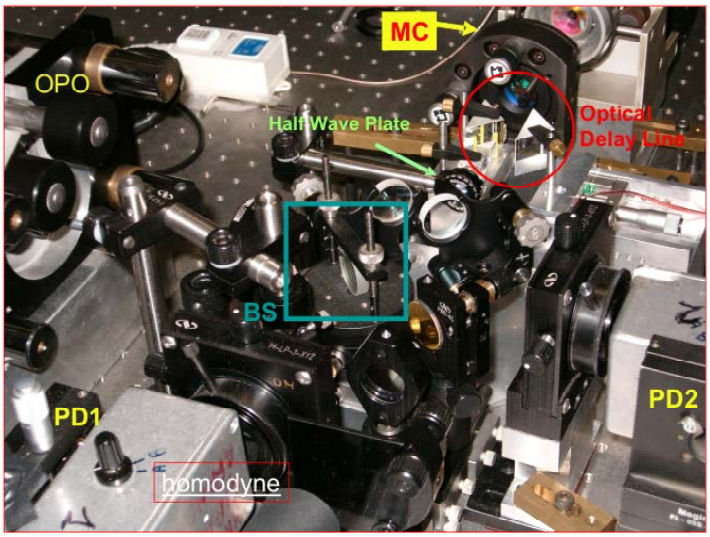

Figure 4.4. A picture of the homodyne detector showing the beam splitter (BS), the two photodiodes$PD_{1/2}$ (each preceeded by a focusing lens), the MC cavity, the prisms of the optical delay line and the half wave plate for polarization matching.

G_{PD_1}= 323±1 mV/mW and G_{PD_2}= 321±1 mV/mW. Differences for the AC output, actually used in the homodyne detection are negligible. The saturation power is 6mW for both PD_1 and PD_2.

The BS is balanced only when oriented exactly at 45° with respect to both signal and LO propagation directions. Small BS rotations are allowed by a rotatory stage with micrometric screws. Unbalance is estimated by comparing, for different BS angle, the transmitted P_1 and reflected P_2 powers on the homodyne photodiodes:

$$\Delta P = \frac{|P_1 - P_2|}{P_1 + P_2}\% \tag{4.38}$$

with $P_j = \frac{V_j - V_{j\text{dark}}}{G_{PD_j}}$ taking into account different photodiode gains G_{PD_j} and dark voltage $V_{j\text{dark}}$. BS orientation is modified till perfect balancing $\Delta P = 0$ is reached simultaneously for the signal and the LO beams.

Experimentally the alignment is performed by obscuring the LO and the OPO pump and sending on the BS the output of the seeded OPO locked to IR TEM_{00} resonance. Powers measured by each homodyne photodiode over long time interval (≥ 0.5 h) are compared by (4.38) and unbalance is estimated by time averaging $\Delta P\,(t)$. Since the seed transmitted by the OPO is very feeble ($\approx 30\mu W$ powered), the power measurement is badly affected by photodiode noise. Relative error on ΔP estimation is reduced by sending the LO on the BS to check the quality of the balance. Small corrections to the BS orientation can eventually be performed. Best obtained value for ΔP is accurate within $3\% \pm 1\%$.

4.4.2 Mode matching between LO and signal

Spatio-temporal mode matching condition is the most critical parameter in homodyne setting. As previously shown, the LO acts as an optical filter selecting for the detection only the field with its same properties. In experimental homodyne, the situation is reversed and the LO profile is tailored to match exactly the OPO output properties, so to optimize its detection. In the entire mode matching procedure the OPO pump is obscured and the LO oscillator is compared with the transmitted beam for the IR seeded

OPO resonant on the IR TEM_{00}. The LO amplitude is kept to be equal to the OPO output one, to be augmented only when the homodyne is aligned and ready to be used.

The superposition between two Gaussian beams is maximum when differences in the beam waists and in the radii of curvature are reduced to zero. Since $w(z)$ and $R(z)$ are fully determined by b and the optical path $z - z_{\min}$, the condition of optimum mode matching translates into the coincidence on these parameters for the two beams.

The matching of the two confocal parameters b is obtained by sending the LO through an empty cavity (*mode cleaner*, MC) with the same geometry of the OPO one. MC mirrors have the same (nominal) radius of curvature as the OPO's ($R = 51.68$). By means of a micrometric translation stage ($100\mu m$ sensible) mounted below the output mirror, the MC length is set to be equal to the measured OPO one (@1064nm) [14] with typical residual differences of $\approx 200\mu m$. The MC is set to resonate on the TEM_{00} by means of a Drever Pound system identical to the OPO's one.

Second requirement is the matching of optical paths $z - z_{\min}$ to the BS for the two beams outing the MC and OPO. If this condition is not satisfied, at a point z the beams will exhibit different radii of curvature and destructive interference can arise between the points of the two wave fronts. Optical paths are matched by adjusting the LO's one with an optical delay line. This is made up of three prisms whose relative distance can be varied with a resolution of $100\mu m$ by means of a micrometric translation stage. PZT-driven small changes of the optical delay line length control the LO phase θ. The phase is continuously spanned between 0 and 2π by applying a linear ramp to the PZT.

Eventually an half-waves-plate on LO path guarantees polarization matching.

The last, obvious, condition for optimum superposition is the coaxiality of the beams downstream BS so to prevent from spatial spread. The LO propagation direction is aligned with a beam steering (HR@1064 nm).

A quantitative measurement of the interference is provided by intensity measurement on the homodyne PDs. When introducing a dephase θ between LO and signal,

[14] The optical length @1064nm is obtained by looking at the IR transmission of the cavity when its length is linearly varied. The transmission shows peaks corresponding to the istantaneous resonance of the TEM_{00}. The optical length is provided by the relative distance between them.

the intensity for each BS outputs shows an oscillatory behaviour. A measurement of the beams superposition is the contrast CNT [62] :

$$CNT \equiv \frac{I_{\max} - I_{\min}}{I_{\max} + I_{\min}}$$

with $I_{\max\,/\,\min}$ the maximum/minimum of the experimentally measured oscillation. Assuming initially equal intensities of the LO and the signal ($I_{LO} = I_s = I$), for perfect mode matching, the system turns from perfect constructive interference ($I_{\max} = 2I$) to perfect destructive interference ($I_{\min} = 0$), so that $CNT = 1$ [15]. The mode matching quality is measured by deviations of the actual CNT from 1. The measurement is simultaneously performed on both the homodyne PDs, by correcting the effect of dark currents. The confocal parameter, the optical paths and the polarization of the LO are progressively adjusted to optimize the CNT.

The entire procedure is done by controlling the coaxiality of the beams on a CCD camera (*TM-745 Spiricon*) set at one of the two BS outputs. For perfectly coaxial beams, the interference figure on the CCD exhibits cylindrical symmetry and its central maximum expands when improving the mode matching.

Typical final values CNT=0.97$\pm$0.02 have been repeatedly obtained. The overall computed quantum efficiency (imperfect detectors+CNT effects) is η =0.88$\pm$0.02.

The very last part of the procedure is to set the homodyne detector in working condition. The LO power is increased up to 5.5mW. The phase is continuously spanned between 0 and 2π by applying a linear ramp to the optical delay line PZT, so that the phase is linearly varied with the time. The ramp period is set to be 200ms. During the measurement the DOPO is not seeded and only the pump is injected in it.

[15] When considering initial unbalance in the beam intensities ($I_s \neq I_{LO}$) it is more convenient to use the visibility, VIS :

$$VIS = \frac{2\sqrt{I_s I_{LO}}}{I_s + I_{LO}} \cdot CNT$$

For perfect balancing VIS reduces to CNT.

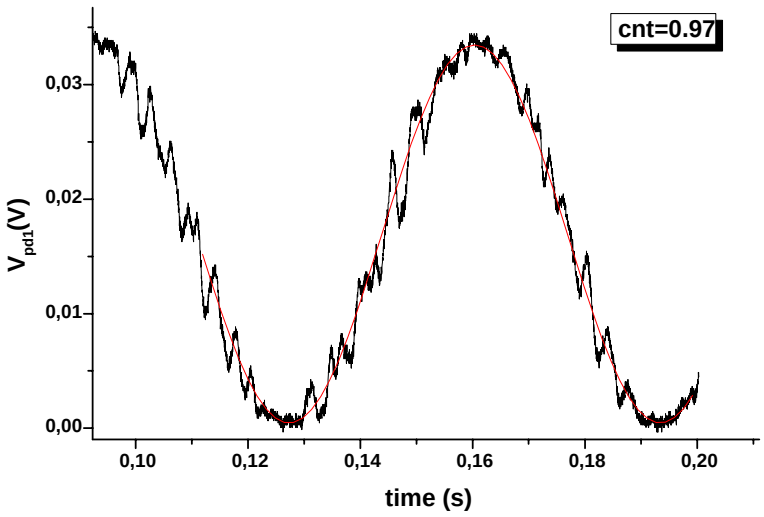

Figure 4.5. The inteference curve detected on one of the homodyne phodiodes. The time coordinate linearly corresponds to a variation of the LO phase. The measured contrast, obtained by a non linear fit of the data (red line) gives $CNT = 0.97$.

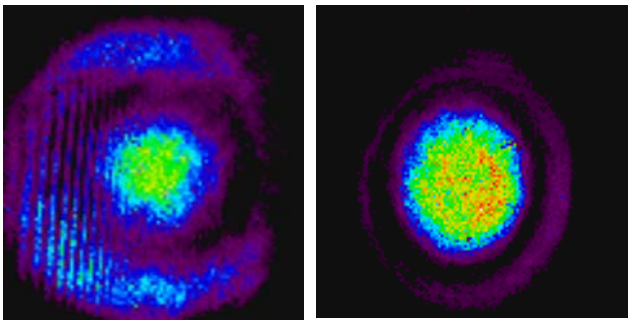

Figure 4.6. Typical interference patterns recorded by the CCD camera at one of the BS outputs. On the left the first interference ring around the central maximum is well visible. On the right, the mode matching has been improved and the power re-distributes from the first ring to the central maximum.

4.5 Homodyne data processing

The output of the homodyne detector provides the DOPO output quadratures. Acquired samples consist of N homodyne data $\{x_i, \theta_i\}$, $j = 1, ..., N$ with phases θ_i equally spaced. Since the piezo ramp is active during the whole acquisition time, to each θ_i corresponds a single value x_i.

The data can be processed in different ways. A first measurement is performed by looking at quadrature noise spectrum of the field outing the DOPO, as a function of the phase. As expected a sub-shot noise character is shown for the LO phase $\theta = \pi/2$. Spectral measurements are performed by sending the photocurrent difference to a spectrum analyzer (*Tektronix-2712*, working range $1KHz$-$10GHz$) set to zero-span operation (following only one spectral component). It has to be noted that the low frequency region of the spectrum is affected by the laser source noise (shot noise limited @2.5MHz). Moreover to see the squeezing effects it is necessary to follow the DOPO output behaviour well inside the cavity bandwidth (18MHz and 15MHz for $\eta_{out} = 0.5$ and 0.4 respectively). These conditions determined the choice of looking at the spectral component at $3MHz$. Acquisition is triggered by a linear ramp applied to the PZT, that drives θ. The ramp is adjusted to obtain a 2π variation in an acquisition window. Eventually data are normalized to the shot noise level measured by obscuring the DOPO output.

A different analysis is performed by sampling the homodyne output to acquire tomographic data to be used in state parameters reconstruction [26] . In this case, to avoid the laser low frequency noise, data sampling is moved away from the optical carrier frequency by mixing the homodyne current with signal of frequency Ω. Different values of Ω ranging from 2.7 to 8 MHz have been acquired to investigate the field state at different points of the cavity bandwidth. The ramp spans the 2π LO phase in 200 ms. The resulting current, is filtered by a cascade of low–pass filters with total bandwidth B.

Eventually the filter output is sampled by a digital acquisition PC based module (Gage 14100) able to acquire up to 1M–points per run with 14 bits resolution.

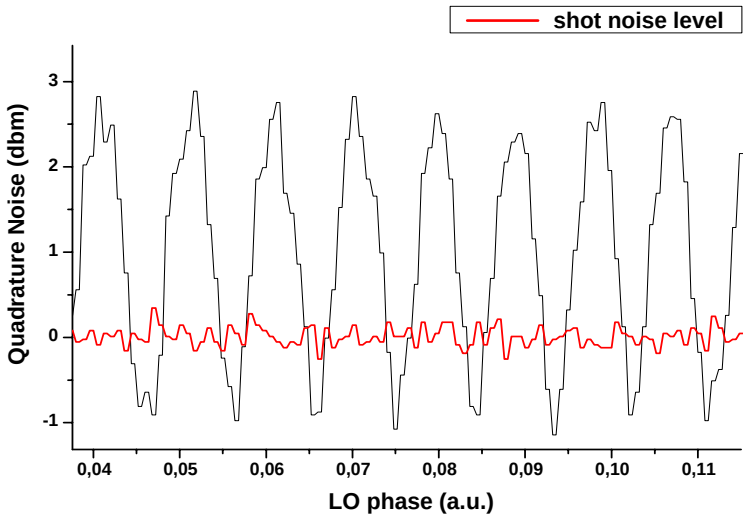

Figure 4.7. Variance ΔX_θ^2 (@3MHz) against the local oscillator phase θ linearly scanned with the time. The noise is normalized to the shot noise, value (red trace). It is possible to see the non classical reduction of the noise, below the shot noise.

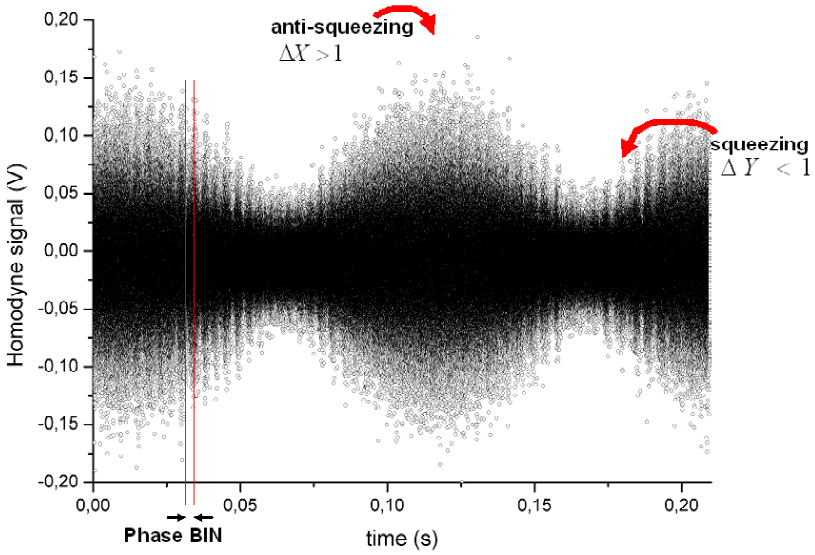

Figure 4.8. Tomographic data: quadratures outcomes against the LO phase θ scanned over 2π in 200ms. It is possible to see the enhancement and reduction of the noise corresponding respectively to the anti-squeezed and squeezed quadratures. By selecting a small fraction of the whole distribution, the phase θ can be considered to be approximately constant ($\theta \approx \bar{\theta}$), so that the data give the hystogram of the measured quadrature $X_{\bar{\theta}}$.

Calibration with respect to the noise of the coherent vacuum state is obtained by acquiring a set of data by obscuring the signal while scanning the LO phase θ. The total electronic noise power has been measured to be 15 dBm below the shot–noise level, corresponding to a signal to noise ratio of ≈ 40.

The reconstruction are carried out by dr. M.G.A. Paris by means of pattern function technique.

Chapter 5:
Deviations from Gaussianity for DOPO close to threshold

The experimental set-up illustrated in previous chapters permits to investigate the behaviour of the squeezed radiation emitted by the DOPO for different working conditions. In particular data are acquired at different distances from threshold $\mathcal{E}$, by changing the OPO cavity end mirror so to have two different value for the cavity escape efficiency $\eta_{out}^{I} = 0.4$ or $\eta_{out}^{II} = 0.5$ (see previous chapter). These measurements permit to test for the DOPO output, the effect of threshold fluctuation, due to crystal temperature fluctuation, pump intensity instability and cavity detuning.

The data analysis is performed by means of both pattern function tomography and direct statistical analysis of the quadrature histograms obtained by homodyning the DOPO output.

Tomographic measurements are performed at $\Omega = 3\,\mathrm{MHz}$. The resulting current, is filtered by a cascade of low–pass filters with total bandwidth $B \simeq 1\,\mathrm{MHz}$, and it is eventually sampled by the digital acquisition PC based module. The sampling rate ν is fixed to 5Msamples/s for experimental convenience. It is worth noting that a ratio $\frac{B}{\nu} < 1$ reduces the number of totally uncorrelated samples. In this way the number of effective samples is given by $N_{eff} = N \times \frac{B}{\nu}$. Being the measured process stationary the filtering-sampling procedure does not alter the statistics of the outcomes. In this way the effective number of samples has been privileged with respect to a better defined spectral selection.

5.1 Photon number distribution measurement

The first set of data is relative to $\eta_{out} = \eta_{out}^{I} = 0.4$ and $\mathcal{E} = 0.5$, 0.8 and 0.95. The distance from threshold is experimentally estimated by direct measurement, at the end of the data acquisition, of the power injected inside the cavity. It is worth stressing

that, to our knowledge, no previous squeezing measurement on DOPO output have been performed so close to threshold.

For each value of $\mathcal{E}$ typically 5 homodyne traces are acquired. For each, by means of state tomographic reconstruction, are reconstructed the diagonal density matrix element ρ_{nn} (up to $n = 5$) and the amplitude/phase quadrature variances (ΔX, ΔY) normalized to the shot–noise level obtained in homodyne calibration (see previous chapter, last section).

The reconstructed ΔX and ΔY are used to compute the photon number probability p_n for a STV state (see 2^{nd} chapter), under the assumption of Gaussian state. The obtained results, p_n can be compared, for each n with the reconstructed ρ_{nn} Since pattern function tomography is able to reconstruct the real state properties, without any a priori hypothesis on it (see 3^{rd} chapter), the aim of this test is to compare the results expected for the DOPO output with the actual experimental finding [26] .

In Fig. (5.1) are report ρ_{nn} and p_n for $\mathcal{E} = 0.5$ (lower plot), 0.8 and 0.95 (upper plot). As it can be seen the two determinations are sensibly different, their difference being larger the closer the OPO is to the threshold. As an example, for $\mathcal{E} = 0.5$ (lower plot) $\varrho_{00} = 0.780$ and $p_0 = 0.743$ ($< 3\%$ difference), while for $\mathcal{E} = 0.95$ (upper plot) $\varrho_{00} = 0.585$ and $p_0 = 0.533$ (10% difference). For $\mathcal{E} = 0.8$ (middle plot) is 8%.

This behavior has been confirmed by a second set of measurements performed with higher coupling efficiency ($\eta_{out} = 0.5$). In this case data refer to $\mathcal{E} = 0.5$, 0.60, 0.65, 0.70, and 0.8. Similarly to the previous case, the relative deviation between ϱ_{00} and p_0 increases with $\mathcal{E}$, but, for equal $\mathcal{E}$, the discrepancy is less evident than for the case of $\eta_{out} = 0.4$. The maximum deviation is less than 6% for $\mathcal{E} = 0.8$. In Fig. (5.2) the relative deviation between ϱ_{00} and p_o for both coupling efficiencies are reported.

5.2 Quadrature statistics measurement

The origin of these differences can be related to the fakeness of the model used to describe the DOPO output. To give a more quantitative estimation of the reliability of the STV state model, it is tested the Gaussian character of the state by analyzing the

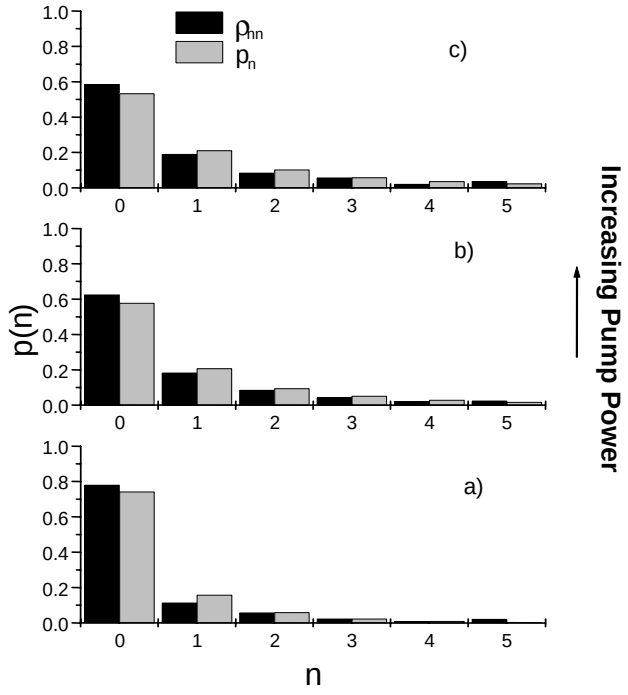

Figure 5.1. Photon number distribution for $\mathcal{E} = 0.5$ (a), 0.8 (b) and 0.95 (c) as recovered by pattern function tomography (ϱ_{nn} black columns) and in the Gaussian state hypothesis (p_n grey columns). The two determinations are different with a deviation increasing with pump power. Confidence intervals (not shown) are much smaller that the difference between the two determinations.

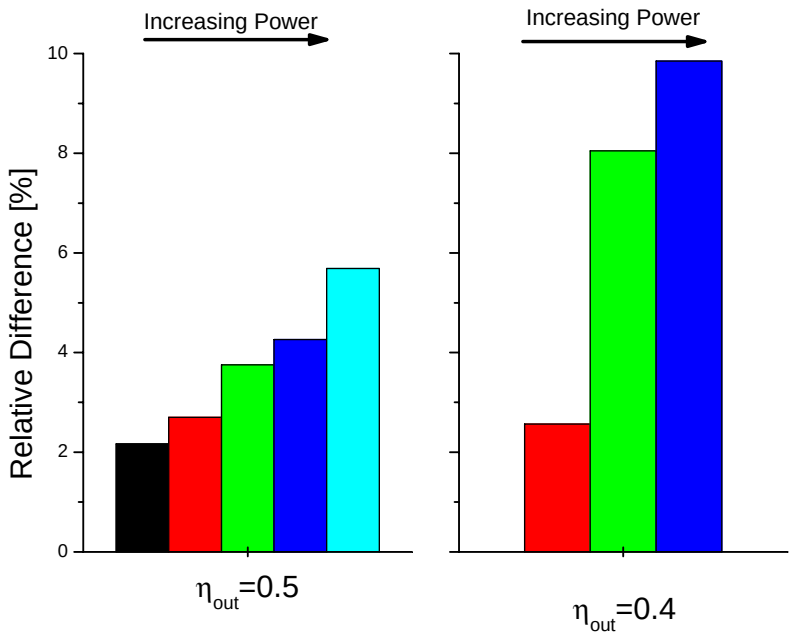

Figure 5.2. Relative difference between the two experimental determinations of ϱ_{00} (by pattern function tomography) and p_0 (Gaussian hypothesis). The reported deviations correspond to $\mathcal{E}$ = 0.5, 0.6, 0.65, 0.7, and 0.8 (η_{out} = 0.5), and $\mathcal{E}$ = 0.5, 0.8 and 0.95 (η_{out} = 0.4). In both cases deviation encrease when approaching the threshold, however they are more evident when the output coupling is lowered.

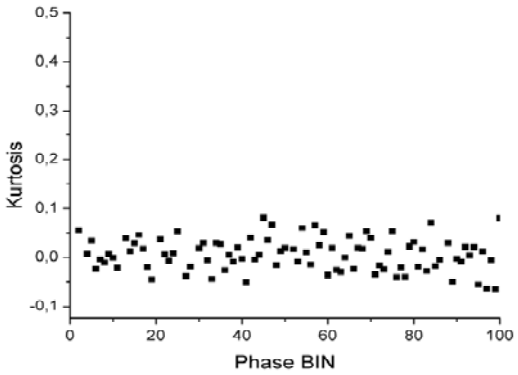

Figure 5.3. Kurtosis of $p(x,\theta)$ for homodyne data corresponding to the coherent vacuum maesurement, obtained obscuring the signal port of the homodyne detector. The Kurtosis distribution is flat with mean value practically equal to 0 for every value of θ as expected for Gaussian beams.

data statistics at a fixed θ. It is worth remembering that indeed for a Gaussian state, the Wigner function is Gaussian and so is the marginal distribution $p(x,\theta)$ at fixed θ: any deviation of $p(x,\theta)$ from a Gaussian is an indication of the deviation of the state itself. The deviation of a statistical distribution from a Gaussian can be evaluated by means of the Kurtosis [40]

$$K = \frac{1}{N}\sum_{i=1}^{N}\frac{(x_i-\bar{x})^4}{\sigma^4} - 3$$

which vanishes in the Gaussian case.

Each data set refers to a LO phase θ spanning between 0 and 2π corresponding to 10^6 points acquired in 200 ms. In order to test the statistics at a fixed θ_n the entire tomographic set is divided in 100 phase bins (10000 data each, lasting 2 ms). For each bin the LO phase con be considered approximately constant so that the histogram of the data describes $p(x,\theta_n)$ for a given $X(\theta_n)$.

For a Gaussian state the kurtosis distribution with the phase bins is expected to be flat with mean value consistent with zero. This is what actually observed for the calibration vacuum noise, obtained when obscuring the signal port of the homodyne detector.

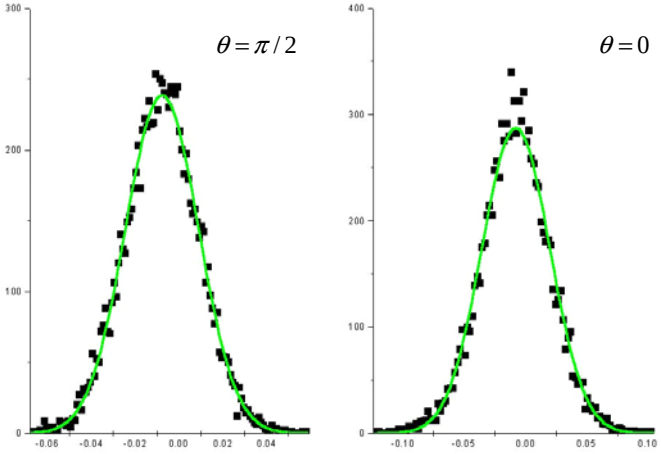

Figure 5.4. Distribution of X_θ values measured for $\mathcal{E}$=0.95. Full lines (green) represent Gaussian with the same mean and variance. As it can be see for $\theta = 0$ the data are not in agreement with the Gaussian distribution.The measured kurtoses K for the two distributions are respectively equal to 0.005 and 0.5.

K_θ for calibration data is zero within $5 * 10^{-3}$. This result releases from the hypothesis of any spurious effects of the detection apparatus on the observed distributions.

In case the DOPO output is measured, the kurtosis distribution is no longer flat and exhibits an oscillating behaviour. For the squeezed quadrature the kurtosis is approximately equal to zero, but clear deviations from a Gaussian ($K_\theta > 0$) are observed for the anti–squeezed quadrature. This behaviour becomes more and more evident when the threshold is approached. In Fig. (5.5) are reported the $p(x, \theta_n)$ variance and Kurtosis versus the phase BIN. For low pump level the Kurtosis keeps below 0.15 for any θ_n while for powers close to the threshold (upper plot) K_θ reaches $0.4 \div 0.5$ in correspondence of the two variance maxima. In all the acquisitions K_θ is practically 0 in correspondence of variance minima. Even in the Kurtosis analysis, deviations from Gaussianity are less evident when $\eta_{out} = 0.5$. This could indicate a less critical influence of $\mathcal{E}$ as the coupling efficiency is enhanced.

5.3 Theoretical model

The experimental behavior can be connected to residual fluctuations of the OPO parameters. Due to small changes in the crystal temperature T, the laser pump amplitude A_p or the cavity resonance ψ, the effective threshold P_{th} fluctuates.

These fluctuations transform a constant coefficient Langevin equation [21] into a time dependent one:

$$\frac{da}{dt} = (\mathcal{E} + \delta\mathcal{E}(t))\, a^\dagger - (\gamma_M + i\psi + i\delta\psi(t))\, a + \sqrt{2\gamma_1} a_1^{in} + \sqrt{2\gamma_2} a_2^{in} \tag{5.39}$$

with $\gamma_M = \gamma_1 + \gamma_2$ the total damping rate and $a_{1/2}^{in}$ is the delta correlated vacuum entering in the cavity due to the output mirror/extra losses. The time dependent terms $\delta\psi(t)$ and $\delta\mathcal{E}(t)$ are Gaussianly distributed and represent respectively the fluctuations around the stationary detuning ψ and parametric gain $\mathcal{E}$. Ignoring the fluctuations the field a generated inside the OPO inherits the Gaussian statistics of the input vacuum a^{in} thus giving rise to squeezed vacuum. When $\delta\psi(t)$ and $\delta\mathcal{E}(t)$ are switched on, in

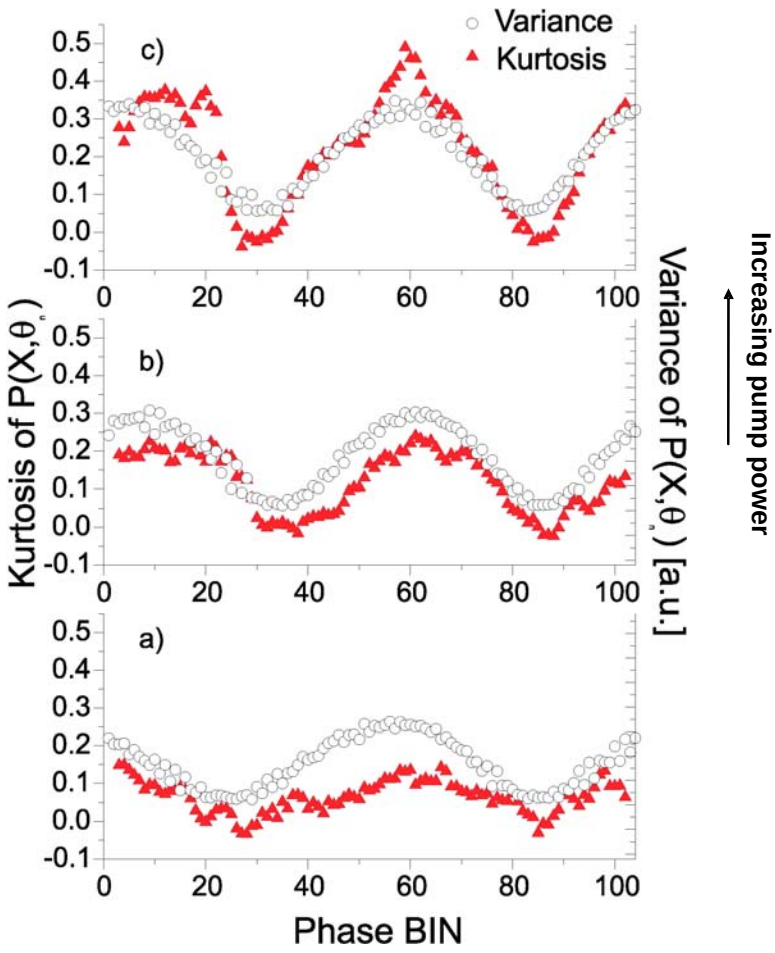

Figure 5.5. Kurtosis of $p\,(x,\theta)$ (red triangles) for three homodyne data sets: $\mathcal{E}=0.5$ (a), 0.8 (b) and 0.95 (c) and η_{out} =0.4. Empty circles indicate the quadrature variance (given in a.u.) for the same $\mathcal{E}$. The phase BIN at which the variance and the Kurtosis are maximum coincides. The Kurtosis goes practically to 0 in correspondance of variance minima. The highest Kurtosis is $K=0.5$ for $\mathcal{E}$= 0.95. In this case the relative deviation between ϱ_{00} and p_0 (see text for details) reaches 10%.

the explicit expression of a they are multiplied the input a^{in}; since the product of two Gaussian process is no longer Gaussian [40] , a deviates from the Gaussian state the more the greater $\overline{\delta\psi^2}$ and $\overline{\delta\mathcal{E}^2}$ are.

The contribution $\delta\psi\left(t\right)$ in (5.39) is physically due to the residual errors of the system controlling the OPO cavity length.

The parametric gain $\mathcal{E}$ linearly depends on the laser pump amplitude A_p times the non linear coefficient E_{NL} that is in turn a function of the phase mismatch $\Delta k\left(\boldsymbol{\lambda},T\right)$ (see previous chapters) [59] . The fluctuation $\delta\mathcal{E}$ can be written as,

$$\delta\mathcal{E}\left(t\right)=\mathcal{E}\left(\frac{\delta A_p}{A_p}-\frac{\delta T^2}{\Delta T^2}\right)$$

where it is stressed the dependence on the pump amplitude $\frac{\delta A_p}{A_p}$ and on the crystal temperature $\frac{\delta T^2}{\Delta T^2}$ fluctuations. In the following the latter ones will be ignored since fluctuate much more slowly than δA_p and $\delta\psi$.

5.4 Zeroth order generation of STV states

By ignoring $\delta\psi$ and $\delta\mathcal{E}$, Eq. (5.39) and its adjoint reduce to the time independent DOPO ones so that the zeroth order solutions $a^{(0)}$ are the STV states seen in previous chapters. In the frequency domain, with the matrix formalism $\tilde{\mathbf{a}}\left(\omega\right)\equiv\left[\begin{array}{c}\tilde{a}\left(\omega\right)\\ \tilde{a}^{\dagger}\left(-\omega^{*}\right)\end{array}\right]$ they can be expressed as:

$$\tilde{\mathbf{a}}^{(0)}=\tilde{\mathbf{G}}\cdot\sqrt{2\gamma_M}\tilde{\mathbf{b}}^{in}$$

with

$$\sqrt{2\gamma_M}\tilde{\mathbf{b}}^{in}=\sqrt{2\gamma_1}\tilde{\mathbf{a}}_1^{in}+\sqrt{2\gamma_2}\tilde{\mathbf{a}}_2^{in}$$

and $\tilde{\mathbf{G}}$ the matrix of the Fourier transformed Green functions for (5.39). It can be re-expressed as $\tilde{\mathbf{G}}=\tilde{\mathbf{g}}/\tilde{D}\left(\omega\right)$ with:

$$\tilde{\mathbf{g}}\left(\omega\right)\;=\;\left[\begin{array}{cc}\gamma_M+i\left(\omega-\psi\right) & \mathcal{E}\\ \mathcal{E} & \gamma_M+i\left(\omega+\psi\right)\end{array}\right],$$

$$\tilde{D}(\omega) = -\left(\omega - i\omega_{+}^{OPO}\right)\left(\omega - i\omega_{-}^{OPO}\right)$$

where

$$\omega_{\pm}^{OPO} = \gamma_M \pm \sqrt{\mathcal{E}^2 - \psi^2} \tag{5.40}$$

5.5 Perturbative solution

Time dependent Eq. (5.39) can be solved by means of an iterative procedure. To this end, it is convenient to introduce the matrix:

$$\tilde{\mathbf{\Delta}} = \begin{bmatrix} i\delta\psi & \delta\mathcal{E} \\ \delta\mathcal{E} & -i\delta\psi \end{bmatrix} \tag{5.41}$$

representing the Gaussian processes $\delta\psi$ and $\delta\mathcal{E}$. The fluctuating terms are characterized by spectral densities

$$\begin{aligned} \overline{\delta\mathcal{E}(\omega)\,\delta\mathcal{E}(\omega')} &= S_{\mathcal{E}}(\omega)\,\delta(\omega+\omega') \\ \overline{\delta\psi(\omega)\,\delta\psi(\omega')} &= S_{\psi}(\omega)\,\delta(\omega+\omega') \end{aligned} \tag{5.42}$$

proportional respectively to the laser pump technical noise and the spectral density of the error signal for the OPO cavity length controller. In (5.42), and it what follows, the bar indicate the average over the $\delta\psi$ and $\delta\mathcal{E}$ degrees of freedom.

Solution of Eq. (5.39) can be expressed in the frequency domain as:

$$\tilde{\mathbf{a}} = \sum_{i=0}^{\infty} \tilde{\mathbf{a}}^{(i)} \tag{5.43}$$

with the terms $\tilde{\mathbf{a}}^{(i)}$ obtained by the recursive formula:

$$\tilde{\mathbf{a}}^{(i)} = \tilde{\mathbf{G}} \cdot \left(\tilde{\mathbf{\Delta}} \otimes \tilde{\mathbf{a}}^{(i-1)}\right) \tag{5.44}$$

The symbol $\otimes$ denotes the convolution in the frequency domain. By repeated application of (5.44), $\tilde{\mathbf{a}}^{(i)}$ in terms of the input vacuum field is:

$$\tilde{\mathbf{a}}^{(i)}(\omega_1) = \sqrt{2\gamma_M}\int_{-\infty}^{\infty} d\omega_{i+1}\, \mathbf{A}^{(i)}(\omega_1, \omega_{i+1}) \cdot \tilde{\mathbf{b}}^{in}(\omega_{i+1}) \qquad i \geq 1$$

with the kernels of the integral operator:

$$\mathbf{A}^{(i)}(\omega_1, \omega_{i+1}) = \prod_{\iota=2}^{i}\int_{-\infty}^{\infty} d\omega_\iota\, \frac{\tilde{\mathbf{g}}^{(i)}(\omega_1, \ldots, \omega_i, \omega_{i+1})}{\tilde{D}(\omega_1)...\tilde{D}(\omega_{i+1})}$$

and

$$\tilde{\mathbf{g}}^{(i)}(\omega_1, \ldots, \omega_i, \omega_{i+1}) = \tilde{\mathbf{g}}(\omega_1) \cdot \tilde{\mathbf{\Delta}}(\omega_1 - \omega_2) \cdot ... \cdot \tilde{\mathbf{g}}(\omega_i) \cdot \tilde{\mathbf{\Delta}}(\omega_i - \omega_{i+1}) \cdot \tilde{\mathbf{g}}(\omega_{i+1}) \tag{5.45}$$

being $\delta(\omega - \omega')$ the Dirac delta function.

The field outside the cavity, obtained by means of the input output relations, is:

$$\tilde{\mathbf{a}}^{out} = \sqrt{2\gamma_1}\,\tilde{\mathbf{a}} - \tilde{\mathbf{a}}_1^{in} = \sum_{i=0}^{\infty} \tilde{\mathbf{a}}^{out\,(i)}$$

where

$$\begin{aligned} \tilde{\mathbf{a}}^{out\,(0)} &= \sqrt{2\gamma_1}\left(\frac{\sqrt{2\gamma_M}}{\tilde{D}(\omega)}\mathbf{g} \cdot \tilde{\mathbf{b}}^{in} - \frac{1}{\sqrt{2\gamma_1}}\tilde{\mathbf{a}}_1^{in}\right) \\ \tilde{\mathbf{a}}^{out\,(i)} &= \sqrt{2\gamma_1}\tilde{\mathbf{a}}^{(i)} \end{aligned}$$

Although an accurate examination of the range of convergence of the series expansion (5.43) goes beyond the limits of the present discussion, it is worth discussing qualitatively the problem by recalling the Fubini-Tonelli inequality for two generic functions $f, g \in C(R)$:

$$\int_{-\infty}^{\infty}\left|\int_{-\infty}^{\infty} f(x-y)\, g(y)\, dy\right| dx \leq \int_{-\infty}^{\infty} |f(x)|\, dx \int_{-\infty}^{\infty} |g(y)|\, dy$$

This result implies that the series (5.43) is convergent if

$$\int_{-\infty}^{\infty} \left| \tilde{\mathbf{g}}\left(\omega+\bar{\omega}\right) \cdot \tilde{\mathbf{\Delta}}\left(\bar{\omega}\right) / \tilde{D}\left(\omega+\bar{\omega}\right) \right| d\bar{\omega} < 1$$

Since $\left| \tilde{D}\left(\omega+\bar{\omega}\right) \right| \geq \omega_{+}^{OPO}\omega_{-}^{OPO}$ then a sufficient condition for the convergence is

$$\int_{-\infty}^{\infty} \left| \tilde{\mathbf{g}}\left(\omega+\bar{\omega}\right) \cdot \tilde{\mathbf{\Delta}}\left(\bar{\omega}\right) \right| d\bar{\omega} < \omega_{+}^{OPO}\omega_{-}^{OPO}$$

Then, approximating $\tilde{\mathbf{\Delta}}\left(\bar{\omega}\right)$ as:

$$\tilde{\mathbf{\Delta}}\left(\bar{\omega}\right) \approx \sqrt{S_{\mathcal{E}}\left(\omega\right)} \begin{bmatrix} 0 & 1 \\ 1 & 0 \end{bmatrix} + i\sqrt{S_{\psi}\left(\omega\right)} \begin{bmatrix} 1 & 0 \\ 0 & -1 \end{bmatrix}$$

one obtains

$$\int_{-\infty}^{\infty} \left| \tilde{\mathbf{g}}\left(\omega+\bar{\omega}\right) \cdot \left(\sqrt{S_{\mathcal{E}}\left(\omega\right)} \begin{bmatrix} 0 & 1 \\ 1 & 0 \end{bmatrix} + i\sqrt{S_{\psi}\left(\omega\right)} \begin{bmatrix} 1 & 0 \\ 0 & -1 \end{bmatrix} \right) \right| d\bar{\omega} \ll \gamma_{M}^{2} - \mathcal{E}^{2} + \psi^{2}$$

that is $S_{\mathcal{E}}\left(\omega\right)$ and $S_{\psi}\left(\omega\right)$ are upper bounded by the distance from the threshold.

5.5.1 Quadratures

The field quadrature can be expanded in a perturbative series similar to (5.43),

$$\tilde{X}_{\theta}\left(\omega\right) = \sum_{i=0}^{\infty} \tilde{X}_{\theta}^{(i)}\left(\omega\right) = \boldsymbol{\theta} \cdot \sum_{i=0}^{\infty} \tilde{\mathbf{a}}^{(i)}\left(\omega\right) \tag{5.46}$$

with $\boldsymbol{\theta}$ the row vector

$$\boldsymbol{\theta} = \begin{bmatrix} \frac{1}{2}e^{-i\theta} & \frac{1}{2}e^{i\theta} \end{bmatrix}$$

Explicitly:

$$\tilde{X}_{\theta}^{(i)}\left(\omega_1\right) = \sqrt{2\gamma_M} \int_{-\infty}^{\infty} d\omega_{i+1}\, \mathbf{X}_{\theta}^{(i)}\left(\omega_1, \omega_{i+1}\right) \cdot \mathbf{b}^{in}\left(\omega_{i+1}\right) \tag{5.47}$$

with the kernel of the integral operator in (5.47) expressed as:

$$\mathbf{X}_{\theta}^{(i)}\left(\omega_1,\omega_{i+1}\right)=\prod_{\iota=2}^{i}\int_{-\infty}^{\infty}d\omega_{\iota}\,\frac{\boldsymbol{\theta}\cdot\tilde{\mathbf{g}}^{(i)}\left(\omega_1,\ldots,\omega_i,\omega_{i+1}\right)}{\tilde{D}\left(\omega_1\right)...\tilde{D}\left(\omega_{i+1}\right)}$$

The output state quadrature is:

$$\tilde{X}_{\theta}^{out}=\sqrt{2\gamma_1}\sum_{i=0}^{\infty}\tilde{X}_{\theta}^{(i)}-\sqrt{\frac{\gamma_1}{\gamma_M}}\tilde{X}_{\theta}^{(in)} \tag{5.48}$$

The quantity actually measured is reproduced from (5.48) by accounting for the detection effect. Quadratures $\tilde{X}_{\theta}^{out}$ are detected by a balanced optical homodyne and the relative current is demodulated at the frequency Ω and integrated for a time $1/\gamma_f$. the resulting output signal is:

$$\begin{aligned}s_{\theta}\left(t\right) &= \int_{-\infty}^{t}e^{-\gamma_f(t-t')}X_{\theta}^{out}\left(t'\right)\cos\left(\Omega t'\right)dt'\\ &= \int_{-\infty}^{\infty}H^{SA}\left(\omega_1,t\right)\tilde{X}_{\theta}^{out}\left(\omega_1\right)e^{i\omega_1 t}d\omega_1\end{aligned}$$

with

$$H^{SA}\left(\omega,t\right)=H^{SA\,\ddagger}\left(\omega,t\right)=-i\left(\frac{e^{-i\Omega t}}{\omega-\Omega-i\gamma_f}+\frac{e^{i\Omega t}}{\omega+\Omega-i\gamma_f}\right)$$

5.6 Kurtosis calculation

The Gaussianity of the OPO output state is checked by looking at the Kurtosis K_{θ} for the quadrature distribution. In terms of $s\left(t\right)$ the Kurtosis is:

$$K_{\theta}=\frac{\overline{s_{\theta}^4}-3\left(\overline{s_{\theta}^2}\right)^2}{\left(\overline{s_{\theta}^2}\right)^2} \tag{5.49}$$

where the quantities $\overline{s_\theta^2}$ and $\overline{s_\theta^4}$ are respectively the second and fourth order moments for $\tilde{X}_\theta^{out}$. By making use of (5.46):

$$\begin{aligned}
\overline{s_\theta^2} &= \overline{\sum_n \sum_{\substack{i,j \\ i+j=n}} s_\theta^{(i,j)}(t)} \\
\overline{s_\theta^4} &= \overline{\sum_n \sum_{\substack{i,j,k,l \\ i+j+k+l=n}} s_\theta^{(i,j,k,l)}(t)}
\end{aligned} \tag{5.50}$$

being n the order of the expansion for the moment under scrutiny and:

$$s_\theta^{(i,j)}(t) = \prod_{m=I}^{II} \int_{-\infty}^{+\infty} d\omega_1^m H^{SA}(\omega_1^m, t) \quad e^{i\left(\omega_1^I + \omega_1^{II}\right)t} \left\langle \tilde{X}_\theta^{out(i)}\left(\omega_1^I\right) \tilde{X}_\theta^{out(j)}\left(\omega_1^{II}\right) \right\rangle$$

and

$$\begin{aligned}
s_\theta^{(i,j,k,l)}(t) &= \prod_{m=I}^{IV} \int_{-\infty}^{+\infty} d\omega_1^m H^{SA}(\omega_1^m, t) \quad e^{i\left(\omega_1^I + \omega_1^{II} + \omega_1^{III} + \omega_1^{IV}\right)t} \\
&\left\langle \tilde{X}_\theta^{out(i)}\left(\omega_1^I\right) \tilde{X}_\theta^{out(j)}\left(\omega_1^{II}\right) \tilde{X}_\theta^{out(k)}\left(\omega_1^{III}\right) \tilde{X}_\theta^{out(l)}\left(\omega_1^{IV}\right) \right\rangle
\end{aligned}$$

In the previous expressions $\langle .. \rangle$ denotes the quantum average.

Without loosing in generality the denominator of (5.49) can be approximated with the 0-th order solution $s_\theta^{(0,0)}(t)$. In general, $\overline{s_\theta^2}$ and $\overline{s_\theta^4}$ are computed by exploiting the properties of Gaussianity for the quantity $\mathbf{b}^{in}(\omega)$ and $\delta\mathcal{E}(t)$ and $\delta\psi(t)$. The details of the calculation will not be reported here, only a qualitative analysis of them being proposed (for a more exhaustive analysis see Re.. [66]).

5.6.1 Quantum average calculation

To compute K_θ the quantum averages $\left\langle \tilde{X}^{out(i)} \tilde{X}^{out(j)} \right\rangle$ and $\left\langle \tilde{X}^{out(i)} \tilde{X}^{out(j)} \tilde{X}^{out(k)} \tilde{X}^{out(l)} \right\rangle$ must be evaluated. As shown by relation (5.47), $\tilde{X}_\theta$ is given by applying an integral operator to the input vacuum $\mathbf{b}^{in}$. This means that the quadrature products in (5.50) are proportional to the product of two or four vacuum operator $\tilde{b}^{in}(\omega)$, $\tilde{b}^{in\dagger}(-\omega^*)$ respec-

tively. Since $\mathbf{b}^{in}$ is Gaussian distributed the quantum average product of four quadratures can be reduced to the sum of three products of two quadratures [40] :

$$\left\langle \tilde{X}\left(\omega^{I}\right)\tilde{X}\left(\omega^{II}\right)\tilde{X}\left(\omega^{III}\right)\tilde{X}\left(\omega^{IV}\right)\right\rangle = 3\left\langle \tilde{X}\left(\omega^{I}\right)\tilde{X}\left(\omega^{II}\right)\right\rangle \left\langle \tilde{X}\left(\omega^{III}\right)\tilde{X}\left(\omega^{IV}\right)\right\rangle \tag{5.51}$$

so that only two quadratures product quantum averages must be calculated.

The properties of the input vacuum also guarantee that, in each product $\left\langle \tilde{X}_{\theta}^{(i)}\tilde{X}_{\theta}^{(j)}\right\rangle$, only the terms with $\tilde{b}^{in}$ on the left and $\tilde{b}^{in\dagger}$ on the right will survive with $\tilde{b}^{in}$ delta correlated. The product of two quadratures is thus simplified into:

$$\left\langle \tilde{X}_{\theta}^{(i)}\left(\omega_1^{I}\right)\tilde{X}_{\theta}^{(j)}\left(\omega_1^{II}\right)\right\rangle = \tilde{X}_{\theta}^{(i,j)}\left(\omega_1^{I},\omega_1^{II}\right)$$

where:

$$\tilde{X}_{\theta}^{(i,j)}\left(\omega_1^{I},\omega_1^{II}\right) = 2\gamma\int_{-\infty}^{\infty} d\bar{\omega}\; X_{\theta\alpha}^{(i)}\left(\omega_1^{I},\bar{\omega}\right)X_{\theta\beta}^{(j)}\left(\omega_1^{II},-\bar{\omega}\right) \tag{5.52}$$

having indicated with

$$X_{\theta\alpha/\beta}^{(i)}\left(\omega_1^{I},\bar{\omega}\right) = \mathbf{X}_{\theta}^{(i)}\left(\omega_1^{I},\omega_{i+1}\right)\cdot\boldsymbol{\alpha}/\boldsymbol{\beta}$$

with $\boldsymbol{\alpha} = \begin{pmatrix} 1 \\ 0 \end{pmatrix}, \boldsymbol{\beta} = \begin{pmatrix} 0 \\ 1 \end{pmatrix}$.

In particular for the field outside the cavity:

$$\begin{aligned}
\tilde{X}_{\theta}^{out(i,j)}\left(\omega_1^{I},\omega_1^{II}\right) &= 2\gamma_1\tilde{X}_{\theta}^{(i,j)}\left(\omega_1^{I},\omega_1^{II}\right)+\frac{1}{4}\delta\left(\omega_1^{I}+\omega_1^{II}\right)+ \\
&-\sqrt{\frac{\gamma_1}{2}}e^{i\theta}\delta_{0j}\int_{-\infty}^{+\infty}d\omega_1^{II}X_{\theta\alpha}^{(i)}\left(\omega_1^{I},-\omega_1^{II}\right) \\
&-\sqrt{\frac{\gamma_1}{2}}e^{-i\theta}\delta_{0i}\int_{-\infty}^{+\infty}d\omega_1^{I}X_{\theta\beta}^{(j)}\left(\omega_1^{II},-\omega_1^{I}\right)
\end{aligned}$$

where δ_{0j} is the Kronecker delta.

5.6.2 Time average

A further simplification concerns with the average over $\delta\mathcal{E}$ and $\delta\psi$ degree of freedom. Since the quantities $\delta\mathcal{E}$ and $\delta\psi$ are Gaussian processes the odd moments for their distributions are all equal to zero and do not contribute to the calculus of the kurtosis. Since each term of order i in the expression (5.46) contributes with a power i of $\delta\mathcal{E}$ and $\delta\psi$, the expansion (5.50) for $\overline{s_\theta^2}$ and $\overline{s_\theta^4}$ simplify to:

$$\begin{aligned}
\overline{s_\theta^2} &= \overline{\sum_n \sum_{\substack{i,j \\ 2n=i+j}} s_\theta^{(i,j)}(t)} \\
\overline{s_\theta^4} &= \overline{\sum_n \sum_{2n=i+j+k+l} s_\theta^{(i,j,k,l)}(t)}
\end{aligned}$$

In the following expansion up to the 2-th order will be considered ($n \leq 1$). The case of higher orders is discussed in reference [66] .

For $n \leq 1$, the only terms admitted in the second order moment are $s_\theta^{(0,0)}$ and $s_\theta^{(1,1)}$, while contribute to the $\overline{s_\theta^4}$, all the $s_\theta^{(i,j,k,l)}$ whose indexes (i,j,k,l) are permutation of the vector $(0,0,1,1)$. However, since the Kurtosis is given by the difference between $\overline{s_\theta^4}$ and $\left(\overline{s_\theta^2}\right)^2$ the terms $(0,0,1,1)$ and $(1,1,0,0)$ in $\overline{s_\theta^4}$ while cancel with those obtained by evaluating $\left(\overline{s_\theta^2}\right)^2 = \left(s_\theta^{(0,0)} + s_\theta^{(1,1)}\right)^2$ so that the only contribution will come from $\left\langle X_\theta^{out}(1) X_\theta^{out}(0) \right\rangle$ and $\left\langle X_\theta^{out}(0) X_\theta^{out}(1) \right\rangle$.

Since $\delta\psi$ and $\delta\mathcal{E}$ are delta correlated, results similar to those for the quantum average are obtained for the arguments of the $\mathbf{\Delta}$ matrixes contained in (5.45). Moreover, it is in particular possible to show [66] that the frequency sums $\sum_m \omega_1^m$ are equal to zero, so that the fluctuating terms $e^{i\left(\omega_1^I+\omega_1^{II}\right)t}$ and $e^{i\left(\omega_1^I+\omega_1^{II}+\omega_1^{III}+\omega_1^{IV}\right)t}$ will be skipped in the following.

Eventually the time average in the moments $\overline{s_\theta^4}$ and $\left(\overline{s_\theta^2}\right)^2$ must be performed. By considering the explicit expression for $H^{SA}(\omega_1^m, t)$, it is readily seen that in the product $\prod_m H^{SA}(\omega_1^m, t)$ will appear terms proportional to 1, $e^{\pm i2\Omega t}$ and $e^{\pm i4\Omega t}$. Since the demodulation frequency Ω is usually very high ($\sim$MHz), only the terms proportional

to 1 will give a significatively non zero mean value in the time average. The product $H^{SA}\left(\omega_1^I,t\right)H^{SA}\left(\omega_1^{II},t\right)$ is thus rewritten as:

$$H^{SA}\left(\omega_1^I,t\right)H^{SA}\left(\omega_1^{II},t\right)=\sum_{\substack{\sigma^I,\sigma^{II}\\ \sigma^I+\sigma^{II}=0}}\frac{e^{i\left(\sigma^I+\sigma^{II}\right)\Omega t}}{\left(\omega_1^I+\sigma^I\Omega-i\gamma_f\right)\left(\omega_1^I+\sigma^{II}\Omega-i\gamma_f\right)}$$

with the right sides summed over $\sigma^p=\pm1$, and an analogous expression holding for $\prod_{m=I}^{IV}H^{SA}\left(\omega_1^m,t\right)$. By taking into account these simplifications, it is convenient to introduce the quantities:

$$\overline{s^{(i,j)}_{\theta,(\sigma^I,\sigma^{II})}}=\prod_{m=I}^{II}\int_{-\infty}^{+\infty}d\omega_1^m\frac{e^{i\left(\sigma^I+\sigma^{II}\right)\Omega t}\,\overline{\tilde{X}_\theta^{out\,(i,j)}\left(\omega_1^I,\omega_1^{II}\right)}}{\left(\omega_1^I+\sigma^I\Omega-i\gamma_f\right)\left(\omega_1^{II}+\sigma^{II}\Omega-i\gamma_f\right)} \tag{5.53}$$

and

$$\begin{aligned}&\overline{s^{(i,j,k,l)}_{\theta,(\sigma^I,\sigma^{II},\sigma^{III},\sigma^{IV})}}\\ &=\;3\prod_{m=I}^{II}\int_{-\infty}^{+\infty}d\omega_1^m\frac{e^{i\left(\sigma^I+\sigma^{II}+\sigma^{III}+\sigma^{IV}\right)\Omega t}\,\overline{\tilde{X}_\theta^{out(i,j)}\left(\omega_1^I,\omega_1^{II}\right)\tilde{X}_\theta^{out(k,l)}\left(\omega_1^{III},\omega_1^{IV}\right)}}{\left(\omega_1^m+\sigma^m\Omega-i\gamma_f\right)}\end{aligned} \tag{5.54}$$

The Kurtosis can be easily rewritten in terms of (5.53) and (5.54) as:

$$\begin{aligned}K_\theta\;&=\;\frac{\overline{s_\theta^4}-3\overline{s_\theta^2}^2}{\left(s_\theta^{(0)2}\right)^2}\\ &=\;\frac{1}{\sum_\sigma s^{(0,0)}_{\theta,(\sigma^1,\sigma^2)}s^{(0,0)}_{\theta,(\sigma^3,\sigma^4)}}\sum_{n=0}^{2}\sum_{\substack{i,j,k,l\\ i\neq j,k\neq l\\ 2n=i+j+k+l}}\sum_\sigma\left(\overline{s^{(i,j,k,l)}_{\theta,(\sigma^1,\sigma^2,\sigma^3,\sigma^4)}}-3\overline{s^{(i,j)}_{\theta,(\sigma^1,\sigma^2)}s^{(k,l)}_{\theta,(\sigma^1,\sigma^2)}}\right)\end{aligned}$$

Poles of the integrands of (5.53) and (5.54) are due to product of $\left(\omega_1^m+\sigma^m\Omega-i\gamma_f\right)$ in $H^{SA}\left(\omega_1^m,t\right)$ with $\prod_i\tilde{D}\left(\omega_i^m\right)$ contained in the $\tilde{X}_\theta^{out\,(i,j)}\left(\omega_1^I,\omega_1^{II}\right)$. The integrations in K_θ can thus be simply calculated, by means of the residues theory, taking into ac-

count the delta correlation due to $\overline{\delta\mathcal{E}^2}$ and $\overline{\delta\psi^2}$ (see (5.42)). It is worth saying that no correlation is expected between $\delta\mathcal{E}$ and $\delta\psi$ so that two contributions can be considered separately.

For a generic perturbative order n, after performing the integration, the Kurtosis takes the form [66] :

$$K_\theta = \frac{4}{\sum_\sigma R^{out(0,0)}_{\theta(\sigma^I,\sigma^{II})} R^{out(0,0)}_{\theta(\sigma^{III},\sigma^{IV})}} \left(\int_{-\infty}^{\infty} d\omega \Delta\tilde{R}^{(1)}_\theta(\omega) + \int_{-\infty}^{\infty} dv_1 \int_{-\infty}^{\infty} dv_2 \Delta\tilde{R}^{(2)}_\theta(v_1, v_2) + \cdots \right) \tag{5.55}$$

where $R^{out(i,j)}_{\theta,(\sigma^I,\sigma^{II})}$ are the sums of residues of $\overline{s^{(i,j)}_{\theta,(\sigma^I,\sigma^{II})}}$ with respect to all the poles. The functions $\Delta\tilde{R}^{(n)}_\theta(\omega)$ in (5.55) can be expressed in terms of $R^{out\ (i,j)}_{\theta,(\sigma^I,\sigma^{II})}$ as:

$$\Delta\tilde{R}^{(n)}_\theta(\omega_1, \omega_2, \ldots, \omega_n) = \sum_{\substack{i,j,k,l \\ 2n=i+j+k+l}} \sum_\sigma \left(\overline{\tilde{R}^{out(i,j)}_{\theta,(\sigma^I,\sigma^{II})} \tilde{R}^{out(k,l)}_{\theta,(\sigma^{III},\sigma^{IV})}} - 3\ \overline{\tilde{R}^{out(i,j)}_{\theta,(\sigma^I,\sigma^{II})}} \overline{\tilde{R}^{out(k,l)}_{\theta,(\sigma^{III},\sigma^{IV})}} \right)$$

For $n \leq 1$ expression (5.55) becomes:

$$K_\theta \approx \frac{4}{\sum_\sigma R^{out(0,0)}_{\theta(\sigma^I,\sigma^{II})} R^{out(0,0)}_{\theta(\sigma^{III},\sigma^{IV})}} \int_{-\infty}^{\infty} d\omega \left(S_\mathcal{E}(\omega) \Delta\tilde{R}^{(1)}_{\theta\mathcal{E}}(\omega) + S_\psi(\omega) \Delta\tilde{R}^{(1)}_{\theta\psi}(\omega) \right) \tag{5.56}$$

where the function $\Delta\tilde{R}^{(1)}_{\theta\mathcal{E}}(\omega)$ and $\Delta\tilde{R}^{(1)}_{\theta\psi}(\omega)$ are obtained by collecting in the $\Delta\tilde{R}^{(1)}_\theta$ the terms proportional to $S_\mathcal{E}(\omega)$ and $S_\psi(\omega)$

5.6.3 Numerical simulations results

The behaviour of (5.56) is strongly dependent on the shape of the spectral densities $S_\mathcal{E}(\omega)$ and $S_\psi(\omega)$. Nevertheless, some preliminar results can be obtained by the analysis of functions $\Delta\tilde{R}^{(1)}_{\theta\mathcal{E}/\psi}$ for different OPO parameters.

In fig. (5.6) are reported the behaviour of $\Delta\tilde{R}^{(1)}_{\theta\mathcal{E}}(\omega)$ and $\Delta\tilde{R}^{(1)}_{\theta\psi}(\omega)$ as functions of the quadrature angle θ and the frequency ω for zero detuning. The parameters in the simulations have been chosen equal to the experimental ones for $\eta_{out} = 0.4$, with a filter bandwidth $\gamma_f \equiv B$ =1MHz and the demodulation frequency Ω =3MHz. The distance from threshold is $\mathcal{E} = 0.8$. As seen by the plots, the deviations from Gaussianity are

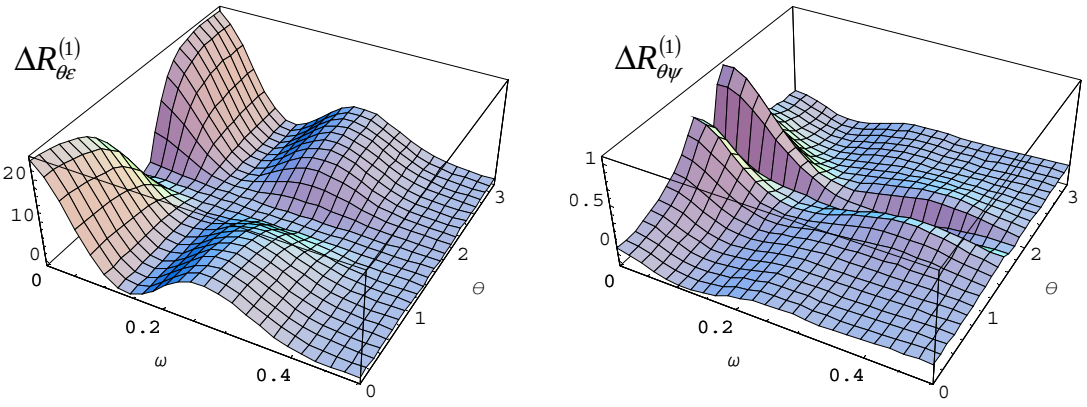

Figure 5.6. Spectral behaviour of $\Delta\tilde{R}^{(1)}_{\theta\mathcal{E}}$ (left) and $\Delta\tilde{R}^{(1)}_{\theta\psi}$ (right) as function of the quadrature angles for $\eta_{out} = 0.4$, $\gamma_f = 0.07$, $\mathcal{E} = 0.8$ and $\Omega = 3MHz$. The frequencies ω are normalized to the cavity bandwidthγ_M. The positive values for $\Delta\tilde{R}^{(1)}_{\theta\mathcal{E}/\psi}$, indicating a deviation from gaussianity, are more evident in the lower frequency region of the spectra and reduce to zero at approximately one half of the cavity bandwidth.

expected to be more evident in the lower part of the spectrum. In general the effect of $\Delta\tilde{R}^{(1)}_{\theta\mathcal{E}/\psi}(\omega)$ vanishes for frequency higher than one half of the cavity bandwidth. It is worth saying that in this region also the effect of the laser pump noise contained in $S_{\mathcal{E}}(\omega)$ is more evident.

Since most interesting results concern the low frequency behaviour in fig. (5.7) are reported $\Delta\tilde{R}^{(1)}_{\theta\mathcal{E}/\psi}(0)$, as functions of the quadrature phase θ (Ω =3MHz, γ_f =1MHz, η_{out} =0.4, ψ =0) at different distances from threshold $\mathcal{E} = 0.95,\ 0.8,\ 0.5$ and for zero cavity detuning ψ.

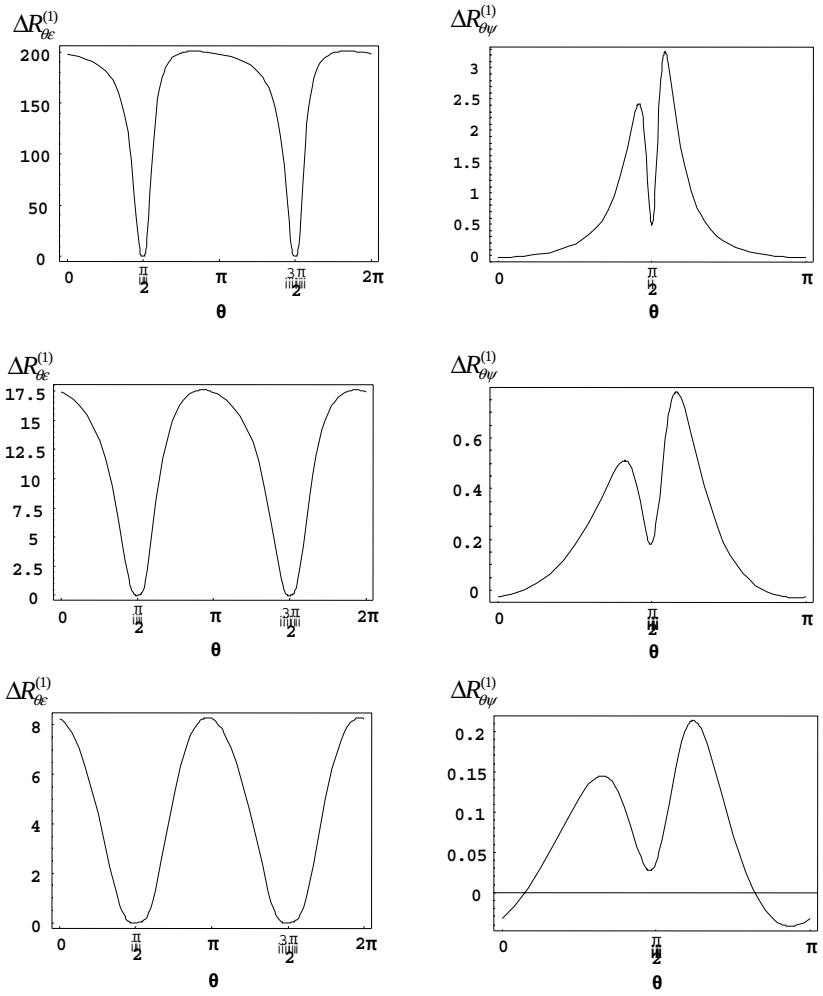

Figure 5.7. Behaviour of $\Delta\tilde{R}^{(1)}_{\theta\mathcal{E}}$ (left) and $\Delta\tilde{R}^{(1)}_{\theta\psi}$ (right) as functions of the quadrature angle θ for different distance from threshold $\mathcal{E} = 0.95$ (up), 0.8 (center), 0.5 (down). The simulation parameters have been chosen equal to the experimental ones for the $\eta_{out} = 0.4$ with a filter bandwidth γ_f =1MHz and the demodulation frequency Ω =3MHz. $\Delta\tilde{R}^{(1)}_{\theta\mathcal{E}/\psi}$ deviations from zero are stronger when the threshold is approached accordingly with experimental finding. Moreover it is possible to recognized in $\Delta\tilde{R}^{(1)}_{\theta\mathcal{E}}$ the oscillatory behaviour seen for the kurtosis, with minima for the squeezed quadrature and maxima for the antisqueezed one.

Accordingly with experimental findings for K_θ, the contribution from $\Delta\tilde{R}^{(1)}_{\theta\mathcal{E}/\psi}$ sharply increases in proximity of the threshold, where the relative effect of threshold fluctuations is stronger. The simulations show that the most important contribution to the Kurtosis is given by the parametric gain fluctuations (two order of magnitude higher than the $\delta\psi$'s one). Moreover $\Delta\tilde{R}^{(1)}_{\theta\mathcal{E}}$ shows the oscillatory behaviour as a function of the quadrature phase θ with minima ($\Delta\tilde{R}^{(1)}_{\theta\mathcal{E}} \approx 0$) corresponding to the squeezed quadrature and maxima to the antisqueezed one.

Functions $\Delta\tilde{R}^{(1)}_{\theta\mathcal{E}/\psi}$ have period equal to π. This a consequence of factors $e^{\pm i4\theta}$ and $e^{\pm i2\theta}$ present in the explicit shape of the function $\Delta\tilde{R}^{(1)}_{\theta\mathcal{E}/\psi}$ [66] :

$$\Delta\tilde{R}^{(1)}_{\theta\mathcal{E}/\psi} \approx 1 + \mathrm{Re}\left[A_{\mathcal{E}/\psi}e^{i4\theta} + B_{\mathcal{E}/\psi}e^{i2\theta}\right] \tag{5.57}$$

Coefficients $A_{\mathcal{E}/\psi}$ and $B_{\mathcal{E}/\psi}$ in (5.57) are determined by the OPO and the detection parameters. Since in general $A_{\mathcal{E}/\psi}$ and $B_{\mathcal{E}/\psi}$ can be complex, the functions $\Delta\tilde{R}^{(1)}_{\theta\mathcal{E}/\psi}$ are not symmetric around $\pi/2$. This behaviour is widely evident in the shape of $\Delta\tilde{R}^{(1)}_{\theta\psi}$ (see fig. (5.7-right column)) and it is accentuated when a non zero detuning ψ is introduced.

In fig. (5.8) are reported the behaviour of $\Delta\tilde{R}^{(1)}_{\theta\mathcal{E}/\psi}(0)$ for ψ =0, 0.15, 0.25 ($\mathcal{E} = 0.8$, Ω =3MHz, γ_f =1MHz, $\eta_{out} = 0.4$). For increasing detuning, the effect of $\delta\mathcal{E}$ is reduced. This is due to the fact that for non perfect resonance, the interference for each wave bouncing back and forth inside the cavity is not optimized. This effect turns out in a lower effective cavity Q-factor and in turn an higher threshold; for the same injected pump power, the greater is ψ, the more the system is far from its effective threshold.

Eventually the effect of the detector is evaluated by considering three different choices of the filter bandwidth γ_f =1MHz, 2.5MHz, 100kHz (see fig. (5.9)) ($\mathcal{E} = 0.8$, Ω =3MHz, $\eta_{out} = 0.4$, $\psi = 0$) Most interesting results concern with $\Delta\tilde{R}^{(1)}_{\theta\mathcal{E}}$ that is drastically reduced when the filter is clenched around the demodulation frequency Ω. This effect is due to the fact that for wider γ_f, more spectral components are included in the integration performed by the detector, so enhancing the obtained noise. It is worth noting that when the demodulation frequency is moved in the spectral region on the

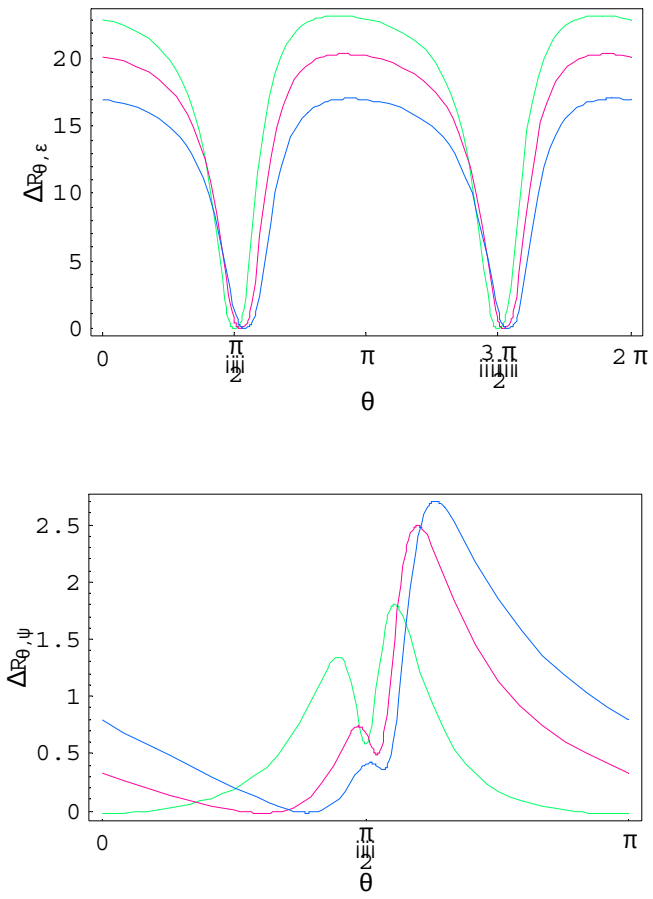

Figure 5.8. Behaviour of $\Delta\tilde{R}^{(1)}_{\theta\mathcal{E}}$ (up) and $\Delta\tilde{R}^{(1)}_{\theta\psi}$ (down) as function of the quadrature angle θ for ψ =0 (green), 0.15 (red), 0.25 (blu) ($\mathcal{E}$ =0.8, Ω =3MHz, γ_f =1MHz, η_{out} =0.4). The detuning enhances the asimmetry around $\pi/2$ for $\Delta\tilde{R}^{(1)}_{\theta\psi}$ and due to its effect on the effective threshold, reduces $\Delta\tilde{R}^{(1)}_{\theta\mathcal{E}}$.

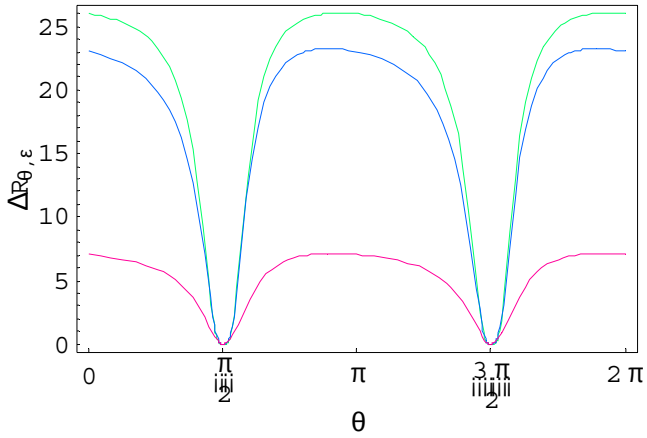

Figure 5.9. Behaviour of $\Delta\tilde{R}^{(1)}_{\theta\mathcal{E}}$ as function of the quadrature angle θ ($\mathcal{E} = 0.8$, Ω =3MHz, $\eta_{out} = 0.4$, $\psi = 0$) for $\gamma_f = 2.5$MHz (green),1MHz (blu) and 100kHz (red).

border of the cavity linewidth ($\Omega \approx \gamma_M$), the use of a wide γ_f will suffer of the effect of cavity filter, that flattens the spectral component to the shot noise level and corrupt the $\Delta\tilde{R}^{(1)}_{\theta\mathcal{E}/\psi}$ shape with respect to the case of narrower γ_f.

After these preliminar results, the computation of the kurtosis for assigned $S_{\mathcal{E}/\psi}(\omega)$ will be considered. It is worth noting that the entire iterative procedure can be also applied to the case of non degenerate OPO, so to evaluate the effect of fluctuations on the entangled between the generated signal and idler modes. Work along this direction is in progress.

Chapter 6:
Transmittivity measurement with squeezed vacuum

Traditional optical measurements of the transmittivity $\mathcal{T}$ are performed by sending on the absorbing sample a probe beam in a coherent state. The value of $\mathcal{T}$ is retrieved by detecting the beam intensity up and down-stream the sample and comparing the obtained results. Sufficient accuracy is achieved by using beams so intense to contrast the shot-noise effect and provide a good signal to noise ratio SNR. However, in some circumstances, using high input intensity is either not useful (in case of very low absorption) or unwise (strongly non-linear materials or samples whose structure may be altered by intense photon fluxes).

Many experimental schemes have provided an upgrade of traditional one by making use of squeezed light radiation. Most of them, used as probe beam a combination of squeezed vacuum with a coherent field set in a well defined phase relation [19] , [20] . Even in these cases, the observable is the field intensity but, due to the presence of the squeezing, the ultimate the limit of shot noise level is beaten..

A further enhancement, in terms of the dose transferred to the sample, is proposed by neglecting the coherent component and using as a probe directly the squeezed vacuum radiation [27] .

As discussed above, below–threshold DOPOs produce *e.m.* radiation in squeezed–thermal–vacuum states (STV) with a Gaussian statistics [54] . Propagation through non resonant media transforms an STV state into another one with different quadrature variances ΔX_θ^2; the trasmittivity $\mathcal{T}$ of the sample can be measured by exploiting the change of ΔX_θ^2. The combination with the coherent light is deplaced down-stream the sample, where it acts as local oscillator in a balanced homodyne detector. Since the detected signal is proportional to X_θ times the LO amplitude, the detection noise can be neglected also in case of very weak beams so that the effects of the SNR on the accuracy can be disregarded.

Essential to the proposed method is the use of a Gaussian distributed quadrature X_θ. This means that for testing the method it is necessary to preliminarily measure the distribution function by sampling X_θ an adequate number N of times. In alternative, it is also possible to determine the whole Wigner function with quantum homodyne tomography (QHT) using samples uniformly distributed over the whole interval $(0, 2\pi)$.

6.1 Propagation of STV states through the sample

The OPO output is characterized by means of the adimensional parameters $n_{th}, n_{sq} = \sinh^2 r$ representing the average number of thermal and squeezed photons, respectively (see previous chapters). The values of n_{th} and n_{sq} are set by the OPO working conditions. In terms of n_{th} and n_{sq}, the mean total photon number is given by:

$$N_{tot} = n_{sq} + n_{th} + 2n_{sq}n_{th}\,, \tag{6.58}$$

while the variance of the generic quadrature X_θ reads:

$$\Delta X_\theta^2 = \frac{(2n_{th}+1)}{4}\left(1 + 2n_{sq} + 2\sqrt{(1+n_{sq})\,n_{sq}}\cos 2\theta\right)\,. \tag{6.59}$$

The STV states are described by a Gaussian Wigner function centered at the origin [67] :

$$\begin{aligned} W(\alpha) &= \frac{1}{2\pi\sqrt{\Delta X^2 \Delta Y^2}}\exp\left(-\frac{\Re[\alpha]^2}{2\Delta X^2} - \frac{\Im[\alpha]^2}{2\Delta Y^2}\right) \\ &= \frac{2}{\pi}\int P(\beta)\exp\left(-2\left|\alpha-\beta\right|^2\right)d^2\beta\,, \end{aligned}$$

with $P(\beta)$ the corresponding P-representation:

$$P(\beta) = \frac{1}{2\pi\sqrt{\left(\Delta X^2 - \frac{1}{4}\right)\left(\Delta Y^2 - \frac{1}{4}\right)}}\exp\left(-\frac{\Re[\beta]^2}{2\left(\Delta X^2 - \frac{1}{4}\right)} - \frac{\Im[\beta]^2}{2\left(\Delta Y^2 - \frac{1}{4}\right)}\right)$$

corresponding to a density matrix:

$$\varrho = \int P(\alpha) |\alpha\rangle \langle\alpha| \, d^2\alpha$$

If the STV is sent through a medium of transmittivity $\mathcal{T}$, the density matrix for the state down stream the sample modifies as

$$\varrho_{\mathcal{T}} = \int P(\alpha) \left|\sqrt{\mathcal{T}}\alpha\right\rangle \left\langle\sqrt{\mathcal{T}}\alpha\right| d^2\alpha = \int P_{\mathcal{T}}(\alpha) |\alpha\rangle \langle\alpha| \, d^2\alpha \,,$$

with

$$\begin{aligned} P_{\mathcal{T}}(\alpha) &= \frac{1}{\mathcal{T}} P\left(\frac{\alpha}{\sqrt{\mathcal{T}}}\right) \\ &= \frac{1}{2\pi\sqrt{\left(\Delta X_{\mathcal{T}}^2 - \frac{1}{4}\right)\left(\Delta Y_{\mathcal{T}}^2 - \frac{1}{4}\right)}} \exp\left(-\frac{\Re[\alpha]^2}{2\left(\Delta X_{\mathcal{T}}^2 - \frac{1}{4}\right)} - \frac{\Im[\alpha]^2}{2\left(\Delta Y_{\mathcal{T}}^2 - \frac{1}{4}\right)}\right), \end{aligned}$$

and

$$\Delta X_{\mathcal{T}}^2 - \frac{1}{4} = \mathcal{T}\left(\Delta X^2 - \frac{1}{4}\right). \tag{6.60}$$

A similar expression is found for $\Delta Y_{\mathcal{T}}^2$ [16]. Introducing the subfixes 0 and $\mathcal{T}$ for labelling up– and down–stream quantities, respectively, Eq. (6.60) generalizes for a generic quadrature X_θ into:

$$\Delta X_{\theta,\mathcal{T}}^2 - \frac{1}{4} = \mathcal{T}\left(\Delta X_{\theta,0}^2 - \frac{1}{4}\right) \tag{6.61}$$

Previous equations show that after the propagation through the sample, the STV state is transformed into a new STV with quadrature variances given by (6.61). Physically $\Delta X_\theta^2 - \frac{1}{4}$ quantifies the deviation of the actual STV variance from the vacuum state case (shot–noise). The absorber deteriorates the quality of the squeezed state; in the

[16] In principle, in the absence of multiple reflections within the sample, the transmittivity T is given by $T = T_1 T_{slab} T_2$, where T_1 and T_2 are the Fresnel transmission coefficients at the input and output faces of the sample respectively and T_{slab} is the sample internal transmittivity.

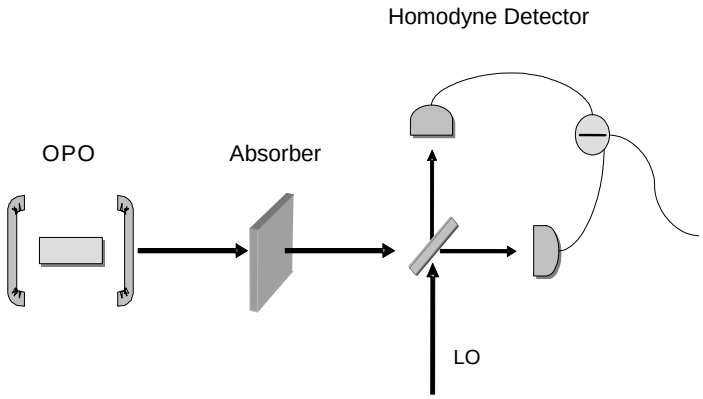

Figure 6.1. Schematic set-up for absorption measurement via quadrature detection. The STV state generated by the OPO is sent to the absorber. The quadrature of the transmitted STV state are characterized by a homodyne detector to retrieve the sample transmittivity.

limit case of $\mathcal{T} = 0$ (complete absorption), the squeezing is completely degraded and the state reduces to a coherent vacuum with shot noise $1/4$.

Equation (6.61) provides a simple way to obtain the sample transmittivity $\mathcal{T}$ by measuring the up– and down–stream quadrature variances:

$$\mathcal{T} = \frac{\Delta X^2_{\theta,\mathcal{T}} - \frac{1}{4}}{\Delta X^2_{\theta,0} - \frac{1}{4}} \tag{6.62}$$

By means of Eqs.(6.59) and (6.62), $\mathcal{T}$ can be also expressed as:

$$\mathcal{T} = \frac{(2n_{th,\mathcal{T}} + 1)\left(1 + 2n_{sq,\mathcal{T}} + 2\sqrt{(1 + n_{sq,\mathcal{T}})\, n_{sq,\mathcal{T}}}\cos 2\theta\right) - 1}{(2n_{th,0} + 1)\left(1 + 2n_{sq,0} + 2\sqrt{(1 + n_{sq,0})\, n_{sq,0}}\cos 2\theta\right) - 1}\,. \tag{6.63}$$

6.1.1 State parameters evolution

The expression for the density matrix of the transmitted state allows writing the evolution of all the state parameters. The mean photon number N_{tot} transforms proportionally to $\mathcal{T}$ as for a classical field:

$$N_{tot,\mathcal{T}} = \mathcal{T}\ N_{tot,0} \tag{6.64}$$

and $n_{th,\mathcal{T}}$ and $n_{sq,\mathcal{T}}$ can be expressed in terms of $\mathcal{T}$ and of the initial values $n_{th,0}$ and $n_{sq,0}$ as:

$$\begin{aligned}
2n_{th,\mathcal{T}} + 1 = & \\
& \sqrt{\left[1 - \mathcal{T} + \mathcal{T}(1 + 2n_{th,0})\,(1 + 2n_{sq,0})\right]^2 - \left[2\mathcal{T}(1 + 2n_{th,0})\sqrt{(1 + n_{sq,0})\,n_{sq,0}}\right]^2} \\
2n_{sq,\mathcal{T}} + 1 = & \\
& \frac{1 - \mathcal{T} + \mathcal{T}(2n_{th,0} + 1)\,(1 + 2n_{sq,0})}{2n_{th,\mathcal{T}} + 1}\,.
\end{aligned} \tag{6.65}$$

These equations provide alternative ways to estimate $\mathcal{T}$. In the measurements discussed below, $\mathcal{T}$ is determined through a direct measurement of the parameters n_{th} and n_{sq} by QHT technique based on pattern functions. This choice is motivated by the fact that for the STV state used in the experimental test ($n_{th,0} = 0.55$ and $n_{sq,0} = 0.11$), $n_{th,\mathcal{T}}$ and $n_{sq,\mathcal{T}}$ are practically linear in $\mathcal{T}$, so that:

$$\begin{aligned}
\frac{n_{th,\mathcal{T}}}{n_{th,0}} &= A_{th} + B_{th}\mathcal{T} \\
\frac{n_{sq,\mathcal{T}}}{n_{sq,0}} &= A_{sq} + B_{sq}\mathcal{T}\,.
\end{aligned} \tag{6.66}$$

The coefficients A and B can be calculated by linearizing Eqs.(6.65) as a function of $\mathcal{T}$ for fixed $n_{th,0}$, $n_{sq,0}$. In table (6.1) computed A and B have been reported (first two columns) together with the corresponding values obtained experimentally (last two

	A	B	A$^{(QHT)}$	B$^{(QHT)}$
N_{tot}	0	1	-0.05±0.07	1.1±0.1
n_{th}	0.12	0.89	0.07±0.05	0.85±0.07
n_{sq}	-0.12	1.14	-0.16±0.05	1.14±0.07

Table 6.1. Coefficients A and B computed by equation (6.69) (left) and experimental ones measured by QHT (right)

columns). For the sake of completeness the measured ratio $N_{tot,\mathcal{T}}/N_{tot,0}$ has been reported as well, in order to evidence the agreement with the theoretical value of Eq.(6.64).

In conclusion, it is worth remarking that the above transformation laws and in turn expressions (6.62) for $\mathcal{T}$ are valid only for Gaussian state. As showed before a Gaussian statistics follows from the assumption of time independent gain and detuning of the OPO with relative deviations decreasing when the DOPO is driven far from threshold. For the used OPO the correctness of Gaussianity assumption is discussed by measuring the kurtosis parameter K_θ.

6.2 Accuracy of the estimation of $\mathcal{T}$

The limit of the uncertainty on the estimate of $\mathcal{T}$ expressed by Eq.(6.62) depends on the confidence interval $\delta\left[\Delta X_\theta^2\right]$ in the measurement of ΔX_θ^2. Explicitly, the relative error on $\mathcal{T}$ is [27] :

$$\frac{\delta\mathcal{T}}{\mathcal{T}} = \frac{1}{\left|\Delta X_{\theta,0}^2 - \frac{1}{4}\right|}\sqrt{\frac{\delta\left[\Delta X_{\theta,\mathcal{T}}^2\right]^2}{\mathcal{T}^2} + \delta\left[\Delta X_{\theta,0}^2\right]^2}\,. \tag{6.67}$$

In case of Gaussian distributed X_θ, as for the STV, is possible to write:

$$\delta\left[\Delta X_\theta^2\right] = \sqrt{\frac{2}{N}}\Delta X_\theta^2\,,$$

with N the number of acquired data, so that:

$$\frac{\delta\mathcal{T}}{\mathcal{T}} = \sqrt{\frac{2}{N}}\frac{1}{\left|\Delta X_{\theta,0}^2 - \frac{1}{4}\right|}\sqrt{\frac{1}{16}\left(1-\frac{1}{\mathcal{T}}\right)^2 + \frac{1}{2}\left|\Delta X_{\theta,0}^2 - \frac{1}{4}\right|\left(\frac{1}{\mathcal{T}} + 3 + 4\left|\Delta X_{\theta,0}^2 - \frac{1}{4}\right|\right)}\,. \tag{6.68}$$

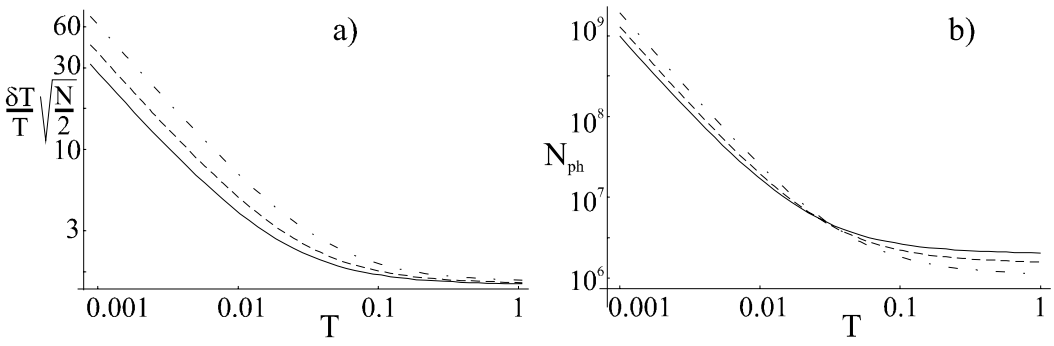

Figure 6.2. Relative error $\frac{\delta\mathcal{T}}{\mathcal{T}}\sqrt{\frac{N}{2}}$ (a) and (b) number $\mathcal{N}$ of photons hitting the sample for $\frac{\delta\mathcal{T}}{\mathcal{T}}$= 0.01 and $\kappa\tau_s$= 6 vs. transmittivity $\mathcal{T}$. The plots refer to the STV state parameter calculated at ω = 0 for the output of a DOPO with zero detuning, at half the threshold ($\mathcal{E}$ = 0.5) and γ_1/γ_M= 0.5, 0.75, 1) (dot-dashed, dashed and full lines)

This expression gives, for a fixed $\mathcal{T}$, the relative error as a function of N and $\Delta X^2_{\theta,0}$ in turns depending on the OPO working condition (distance from the threshold, output coupling and cavity detuning). On the other hand, the total number of photons $\mathcal{N}$ hitting the sample during the measurement is:

$$\mathcal{N} = N_{tot}\,\gamma_M\,N\,\tau_s\,, \tag{6.69}$$

with τ_s^{-1} the sampling rate, γ_M the cavity overall damping ratio and N_{tot} given by Eq.(6.58). Physically $N_{tot}\,\gamma_M$ expresses the flux of photons outing the cavity (γ_M^{-1} is the cavity lifetime) and $N\,\tau_s$ the time needed to acquire the N samples.

In Fig. (6.2-a) $\frac{\delta\mathcal{T}}{\mathcal{T}}\sqrt{\frac{N}{2}}$ (see Eq. 6.68)) has been plotted as a function of the transmittivity $\mathcal{T}$ for $\omega = \psi = 0$, $\mathcal{E} = 0.5$, and three different escape efficiencies ($\eta_{out} = 0.5$, 0.75, 1). The relative error increases for $\mathcal{T}$ approaching zero. Fig.(6.2–b) gives the photon dose $\mathcal{N}$ necessary to obtain a relative error $\frac{\delta\mathcal{T}}{\mathcal{T}} = 0.01$ as a function of $\mathcal{T}$. The OPO parameter are set as in Fig.(6.2-a) and $\gamma_M\tau_s = 6$ (as in the experimental test). The plot evidences the increase of $\mathcal{N}$ by more than an order of magnitude for $\mathcal{T}$ less than 0.01.

6.2.1 $\mathcal{T}$ estimation via quantum homodyne tomography

A different analysis is performed by uniformly varying the LO angle in the interval $0 \leq \theta \leq 2\pi$ so spreading the N data over more quadratures. Experimentally, this

procedure presents the advantage that it does not require sophisticate phase locking set-up to keep θ constant during the N samples acquisition.

Data over 2π be processed by QHT for obtaining the Wigner function and the state parameters mean value (i.e. N_{tot}, n_{th} and n_{sq}). In this case Eq. (6.67) is still valid with $\delta\left[\Delta X_\theta^2\right]$ replaced by $\delta_{QHT}\left[\Delta X_\theta^2\right]$. For the operator $\hat{O} = \Delta X_\theta^2$ the QHT confidence interval reads (see previous chapters)

$$\delta_{QHT}\left[\Delta X_\theta^2\right] = \frac{1}{\sqrt{N}}\sqrt{\overline{\Delta R^2\left[\Delta X_\theta^2\right]}}, \tag{6.70}$$

By considering the explicit expression of the kernel for X_θ and X_θ^2 it is simple to find with some algebra that:

$$\overline{\Delta R^2\left[\Delta \hat{X}_\theta^2\right]} = C_0 + C_1\cos\left(2\theta\right) + C_2\cos\left(4\theta\right)\ , \tag{6.71}$$

with the coefficients C_0, C_1 and C_2 given by:

$$\begin{aligned}
C_0 &= \frac{1}{4}\left[\frac{27}{2}\left(\Delta X^4 + \Delta Y^4\right) + 9\Delta X^2\Delta Y^2 + \left(1 - \frac{3}{\eta}\right)\left(\Delta X^2 + \Delta Y^2\right) + \frac{1}{4}\left(\frac{3}{\eta^2} - \frac{2}{\eta} + 1\right)\right] \\
C_1 &= \frac{1}{2}\left(\Delta X^2 - \Delta Y^2\right)\left[3\left(\Delta X^2 + \Delta Y^2\right) - 1\right] \\
C_2 &= \frac{3}{8}\left(\Delta X^2 - \Delta Y^2\right)^2\ .
\end{aligned}$$

In previous chapters, it is shown that the confidence interval on ΔX_θ^2 obtained via QHT reconstruction is greater than the one obtained in direct measurements. However for the variances $\Delta X^2, \Delta Y^2$ relative to OPO devices similar to that used in the experimental test, $\delta_{QHT}\left[\Delta X_\theta^2\right]$ differs from $\delta\left[\Delta X_\theta^2\right]$ only by some percents. This means that collecting N samples in the interval $(0,\ 2\pi)$ reduces the accuracy with respect to the case of constant phase by only a few percent. This slight loss is largely compensated by a three dimensional characterization of the STV state in the phase space.

6.2.2 Comparison with intensity measurement accuracy

Conventional measurements of $\mathcal{T}$ use a coherent CW probe beams and the radiation power, P, as observable. In this case the estimation of $\mathcal{T}$ is retrieved as the ratio of the power down– and up–stream the sample:

$$\mathcal{T} = \frac{P_{\mathcal{T}}}{P_0} \tag{6.72}$$

The more the dose transmitted to the sample is reduced, the more the measurement is blurred by the shot noise and by the detector noise equivalent power (NEP). The error on P reads:

$$\delta P = \sqrt{\hbar\omega_0 B\, P} + NEP\,, \tag{6.73}$$

with ω_0 the radiation frequency, and B the detection bandwidth. The corresponding to a relative error on $\mathcal{T}$ given by (6.72) is:

$$\frac{\delta\mathcal{T}}{\mathcal{T}} = \frac{1}{SNR}\sqrt{\frac{1}{\mathcal{T}^2}\left(1+\sqrt{\frac{\hbar\omega_0 B}{NEP}\frac{SNR\,\mathcal{T}}{N}}\right)^2 + \left(1+\sqrt{\frac{\hbar\omega_0 B}{NEP}\frac{SNR}{N}}\right)^2}\,, \tag{6.74}$$

with $SNR = P_0/NEP$ and N the number of acquired data.

In analogy with Eq. (6.69), the total number of photons passing through the sample during the measurement interval is given by

$$\mathcal{N} = SNR\frac{NEP}{\hbar\omega_0}\, N\tau_s \tag{6.75}$$

Equation (6.75) allows replacing the factor $\frac{\hbar\omega_0 B}{NEP\,N}$ in Eq. (6.74) with $\frac{SNR\,B\tau_s}{\mathcal{N}}$ (with $B\tau_s > 1$). In this way the ratio $\frac{B\tau_s}{\mathcal{N}}$ can be expressed as a function of $\frac{\delta\mathcal{T}}{\mathcal{T}}$, $\mathcal{T}$ and SNR. Using for SNR the limiting value (corresponding to $N \to +\infty$)

$$SNR \geq \left(\frac{\delta\mathcal{T}}{\mathcal{T}}\right)^{-1}\sqrt{\frac{1}{\mathcal{T}^2}+1}\,,$$

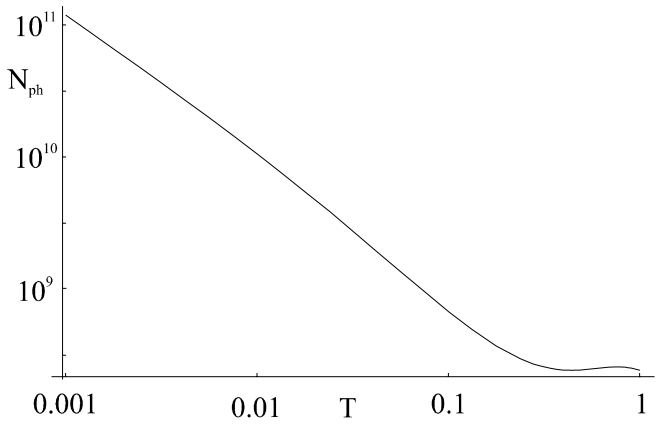

Figure 6.3. Photon dose passing through the sample against $\mathcal{T}$ for transmission measurements based on power measurement up- and down-stream the sample under scrutiny using a coherent beam as a probe. The curve refer to $B\tau_s$ = 10 and $\delta\mathcal{T}/\mathcal{T}$ = 0.01. The required dose increases for low transmittivity but it is always much more intense than the one required for measurement based on quadrature detection (see fig.(6.2))

it has been obtained the plot of Fig. (6.3) representing $\mathcal{N}$ vs. $\mathcal{T}$ for $\frac{\delta\mathcal{T}}{\mathcal{T}} = 0.01$ and $B\tau_s = 10$. Comparing it with Fig. (6.2–b) it appears evident that for obtaining the same accuracy a much lower photon dose (two order of magnitude smaller) is required by the method via quadrature measurement. This results is linked to the fact that in the limit of low photon flux (few pW) with the present detector technology, the NEP on intensity measurement is not negligible so that to achieve a good accuracy the dose has to be raised to guarantee a SNR$\gg 1$. This problem is completely by-passed in homodyne detection where since the LO amplifies the signal, the effect of detector noise can be neglected even for low doses transferred to the sample.

Concerning with the use of squeezed light in transmittivity measurement, it is worth mentioning the case Re.. [20] . In this case the probe beam is given by a coherent beam (a_α) mixed with a squeezed thermal vacuum one ($a_{S\mathcal{T}V}$) with θ their locked phase difference; the total field is described by:

$$a_{tot} = e^{i\theta} a_{S\mathcal{T}V} + a_\alpha \,,$$

The transmittivity of the sample is then retrieved via power measurements.

It can be shown after some algebra that the addition of the squeezed component slightly modifies Eq. (6.73) by replacing B with

$$B_{eff} = B\left(1 + n_{sq} + n_{th} + 2n_{sq}n_{th} + \sqrt{(1+n_{sq})\,n_{sq}}\cos 2\theta\right) .$$

For $\cos 2\theta = -1$ and $\sqrt{(1+n_{sq})\,n_{sq}} > n_{sq} + n_{th} + 2n_{sq}n_{th}$ the squeezed vacuum component reduces the effective detector bandwidth. The reduction of B (typically $B_{eff} \gtrsim .5B$) implies a proportional decrease of $\mathcal{N}$ in (6.75) for assigned $\frac{\delta\mathcal{T}}{\mathcal{T}}$ and $\mathcal{T}$.

6.3 Experimental test

The reliability and accuracy of the method is tested with a sample of know variable transmittivity. The $\mathcal{T}$ values obtained via QHT are compared to those measured, with an accuracy of 10^{-4}, with standard techniques employing 1 mW coherent beam at $\lambda = 1064$ nm.

STV states are generated by a degenerate type–I OPO and characterized by a homodyne detector, both described in details in previous chapters [26] ; in the present case, cavity mirrors are in configuration II (cavity linewidth of 15 MHz). Fixing $\mathcal{E} = 0.50$ the reference STV state has $N_{tot,0} = 0.79 \pm 0.06$, $n_{th,0} = 0.55 \pm 0.02$ and $n_{sq,0} = 0.11 \pm 0.01$, corresponding to a photon flux of 10^7 s^{-1}. For this state the measured kurtosis resulted $K_\theta \lesssim 0.01$ for any θ, thus indicating that the corresponding quadrature statistics was very close to the Gaussian one.

The OPO output is propagated through a variable neutral density filter, which changes $\mathcal{T}$ without introducing misalignment, that could reduce the homodyne efficiency. The transmittivity $\mathcal{T}$ is varied between 0.45 and 1 in discrete steps. The beam passing through the non–absorbing zone ($\mathcal{T} = 1$) of the filter is used as a reference state. The field leaving the absorber is sent to the homodyne detector ($\eta = 0.88 \pm 0.02$). The average electrical signal level at the homodyne output is 15 dB higher than the electronic noise. This prevent from the influence of the NEP on the quadrature measurement.

Tomographic data are acquired by sampling the homodyne signal. To avoid laser technical noise, data sampling is performed by demodulation the homodyne current at $\Omega = 5$ MHz. Then, the resulting current is low–pass filtered, with a cut–off frequency of 2.5 MHz, and 10^6 samples are collected at 2.5 Msample/s ($\tau_s = 400$ ns).

In order to reduce the influence of residual fluctuations of the STV state, each experimental point was averaged over multiple ($\sim$5) tomographic acquisitions. In the present conditions the QHT error was negligible with respect to the standard deviations of the STV state parameters.

To assess the robustness of the method, the transmittivity, $\mathcal{T}_{QHT}$, obtained by tomographic reconstruction was compared with the corresponding value, $\mathcal{T}_{st}$, provided by standard intensity measurements.

In Fig. (6.4), $\mathcal{T}_{QHT} = N_{tot,\mathcal{T}}/N_{tot,0}$ (see Eq.(6.64)) is plotted vs. $\mathcal{T}_{st}$ together with the expected behavior $\mathcal{T}_{QHT} = \mathcal{T}_{st}$ (straight line). A linear regression of the data with $\mathcal{T}_{QHT} = A_{tot}^{(QHT)} + B_{tot}^{(QHT)}\mathcal{T}_{st}$, gives $A_{tot}^{(QHT)} = -0.05 \pm 0.07$ and $B_{tot}^{(QHT)} = 1.1 \pm 0.1$ in good agreement with the expected values of $A_{tot} = 0$ and $B_{tot} = 1$ respectively.

The measured value of $n_{sq,\mathcal{T}}/n_{sq,0}$ versus $\mathcal{T}_{st}$ is plotted in Fig. 5 together with the linear approximation of Eq. (6.66–b). Linear regression on experimental data gives $A_{sq}^{(QHT)} = -0.16 \pm 0.05$ and $B_{sq}^{(QHT)} = 1.14 \pm 0.07$, values in good agreement with $A_{sq} = -0.12$, $B_{sq} = 1.14$. Each experimental point of Fig. 5 represents an average value obtained over multiple acquisitions. In the inset the different values of $\mathcal{T}_{QHT}$, corresponding to four acquisitions at $\mathcal{T}_{st} = 0.64$ are reported. The bar indicates the quantum limit error, calculated by using Eq. (6.68). As it can be seen, all the points are spread over a range comparable to the quantum limit.

Finally, an identical behavior is observed for $n_{th,\mathcal{T}}/n_{th,0}$ (not plotted) resulting in $A_{th}^{(QHT)} = 0.07 \pm 0.05$, $B_{th}^{(QHT)} = 0.85 \pm 0.07$ ($A_{th} = 0.12$, $B_{th} = 0.89$).

A summary of the experimental findings is reported in Table (6-1).

The photon flux at the OPO output $F = N_{tot}/\tau$, with τ the cavity photon lifetime ($\tau \equiv \gamma_M^{-1}$), is less than 10^7 s^{-1}, for $N_{tot} \lesssim 0.7$ and $\tau \approx 6.6 \times 10^{-8}$, corresponding to an optical power $\lesssim 4.2$ pW. The method has been tested for different input states, by

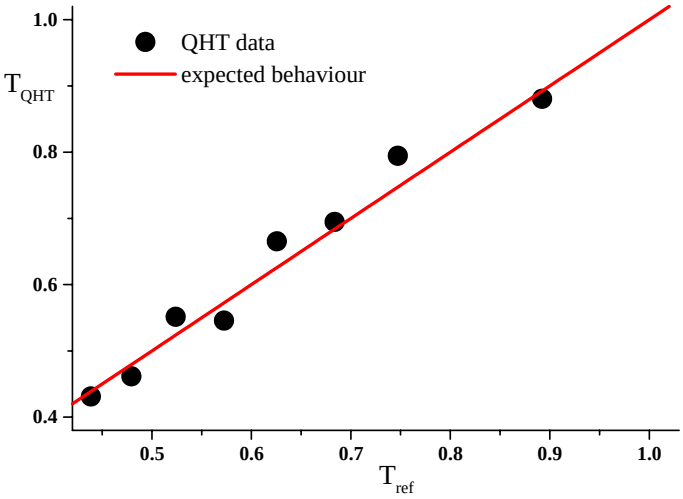

Figure 6.4. Tomographic reconstruction of the sample transmittivity $\mathcal{T}_{QHT}$ obtained by via mean photon number reconstruction against the reference values $\mathcal{T}_{ref}$ measured with standard intensity measurement. Experimental points are compared with the expected behaviour (straight line). Each point referes to more tomographic acquisition.

varying $\mathcal{E}$ and hence the photon flux by showing a good reliability down to a photon flux $F \sim 5 \times 10^6$ s^{-1} (i.e. ∼2.2 pW and $N_{tot,0} = 0.37$).

With $N = 10^6$ $\delta_{QHT}\left[\Delta X^2\right] \sim 1.3 \times 10^{-3}$ and $\delta_{QHT}\left[\Delta Y^2\right] \sim 0.8 \times 10^{-3}$ corresponding to $\delta\mathcal{T}/\mathcal{T} \sim 0.0024$ and ~ 0.056 for $\mathcal{T} = 1$. These QHT estimates were slightly less accurate than those one could obtain by concentrating $N/2$ data on X and $N/2$ on Y quadratures and computing their variances.

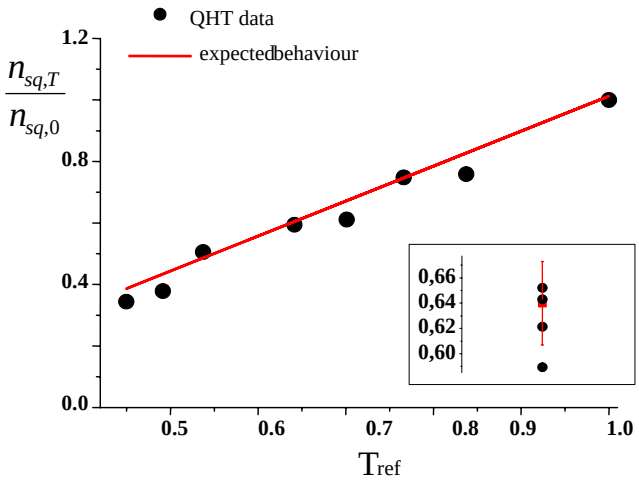

Figure 6.5. Tomographic reconstruction of the mean photon number normalized to the reference value ($n_{sq,T}/n_{sq,0}$) against the sample transmittivity. Experimental points are compared with the expected behaviour obtained by linearizing equation (6.68-b). The points in the inset are relative to four measurements for the fixed attenuator transmittivity $\mathcal{T}_{ref}$ =0.64. They are compared with the error bar obtained by using Eq. (6.71) for the reference state.

Chapter 7:
Squeezed radiation from non degenerate OPO

7.1 Seeded NOPA theory

The case of non degenerate parametric down conversion is considered. In the following the system will be assumed to work below threshold in frequency degeneracy condition with cross polarized signal and idler fields. The experimental realization of such a system is provided by the output of a frequency degenerate OPO based on a type II non linear crystal (NOPO). For simplicity the case of zero detuning and single ended cavity will be considered; results for double ended cavity are reported in [30] .

In analogy with the degenerate OPO, when the pump stationary amplitude α_p is below a threshold value, the system acts as non degenerate parametric amplifier (NOPA) with appreciable gain only over a limited bandwidth. Interesting application of the NOPA are relative to the case of two coherent beams (*seed* s) injected inside the cavity as inputs for the signal and idler modes (*seeded NOPA*). Non linearized Langevin equation for the involved intracavity modes are:

$$\begin{aligned} \frac{da_\xi}{dt} &= -\gamma a_\xi + \chi^{(2)} a_p a_{\xi'}^\dagger + \sqrt{2\gamma} A_\xi(t) \qquad \left(\xi, \xi' = s, i\right) \\ \frac{da_p}{dt} &= -\gamma_p a_p - \chi^{(2)} a_s a_i + A_p + \sqrt{2\gamma_p} a_p^{in}(t) \end{aligned} \tag{7.76}$$

where the input signal/idler fields entering through the mirror (γ) are:

$$A_\xi(t) = A' + a_\xi^{in}(t) \qquad \xi = s, i$$

A' representing the non-zero mean amplitude of the seed and $a_\xi^{in}(t)$ the vacuum fluctuations contribution. Equations (7.76) can be linearized around the steady state value. Letting $\mathfrak{r} = \alpha_s = \alpha_i$, steady state solutions for the signal/idler and pump modes are

expressed as a function of $A = A'\sqrt{2\gamma}$ by equations:

$$\begin{aligned} \alpha_p &= \frac{\gamma}{\chi^{(2)}} - \frac{A}{\chi^{(2)}\mathfrak{r}} \\ 0 &= \mathfrak{r}^3 - \frac{\chi^{(2)}A_p - \gamma\gamma_p}{\left(\chi^{(2)}\right)^2}\mathfrak{r} - \frac{\gamma_p A}{\left(\chi^{(2)}\right)^2} \end{aligned} \tag{7.77}$$

For $A = 0$ (no seed) equations for the signal and idler amplitude reduces to those for a traditional NOPO (unseeded) and the corresponding threshold is $\gamma\gamma_p/\chi^{(2)}$ (see previous chapters) [17]. In case of non zero subharmonic input ($A \neq 0$) Eq. (7.77) is a cubic equation whose solution describes the classical behaviour of the system: steady state solution undergoes a pitchfork bifurcation when the pump reaches the threshold. The addiction of the non zero coherent input ($A \neq 0$) destroys the symmetry of the standard parametric oscillator. The threshold itself is turned into [69] :

$$A_{th}^{seed} = \frac{\gamma\gamma_p}{\chi^{(2)}} + 3\left(\frac{A^2\gamma_p}{4\chi^{(2)}}\right)^{1/3} \tag{7.78}$$

For low pumping Eq. (7.77) has only one real root of the same sign as A. It is possible to show that this solution remains stable even above threshold. For $A_p \geq A_{th}^{seed}$, two other solutions of signs opposite to A's appear, only one of them being stable [69] . When the pump and the seed are not in phase, the equations of motion can be solved numerically. In this case the amplitude r for the field below threshold shows an oscillatory behaviour with the relative phase ζ. Maxima occur when $\zeta = 2n\pi$ ($n = 0, 1, 2..$), corresponding to perfect phase matching for the down conversion process. Conversely minima occur for $\zeta = (2n+1)\,\pi$ ($n = 0, 1, 2..$), corresponding to a breaking of the phase matching condition [68] .

[17] For zero input seed ($A = 0$) the equation for the pump steady state value is no longer described by equation (7.77-a) but coincides with the one reported in the previous chapter. The statedy state value for the pump below threshold is $\alpha_p = A_p/\gamma_p$

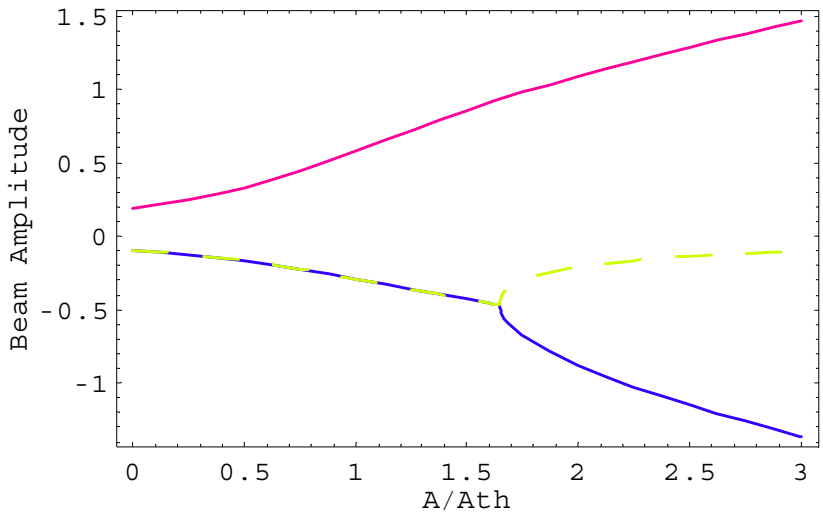

Figure 7.1. Steady state solutions of the intracavity amplitude for the seeded NOPO (seed amplitude $A/\gamma = 0.2$) as functions of the pump coherent amplitude, normalized to the threshold for the unseeded NOPO (A_p/A_{th}), with $\gamma_p\gamma/\left(\chi^{(2)}\right)^2 = 1$. For $A_p/A_{th}^{seed} \leq 1$, only one stable solution, with the same sign as the seed exists (red).This solution remains stable even above threshold ($A_p/A_{th}^{seed} > 1$) where the system admits two other solutions of sign opposite to A's, one stable(blu) and the other unstable(yellow, dashing).

7.1.1 Fluctuations for the NOPA output field

The field outing the NOPA will be described by the sum of the steady state and fluctuation contribution $\alpha_\xi + \delta a_\xi$. In the following it will be considered the system below threshold, with the zero dephase between seed and pump ($\zeta = 0$). In this condition, the system is said to work in *amplification* condition. Linearized equations for the field fluctuations δa are:

$$\begin{aligned}
\frac{d\delta a_\xi}{dt} &= -\gamma\ \delta a_\xi + \chi^{(2)}\alpha_p\ \delta a^\dagger_{\xi'} + r\ \delta a_p + \sqrt{2\gamma}a^{in}_\xi(t) \\
\frac{d\delta a_p}{dt} &= -\gamma_p\ \delta a_p - \chi^{(2)}[\delta a_s + \delta a_i] + \sqrt{2\gamma_p}a^{in}_p(t)
\end{aligned}$$

Coupled equations for signal and idler modes diagonalize by introducing the fields $d_\pm = \frac{1}{\sqrt{2}}(a_s \pm a_i)$ and their quadrature $X_\pm$ and $Y_\pm$. For the case $A = 0$, the evolution of $\delta X_\pm$ and $\delta Y_\pm$ is ruled by equations:

$$\begin{aligned}
\frac{d\delta X_\pm}{dt} &= -\left(\gamma \mp \chi^{(2)}\alpha_p\right)\delta X_\pm + \sqrt{2\gamma}X^{in}_\pm \\
\frac{d\delta Y_\pm}{dt} &= -\left(\gamma \pm \chi^{(2)}\alpha_p\right)\delta Y_\pm + \sqrt{2\gamma}Y^{in}_\pm
\end{aligned} \tag{7.79}$$

The spectra of squeezing for $\delta X_\pm$ and $\delta Y_\pm$ for the field $d_\pm$ outside the cavity can be calculated to be [30] :

$$\begin{aligned}
\left\langle \Delta\delta X^{out}_+(\omega)\right\rangle^2 &= S_+(\omega) = \left\langle \Delta\delta Y^{out}_-(\omega)\right\rangle^2 \\
\left\langle \Delta\delta Y^{out}_+(\omega)\right\rangle^2 &= S_-(\omega) = \left\langle \Delta\delta X^{out}_-(\omega)\right\rangle^2
\end{aligned}$$

with:

$$S_\pm(\omega) = \frac{1}{4}\left(1 \pm 4\frac{\mathcal{E}\gamma}{(\gamma \mp \mathcal{E})^2 + \omega^2}\right) \tag{7.80}$$

having put $\mathcal{E} = \chi^{(2)}\alpha_p$. Equations (7.80) show that d_+ exhibits antisqueezing and squeezing on the amplitude and phase quadratures respectively. Conversely d_- is squeezed

on the amplitude quadrature and anti-squeezed on the phase quadrature. By making use of Eqs. (7.79), it is also possible to retrieve the spectral behaviour for the signal and idler modes; the fluctuations of the two *single* output fields are phase insensitive and satisfy the relation:

$$\left\langle \Delta\delta X_s^{out}(\omega)\right\rangle^2 = \left\langle \Delta\delta Y_s^{out}(\omega)\right\rangle^2 = \left\langle \Delta\delta X_i^{out}(\omega)\right\rangle^2 = \left\langle \Delta\delta Y_i^{out}(\omega)\right\rangle^2 = G(\omega) \tag{7.81}$$

with:

$$G(\omega) = \frac{1}{4}\frac{\left(\gamma^2+\mathcal{E}^2+\omega^2\right)^2+4\gamma^2\mathcal{E}^2}{\left(\gamma^2-\mathcal{E}^2-\omega^2\right)^2+4\gamma^2\omega^2}$$

It is worth noting that $G(0) \rightarrow \infty$ as approaching the threshold ($\mathcal{E} \rightarrow \gamma$); therefore the system amplifies the vacuum noise of the input $a_\xi^{in}(\omega)$ and generates two outputs $a_\xi^{out}(\omega)$ with large noises. Equation (7.81) states that each single NOPA output does not show any squeezing; to see non classical effect, both beams are needed and the sum or difference $d_\pm$ fields must be measured. The quantum state describing the system is a two-modes squeezed state.

In case of non zero seed amplitude ($A \neq 0$), equations for the d_+ field quadrature slightly modify into:

$$\begin{aligned}
\frac{d\delta X_+}{dt} &= -\left(\gamma-\chi^{(2)}\alpha_p\right)\delta X_+ + r\,\delta X_p + \sqrt{2\gamma}X_+^{in} \\
\frac{d\delta Y_+}{dt} &= -\left(\gamma+\chi^{(2)}\alpha_p\right)\delta Y_+ + r\,\delta Y_p + \sqrt{2\gamma}Y_+^{in}
\end{aligned}$$

The corresponding variances for the output field are [68] :

$$\begin{aligned}
\left\langle \Delta\left(\delta X_+^{out}\right)(\omega)\right\rangle^2 &= \frac{1}{4}\left(\frac{4\gamma\left(\chi^{(2)}r\right)^2}{\left(\gamma-\chi^{(2)}\alpha_p\right)^2+\omega^2}+\frac{\left(\gamma+\chi^{(2)}\alpha_p\right)^2+\omega^2}{\left(\gamma-\chi^{(2)}\alpha_p\right)^2+\omega^2}\right) \\
\left\langle \Delta\left(\delta Y_+^{out}\right)(\omega)\right\rangle^2 &= \frac{1}{4}\left(\frac{4\gamma\left(\chi^{(2)}r\right)^2}{\left(\gamma+\chi^{(2)}\alpha_p\right)^2+\omega^2}+\frac{\left(\gamma-\chi^{(2)}\alpha_p\right)^2+\omega^2}{\left(\gamma+\chi^{(2)}\alpha_p\right)^2+\omega^2}\right)
\end{aligned} \tag{7.82}$$

The terms proportional to r in Eqs. (7.82) represent the contributions deriving from the correlation for δX_p, instead the other term arises from the correlation of X_+^{in} for the field outside the cavity.

For $A = 0$, below threshold $r = 0$ and (7.82) reduce respectively to (7.80). For $A \neq 0$ the first term can not be neglected and the field d_+ is squeezed when the output variance $\left\langle \Delta \left(\delta Y_+^{out} \right) (\omega) \right\rangle^2$ is less then $1/4$.

For the mode d_-, there is not dependence on field stationary amplitudes and treatment retraces that of $A = 0$. Since fluctuation properties for $d_\pm$ are similar, with the only macroscopic difference is that d_- has zero mean intensity i.e. it is a squeezed vacuum. Therefore the system below threshold generates bright and vacuum squeezing on two different polarizations.

For phase between the pump and the seeds equal to $\zeta = \pi/2$ the system is said to work in *deamplification condition*. The fluctuations analysis show that the behaviour for d_- and d_+ is inverted with respect to the case $\zeta = 0$.

7.1.2 NOPA and EPR paradox

From the physical point of view, since the signal and idler field originate from pump photons splitting in the amplification process, the fluctuations of their optical amplitudes are strongly correlated so that, under a limiting condition, they become quantum copies of each other. Since the signal and idler beams are spatially separable this correlation is non local. Due to its experimental application (see [30]), it is worth considering, as an example, the case of the unseeded NOPA working at deamplification. For the field amplitude, it is possible to show [30] that, at threshold:

$$\left.\begin{array}{c} X_s(0) = X_i(0) \\ Y_s(0) = -Y_i(0) \end{array}\right\} \tag{7.83}$$

Since Eq. (7.83) is an operator equation, the quadrature phase amplitudes of the output beams become quantum copies of one other. Equation (7.83-a) states that without disturbing the signal beam, the result for $X_s(0)$ can be inferred by a measurement of $X_i(0)$ with certainty. Alternatively from (7.83-b) $Y_s(0)$ can be inferred by a measure-

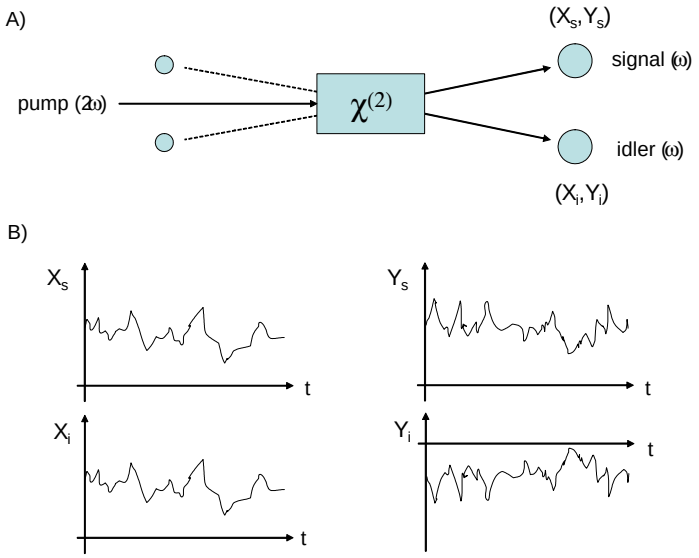

Figure 7.2. A) Non degenerate parametric down conversion via $\chi^{(2)}$. For the unseeded NOPA the noise for the input signal/idler vacuum field are amplified. B) Schematic representation of the fluctuating field amplitudes in the unseeded NOPA output in deamplification condition. Due to the correlation between signal and idler, their quadratures become quantum copies of each other ($X_s = X_i$, $Y_s = -Y_i$).

ment of $-Y_i(0)$. In other words, depending on which idler quadrature is measured, the corresponding signal quadrature is derived with probability 1, so that the signal beam can be thought as having in principle simultaneously a definite value of both amplitude and phase quadrature. As long as $[X, Y] \neq 0$ this contradicts the Heisenberg uncertainty principle [29] .

By considering amplitude and phase quadratures as the analogous of particle position and momentum, the correlation between the NOPA outputs is equal to that in the original Einstein Podolsky Rosen paradox where, depending on the observable measured on a particle 1, the state of a correlated particle 2 can be eigenstate of different operators [28] . This analogy is experimentally demonstrated in reference [30] where from measurement of the spatially separated idler beam, the two quadrature-phase amplitudes of the signal are inferred. The product of the inferred quadratures is then measured and observed to be below the limit associated with the Heisenberg uncertainty relation, in apparent contradiction with quantum mechanics as predicted by the argument of EPR.

7.2 Covariance matrix measurement

Bipartite (entangled) states of two modes of the radiation field, as the output of NOPA, have been widely used as basic tools for experimental realizations of continuous variables quantum information processing (see teleportation or dense coding [32, 33, 34]). It goes without saying that, in order to provide reliability to the use of these states, it is fundamental to find a manner to measure the amount of initial correlation. Moreover, since entanglement is generally corrupted by interaction with the environment, entangled states available in experiments are usually mixed states and it is important to establish whether or not entanglement has survived to the environmental noise effect [41, 42, 43, 44] .

Besides mean values of the field operators, the most relevant quantity characterizing a bipartite state made of two entangled modes a and b, is its covariance matrix $\boldsymbol{\sigma}$ [18].The covariance matrix is a real symmetric positive matrix; in terms of the field

[18]The characteristic function of a quantum state ρ is defined as the expectation values $\chi(\lambda_1, \lambda_2) = \langle D(\lambda_1) \otimes D(\lambda_2) \rangle$ where $\lambda_j \in \mathbf{C}$, $j = 1, 2$ and $D(\lambda) = \exp\left\{\lambda a^\dagger - \lambda^* a\right\}$ is the displacement operator. The most general bipartite Gaussian state

quadrature X, Y, it is expressed as:

$$\boldsymbol{\sigma} = \begin{pmatrix} \Delta X_a^2 & \Delta X_a Y_a & \Delta X_a X_b & \Delta X_a Y_b \\ \Delta Y_a X_a & \Delta Y_a^2 & \Delta Y_a X_b & \Delta Y_a Y_b \\ \Delta X_b X_a & \Delta X_b Y_a & \Delta X_b^2 & \Delta X_b Y_b \\ \Delta Y_b X_a & \Delta Y_b Y_a & \Delta Y_b X_b & \Delta Y_b^2 \end{pmatrix},$$

where diagonal terms $\Delta X^2 = \langle X^2 \rangle - \langle X \rangle^2$ denote the variance of the observable X and $\Delta XY = \frac{1}{2}\langle [X,Y]_+ \rangle - \langle X \rangle \langle Y \rangle$, with $[X,Y]_+ = XY + YX$ the anticommutator, is the mutual correlations between observables X and Y. If the two states are not correlated the matrix $\boldsymbol{\sigma}$ reduces to the sole diagonal elements.

The matrix $\boldsymbol{\sigma}$ can be conveniently expressed as:

$$\boldsymbol{\sigma} = -\mathbf{M} + \mathbf{V}$$

where the mean $\mathbf{M}$ and the variance $\mathbf{V}$ matrices are respectively:

$$\mathbf{M} = \begin{pmatrix} \langle X_a \rangle^2 & \langle Y_a \rangle \langle X_a \rangle & \langle X_a \rangle \langle X_b \rangle & \langle X_a \rangle \langle Y_b \rangle \\ \langle Y_a \rangle \langle X_a \rangle & \langle Y_a \rangle^2 & \langle Y_a \rangle \langle X_b \rangle & \langle Y_a \rangle \langle Y_b \rangle \\ \langle X_b \rangle \langle X_a \rangle & \langle X_b \rangle \langle X_a \rangle & \langle X_b \rangle^2 & \langle X_b \rangle \langle Y_b \rangle \\ \langle Y_b \rangle \langle X_a \rangle & \langle Y_b \rangle \langle Y_a \rangle & \langle Y_b \rangle \langle X_b \rangle & \langle Y_b \rangle^2 \end{pmatrix}. \tag{7.84}$$

corresponds to a characteristic function of the form

$$\chi(\lambda) = \exp\left[-\frac{1}{2}\vec{\lambda}^T \sigma \vec{\lambda} - i\vec{\lambda}^T \mathbf{X}\right]$$

where $\vec{\lambda}=(\lambda_1, \lambda_2)^T$ and $(\cdots)^T$ denotes transposition. The vector $\mathbf{X} = (\langle X_a \rangle, \langle Y_a \rangle, \langle X_b \rangle, \langle X_b \rangle)^T$ contains the mean value of the Cartesian mode operators. The characteristic function fully specifies a quantum state, *i.e.* any expectation value may be obtained as a phase space integral. Since for a Gaussian state the first two moments specify the characteristic function, their knowledge fully characterizes a bipartite Gaussian state.

and

$$\mathbf{V} = \begin{pmatrix} \langle X_a^2 \rangle & \frac{1}{2}\langle [Y_a, X_a]_+ \rangle & \langle X_a X_b \rangle & \langle X_a Y_b \rangle \\ \frac{1}{2}\langle [Y_a, X_a]_+ \rangle & \langle Y_a^2 \rangle & \langle Y_a X_b \rangle & \langle Y_a Y_b \rangle \\ \langle X_b X_a \rangle & \langle X_b X_a \rangle & \langle X_b^2 \rangle & \frac{1}{2}\langle [X_b, Y_b]_+ \rangle \\ \langle Y_b X_a \rangle & \langle Y_b Y_a \rangle & \frac{1}{2}\langle [Y_b, X_b]_+ \rangle & \langle Y_b^2 \rangle \end{pmatrix}, \tag{7.85}$$

The matrix $\mathbf{M}$ only contains the first order moments and can be reconstructed by measuring the four quadratures X_k and Y_k, $k = a, b$. Since the modes are separable, the measurement of their quadrature can be done by means of a single detector, measuring alternatively a and b.

Traditional schemes to measure $\mathbf{V}$, and in particular its off diagonal elements, employ two homodyne detectors acting separately on the modes a and b. To simplify the measurement procedure, it is proposed a new scheme, based on repeated measurements of single-mode quadratures with a *single* homodyne detector [47] . The price to be paid is the measurement of four quadratures instead of the sole X and Y, and the introduction of further optical modes beside a and b.

The set of modes used is:

$$a, \quad b, \quad c = \frac{a+b}{\sqrt{2}}, \quad d = \frac{a-b}{\sqrt{2}}, \quad e = \frac{ia+b}{\sqrt{2}}, \quad f = \frac{ia-b}{\sqrt{2}}\,. \tag{7.86}$$

If a and b correspond to vertical and horizontal polarizations of the light (parallel respectively to versor $\vec{v}$ and $\vec{h}$), c and d are rotated polarization modes at $\pm\pi/4$, whereas e and f correspond to left- and right-handed circular polarizations. It is worth noting that, for the output of a NOPA ($a \equiv a_s$, $a \equiv a_i$), c and d coincide with $d_\pm$ introduced in the previous paragraph. In terms of the quadratures of modes (7.86):

$$\mathbf{V} = \frac{1}{2}\begin{pmatrix} 2\langle X_a^2 \rangle & \langle Z_a^2 \rangle - \langle T_a^2 \rangle & \langle X_c^2 \rangle - \langle X_d^2 \rangle & \langle Y_e^2 \rangle - \langle Y_f^2 \rangle \\ \langle Z_a^2 \rangle - \langle T_a^2 \rangle & 2\langle Y_a^2 \rangle & \langle X_f^2 \rangle - \langle X_e^2 \rangle & \langle Y_c^2 \rangle - \langle Y_d^2 \rangle \\ \langle X_c^2 \rangle - \langle X_d^2 \rangle & \langle X_f^2 \rangle - \langle X_e^2 \rangle & 2\langle X_b^2 \rangle & \langle Z_b^2 \rangle - \langle T_b^2 \rangle \\ \langle Y_e^2 \rangle - \langle Y_f^2 \rangle & \langle Y_c^2 \rangle - \langle Y_d^2 \rangle & \langle Z_b^2 \rangle - \langle T_b^2 \rangle & 2\langle Y_b^2 \rangle \end{pmatrix}.$$

where the quadrature Z and T are $Z = X_{\pi/4}$ and $T = X_{-\pi/4}$. Furthermore, since

$$\begin{aligned}
\mathbf{V}_{14} &= \mathbf{V}_{41} = \frac{1}{2}\left(\left\langle Y_e^2\right\rangle - \left\langle Y_f^2\right\rangle\right) = \left\langle Y_e^2\right\rangle - \frac{1}{2}\left(\left\langle X_a^2\right\rangle + \left\langle Y_b^2\right\rangle\right) \\
\mathbf{V}_{23} &= \mathbf{V}_{32} = \frac{1}{2}\left(\left\langle X_f^2\right\rangle - \left\langle X_e^2\right\rangle\right) = \frac{1}{2}\left(\left\langle X_b^2\right\rangle + \left\langle Y_a^2\right\rangle\right) - \left\langle X_e^2\right\rangle
\end{aligned}$$

the measurement of the quadratures pertaining to mode f is not essential. Overall, in the proposed scheme, the reconstruction of the covariance matrix requires the measurement of at least fourteen quadratures, *e.g.* the following ones (of course measuring also the f-quadratures, being additional independent measurements, would improve the accuracy of the reconstruction):

$$\begin{aligned}
X_k, Y_k \qquad \text{with } k &= a, b, c, d, e \\
Z_{k'}, T_{k'} \qquad \text{with } k' &= a, b
\end{aligned}$$

Notice that the number of parameters needed to characterize a bipartite Gaussian state is fourteen.

7.2.1 Experimental implementation

Since the mode f is not necessary to reconstruct the covariance matrix, its experimental realization will not be considered.

Frequency degenerate, bright continuous-wave beams generated by a seeded NOPA below threshold, are orthogonally polarized and excited in a continuous variable bipartite entangled state. This means that the experimental realization of modes a and b is provided by the output of the NOPA ($a \equiv a_s$ and $b \equiv a_i$). The mode k under scrutiny is selected by inserting suitable components on the optical path of fields a and b, before the detector. To obtain modes $a,\ b,\ c,\ d$, the two modes a and b, both pass through a rotator of polarization R_ϑ, namely a $\lambda/2$ waveplate, and a polarizing beam splitter (PBS). The action of the rotator R_ϑ on the basis $\{\vec{v}, \vec{h}\}$ is given by

$$R_\vartheta\ \vec{v} \;=\; \cos\vartheta\ \vec{v} - \sin\vartheta\ \vec{h}$$

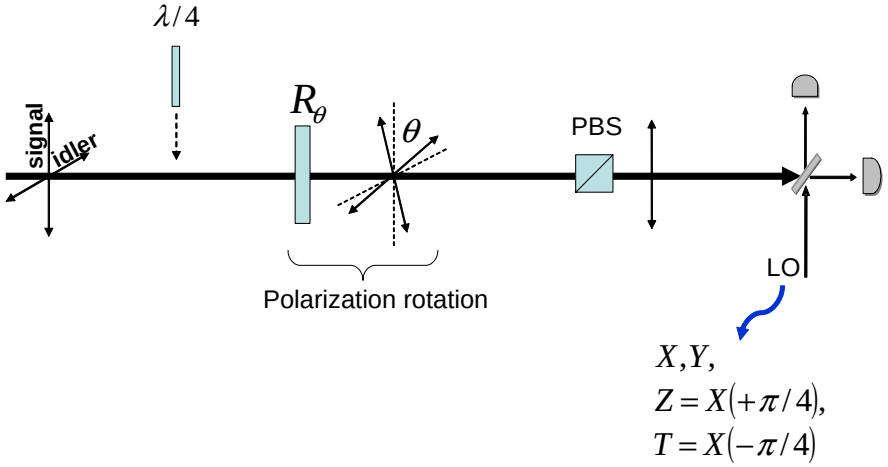

Figure 7.3. Experimental setup for the measurement of the covariance matrix. The cross polarized signal-idler beams from a seeded NOPA are sent to a single Homodyne detector measuring the quadratures X, Y, Z, T. The polarizing beam splitter (PBS) transmits to the detector the sole vertically polarized component of its input beam. To select for detection the modes a, b, c, d a polarization rotator R_ϑ (a $\lambda/2$ wave plate) is inserted on the beams path to the PBS. To realize the mode e an addictional $\lambda/4$-wave plate is needed.

$$R_\vartheta \ \vec{h} \ = \ \sin\vartheta \ \vec{v} + \cos\vartheta \ \vec{h}$$

The PBS is set to send to the homodyne detector only the projection of its input along the $\vec{v}$ direction. The combined action of these optical components for a given ϑ realize different modes k. In particular for $\vartheta = 0$, R_ϑ reduce to the identity and the sole mode a (vertically polarized), is sent to the detector. For $\vartheta = \pi/2$, the polarization of a and b is exchanged and the mode b is measured. In the intermediate case of $\vartheta = \pm\pi/4$, $1/\sqrt{2}$ of each mode is reflected thus realizing mode c and d.

In order to select mode e an additional $\lambda/4$ wave-plate should be inserted just before the rotator R_ϑ with $\vartheta = \pi/4$. The $\lambda/4$ wave-plate produces a $\pi/2$ shift between

Mode	$\lambda/4$	R_ϑ
a	no	0
b	no	$+\pi/2$
c	no	$+\pi/4$
d	no	$-\pi/4$
e	yes	$+\pi/4$

Table 7.2. Experimental setting of the rotator R_θ and the $\lambda/4$ waveplate to select the different modes k. The table refers to the elements of fig.1. The modes a and b are assumed to be respectively vertically and horizontally polarized

horizontal and vertical polarization components, thus turning the polarization from linear into circular.

Table (7.2) summarizes the settings needed to select the five modes. Overall, the vertically polarized mode k arriving at the detector can be expressed in terms of the initial modes as follows

$$k = \exp\{i\varphi\} \cos\vartheta \, a + \sin\vartheta \, b \, ,$$

where $\varphi = \pi/2$ when the $\lambda/4$ wave-plate is inserted, $\varphi = 0$ otherwise.

Once the mode k has been selected, a homodyne detector is used to measure the generic quadrature $X_{k,\theta}$. Indeed, to access $X_{k,\theta}$ the local oscillator phase θ has to be suitably tuned. As stated before, optimization of the detection efficiency is provided by matching the LO mode to the mode k. The mode matching requires precise control of the LO frequency, spatial and polarization properties. Remarkably, the detected mode is always vertically polarized, thus avoiding any need of tuning the LO polarization.

Chapter 8:
NOPA experimental realization

8.1 Phase matching condition

As stated in previous chapters the working condition of an OPO is conditioned by the perfect satisfaction of phase matching condition. In term of the pump (λ_p), signal (λ_s) and idler (λ_i) wavelengths the phase matching condition for a non degenerate OPO is explicitly written as:

$$\Delta k\left(\boldsymbol{\lambda}, T\right) \equiv 2\pi\left(\frac{n_p\left(\lambda_p, T\right)}{\lambda_p} - \frac{n_s\left(\lambda_s, T\right)}{\lambda_s} - \frac{n_i\left(\lambda_i, T\right)}{\lambda_i}\right) = 0 \tag{8.87}$$

with $\boldsymbol{\lambda} = (\lambda_p, \lambda_s, \lambda_i)$. The crystal refractive index $n\left(\lambda, T\right)$ as a function of the wavelength λ and the crystal temperature T is provided by the empirical *Sellmeier* relation [70] :

$$n_\alpha\left(\lambda, T\right) = \sqrt{A_\alpha + \frac{B_\alpha}{1 - C_\alpha/\lambda^2} - D_\alpha\lambda^2} + \left(F_\alpha\lambda + G_\alpha/\lambda^2 + H_\alpha/\lambda + I_\alpha\right)\left(T - T_0\right) \tag{8.88}$$

where $\alpha = x, y, z$ label the crystallographic axes directions and T_0=35°C is a reference temperature. The Sellmeier coefficients (A_α,B_α,C_α....) are determined experimentally for suitable ranges of temperature and wavelength..

Once λ_p is fixed, the non linear interaction is optimized for the pair signal-idler satisfying relation (8.87) and the energy conservation ($\omega_p = \omega_s + \omega_i$). When $\Delta k \neq 0$, there exists a characteristic length $l_c = \pi/\Delta k$ (*coherence length*) representing the distance over which, due to dispersion in the non linear medium, the relative phase between pump and signal/idler changes by π. After a coherence length, the efficiency of energy transfer from pump to subharmonic reduces and the energy flows back from the signal/idler to the pump. The energy transfer inverts again after a l_c, so that the

conversion efficiency shows an oscillatory behaviour. Conversely for $\Delta k \to 0$, $l_c \to +\infty$ and the subharmonic intensities grow with the square of the interaction length [2] .

In traditional devices, phase matching condition is satisfied by exploiting crystal birefringence; refraction indexes $n(\lambda, T)$ in (8.87) are adapted so to have $\Delta k = 0$ for a desired pair of λ_s and λ_i [19]. In *critical phase matching*, the pump incidence angle is varied with respect to the crystal axes. This technique is highly affected by Poynting vector walk off and crystal disalignments [2] . These problems are overcome in *non critical phase matching* [2] where the $n(\lambda, T)$ dependence on the crystal temperature is exploited. This is the technique discussed for the LNB in previous chapters. For each choice of $\boldsymbol{\lambda}$, by exploiting (8.88), Eq. (8.87) can be inverted so to obtain the crystal temperature producing the perfect phase matching for the desired process. Non critical phase matching imposes strict contraints to the experimental setup, regarding both the temperature range and the relative stability around the working point. Moreover, it is worth stressing that there are situations in which the simple mathematical inversion of formula (8.87) for a given $\boldsymbol{\lambda}$ leads to non physical working temperature. In these cases birefringent phase matching can not be used and alternative ways are needed.

8.1.1 Quasi-Phase Matching

*Quasi-phase matching (*QPM*)* overcomes some of the limitations of traditional phase matching methods.

In QPM, the phase mismatch Δk, accumulated by the interacting beams, is compensated along the interacting length by a suitable phase delay introduced by the crystal itself [50] . Although the efficiency is not as good as for the perfect phase matching, this technique has the advantage that can be applied practically to every choice of Δk, the only restrictions on $\boldsymbol{\lambda}$ being determined by the material transparency range.

More specifically, given a certain non linear process characterized by $\bar{\boldsymbol{\lambda}}$ and fixed the desired working temperature $\bar{T}$, the corresponding coherence length is computed as $l_c = \pi/\Delta k\left(\bar{\boldsymbol{\lambda}}, \bar{T}\right)$ and the crystal non linear coefficient d ($\sim 2\chi^{(2)}$ for used crystal) is

[19] It is obvious that the wavelenghts λ_s and λ_i must be chosen within the set of those satisfying the energy conservation relation for a fixed λ_p.

modulated as a square function with period Λ multiple of $2l_c$:

$$d \rightarrow d(z) = d \cdot \sum_{m=-\infty}^{+\infty} \frac{2}{m\pi} \sin\left(\frac{m\pi}{2}\right) e^{i\frac{2\pi m}{\Lambda}z} \tag{8.89}$$

The crystal can be thought of as a wafer made up of different slices, with the sign of the non linear coefficient in each slab reversed with respect to the adjacent ones. These crystals are called *poled* ; they present the greatest advantage of providing non critical phase matching for a non linear process at a temperature chosen by the customer. From the physical point of view, the fields is dephased by π (due to crystal dispersion) at each coherence length; the crystal periodicity introduces an extra dephase π (expressed by the sign change of d) that cancels out the destructive interference effect.

The effective phase matching condition for a poled crystal is given by [50] :

$$\Delta k_m = \Delta k\left(\bar{\boldsymbol{\lambda}}, \bar{T}\right) - \frac{2\pi m}{\Lambda} = 0 \tag{8.90}$$

The index m, the *order* of QPM, refers to the term in (8.89) giving the major contribution in the integration of subharmonic fields equations. For a poling of order m the non linear period $\Lambda = 2ml_c$; for $m = 1$, the sign of the non linear coefficient is inverted each l_c and the conversion efficiency is the best achievable.

8.2 NOPA realization with PKTP

In order to provide cross polarizations for the signal and idler beams, the crystal used for the NOPA must be a type-II one. However, properties of commercial type-II crystals do not allow working in frequency degeneracy condition at $\lambda_{s/i} = 1064$nm. This limit was overcome in previous implementations of NOPA, either a custom crystal [49] or a custom source [**?**] .

In the proposed setup, the problem is bypassed by combining a commercial doubled Nd:YAG laser with a periodically poled α-cut KTP crystal (PKTP). In this way the generated signal/idler beams exhibit frequency degeneration, still preserving cross

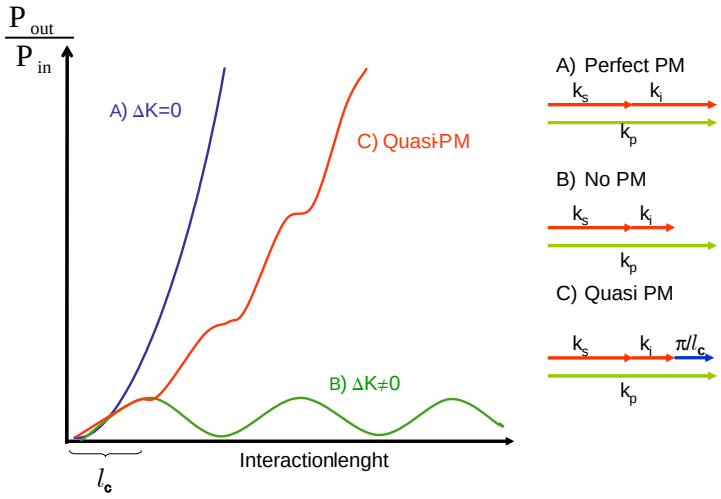

Figure 8.1. Comparison of the conversion efficiency against the interaction lenght for the perfect phase matching (blu), non phase matching (green) and quasi phase matching (red). In perfect phase matching the wavevectors for the signal and idler beams perfecly compensated the pump one, corresponding to perfect momentum conservation for the system of signal, idler and pump photons. In this case the efficiency is proportional to the squared interaction lenght. For non perfect phase matching the momentum conservation is not satisfied so that the conversion efficiency shows an oscillatory behaviour determinated by the coherence lenght l_c. For quasi phase matching the missing momentum is provided by the crystal periodic structure. The conversion efficiency increases with the interaction lenght more slowly than for the perfect phase matching.

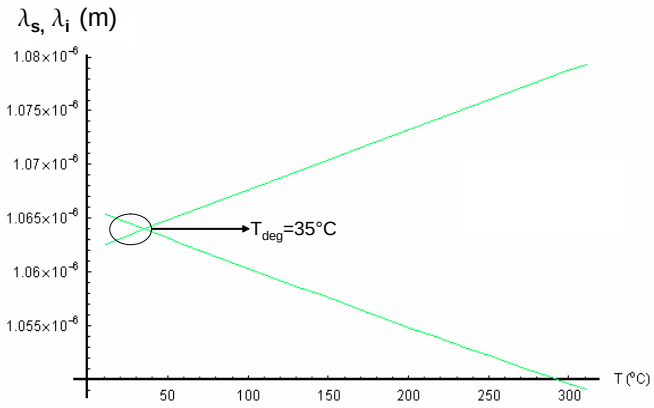

Figure 8.2. Computed behaviour of the emitted signal/idler wavelenghts as functions of the crystal temperature for the used PKTP. The two lines have the same slope (absolute value) and cross at $T_{\rm deg}$ =35$^{\circ}C$.

polarization characteristic because of type-II phase matching. This solution is economically much more stable and easy to obtain with respect to previous ones.

The PKTP is designed by solving Eq. (8.90) for $\lambda_i = \lambda_s = 2\lambda_p$ =1064nm as a function of the working temperature $\bar{T}$ with KTP Sellmeier coefficient given in reference [70] . The corresponding poling period, for $\bar{T}$ =35$^{\circ}C$ ($\sim$room temperature) is Λ =448.4μm. Once λ_p and Λ are fixed, the behaviour $\lambda_{s/i}\,(T)$ of the emitted signal/idler wavelengths against the crystal temperature can be computed by inserting expression (8.88) in (8.90) and exploiting energy conservation relation. The shape of $\lambda_{s/i}\,(T)$ strongly depends on the crystal characteristics via the (8.88). For the used crystal the computed $\lambda_{s/i}\,(T)$ are straight lines intersecting themselves at $T = 35^{\circ}$C with slope $\pm$0.0558 nm/$^{\circ}$C [71] .

The experimental setup required for the NOPA realization is the same used for the DOPO, except for the temperature control system. The cavity mirror have been chosen with trasmittivity T_{in} (@1064nm)= 0. 75$^{0}/_{00}$ (T_{in} (@532nm)= 0.163%) for the input mirror and T_{out} (@1064nm)= 3.4% (T_{in} (@532nm)= 1%) for the output one. Absorption losses in the crystal are 0.8% for the IR and 4.5% for the green. The cavity length

is $\lesssim 100$ mm, thus ensuring a good cavity stability and a longer confocal parameter, so to simplify the homodyne alignment procedure. The measured threshold for the crystal is 40 mW.

The NOPA seeds for the covariance matrix measurement is provided by an extra half wave plate that rotates the polarization of the IR seed at 45° with respect to the polarizations of the KTP output. Due to the PZT on the IR seeds beam steering the dephase between seeds and pump can be driven so to achieve the NOPA in amplification or deamplification. Beside the parametric gain measurement, this permits to look at specific quadratures of d_+ and, varying the seeds phase ζ, to move the squeezing from X_+ (amplification condition) to Y_+ (deamplification condition).

In view of low working temperature sophisticate temperature controls are replaced by a Peltier element with short response time. Moreover, due to the slow thermal response of the KTP, the required stability is of the order of $10m^\circ C$, essentially imposed by the triple resonance condition. The controller sensor is an NTC resistor inserted in a Winston bridge. The achieved stability is of $\approx 1m^\circ C$ well the below the required one.

The homodyne set up is the same as for the DOPO.

8.2.1 Degeneration temperature measurement

To characterize the performances of the PKTP, beside standard absorption measurements, particular attention is paid to the estimation of the actual degeneration temperature $T_{\rm deg}$ for the emitted signal/idler beams. To this aim, the unseeded NOPA is driven above threshold and the generated beams are sent to a grating. An halfwave plate followed by a polarizing beams splitter permit to select the sole signal/idler beam or equal fractions of both. For $T \neq T_{\rm deg}$ bright signal and idler beams are generated at the wavelengths satisfying the energy conservation and the phase matching condition for that temperature. The greater is the distance of T from $T_{\rm deg}$, the greater the distance between λ_s and λ_i. When $T \approx T_{\rm deg}$, the signal and idler beams have the same wavelengths and they are no longer resolved.

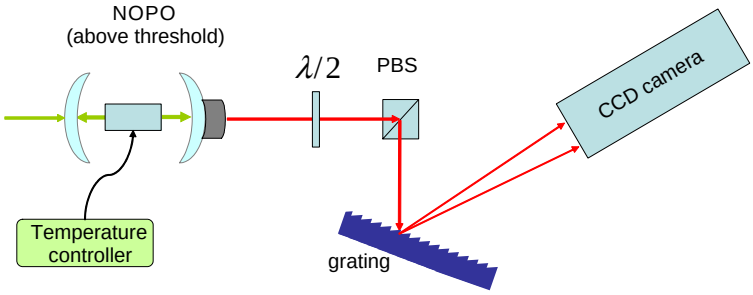

Figure 8.3. Experimental set-up for the measurement of the degeneration temperature $T_{\rm deg}$ by means of the diffraction grating. The above threshold NOPO generates bright signal and idler beams. Its working point is changed by acting on the crystal temperature. The beams outing the NOPO are sent to a system $\lambda/2$+PBS that selects for reflection on the grating a signle beam or both ones. The beams reflected by the grating are sent to a CCD camera that records their positions. For $T \neq T_{\rm deg}$ the signal and idler separate in two spots.

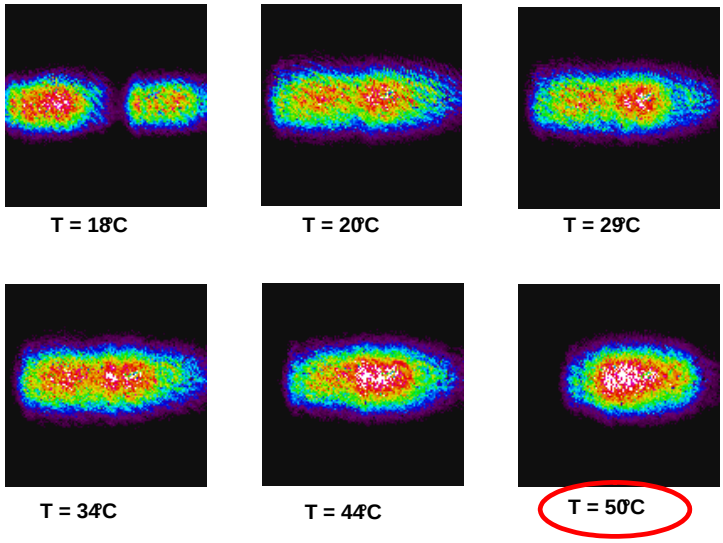

Figure 8.4. Signal and idler spots recorded by the CCD camera as functions of the crystal temperature. At low temperature ($18^{\circ}C$), the spots appear well separated, indicating that the beams have different wavelenghts. When the temperature is increased the spots become closer and for $T \approx 50^{\circ}C$ they are no longer distinguishable.

The grating used in the experiment is a blazed one (DG; Jobin-Yvon 1200 mm^{-1}, optimized @1064 nm). It is set to provide an optimal resolution of $\sim$ 1nm (computed @1880nm) with a spatial dispersion of 1.4mrad/nm. The beams reflected by the grating are sent to the CCD camera and their positions recorded; the behaviour of the spot position on the CCD is a replica of the wavelength's one.

A preliminary rough estimation of $T_{\rm deg}$ is obtained by sending both signal and idler to the camera. The crystal temperature is scanned 25°C÷70°C . For temperature around 25°C the signal and idler spots appear spatially separated, they become closer when the temperature is increase and at T ≈50°C they are no longer resolved. If the temperature is still increased they separate again, thus suggesting an actual $T_{\rm deg}$ ≈50°C (see fig. (8.4)).

A more detailed check is done by sending to the camera only one beam (signal *or* idler) and changing the crystal temperature. The spot position of each beam is recorded with respect to the camera center and plotted as function of T. Experimental data for both signal and idler show a linear behaviour [20]; by performing linear regression the slopes of the two curves are found to be equal (within the error bars) except for the sign. The cross point gives for the degeneration temperature $T_{\rm deg}$ ≈54°C. The observed symmetrical behaviour is an expression of the energy conservation relation linking $\lambda_{s/i}$ and λ_p in agreement with theory. By using the grating properties to retrieve the experimental behaviour of emitted wavelengths from the spot curves, the slopes of the straight lines $\lambda_{s/i}\,(T)$ are found to be of the same order of magnitude of the theoretical one (±0.03nm/°C). Not perfect consistency with the theoretical value can be due to the uncertainty in determining the exact distance between the grating and the CCD plane.

The difference between the experimental (54°C) and the theoretical (35°C) values of $T_{\rm deg}$ can be due to both impurities in the crystal or error in the poling period.

In real crystals an excess of impurities can induce deviations of Sellmeier coefficients from the values used in designing the poled crystal. The effect of small variations of Sellmeier coefficient on $T_{\rm deg}$ can be evaluated by substituting expression (8.88) in

[20] When variyng the crystal temperature the spot counter propagate in the horiizontal direction, with constant vertical position.

(8.87) and solving for T the Eq. (8.90) with $\lambda_s = \lambda_i$. It is seen that a variation of 3.5% in the indexes of refraction is sufficient to explain the observed change in T_{deg}. The corresponding behaviour of $\lambda_{s/i}(T)$ is only slightly changed with respect to the reference one. This situation is analogous to that reported in reference [60] , where the observed degeneration temperature for the LNB was different from the expected one; by assuming small changes in the A_α coefficient the authors were able to reproduce both the observed T_{deg} and the tuning curve for a singly resonant OPO. In that case the variation of the Sellmeier equation was attributed to the crystal doping.

A second possible reason of changes in T_{deg} can be due to manufacture error in the poling period. Even in this case, T_{deg} can be computed as a function of Λ; the observed T_{deg} corresponds to a poling period of $\Lambda = 432\mu$m with a variation of $\approx$3.6% with respect to the nominal value [71] .

A precise analysis of both the crystal impurities degree and the poling period is beyond the instrumentation present in the laboratory. However the previous estimations allow concluding that the observed T_{deg} could probably be attributed to a co-action of both explained effects.

8.2.2 Triply Resonance Condition and crystal misalignment

As for the DOPO the triply resonance of pump and signal/idler is required for a low threshold of the NOPO. Since the Drever Pound locks the cavity lengths on the pump resonance, the triply resonance condition is obtained by fine temperature tuning.

With respect to the LNB, the PKTP crystal suffers of great sensibility to small misalignments. For perfect triple resonance, the beams outing the cavity are all in phase and the peaks of the pump signal and idler resonances coincide. If the crystal is slightly misaligned, the optical path of each beam will depend on the angle θ between the crystal optical axis and the cavity one (assumed to coincide with the beams propagation direction). With respect to $\theta = 0$ (perfect crystal alignment), the beams acquire at the crystal

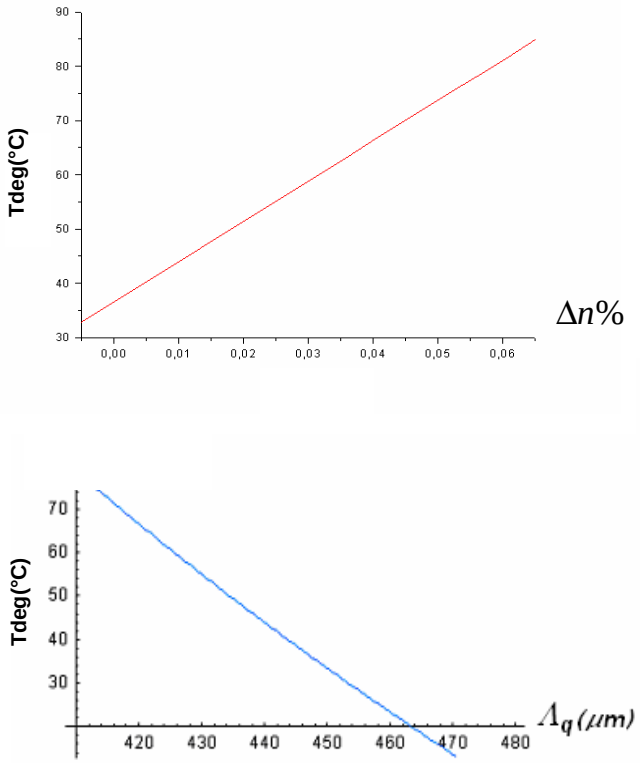

Figure 8.5. Computed behaviours of the degeneration crystal for the used PKTP crystal as functions of the refractive indexes (up) and the poling period (down) variations. In both cases, parameter variations of the order of few percents are enough to explain the deviations of the observed degeneration temperature from the nominal one.

output an extra phase:

$$\varphi_\xi = \frac{2\pi L}{\lambda_\xi} n\left(\lambda_\xi, T\right)\left(1 - \frac{1}{\cos\theta}\right)$$

with L the crystal length. In the limit of small θ, φ_ξ can be expressed in terms of the angle $\bar{\theta}_\xi$ corresponding to $\varphi_\xi = \pi$:

$$\varphi_\xi = \pi \frac{\theta^2}{\bar{\theta}_\xi^2} \tag{8.91}$$

At the degeneration temperature, taking into account the different index of refraction for the beams [21], for the PKTP at $\lambda_s = \lambda_s = 2\lambda_p$ =1064nm:

$$\begin{aligned} \bar{\theta}_p &= 6.17 \text{ mrad} \\ \bar{\theta}_s &= 8.62 \text{ mrad} \\ \bar{\theta}_i &= 8.82 \text{ mrad} \end{aligned} \tag{8.92}$$

The difference in $\bar{\theta}_s$ and $\bar{\theta}_i$ are due to the different index of refraction for the two cross polarizations. If the system temperature is set to guarantee the superposition of the signal, idler and pump resonances for $\theta = 0$, a phase $\varphi_\xi = \pi$ ($\theta_\xi = \bar{\theta}_\xi$) on one of the beams will not spoil the triply resonance. This in general true also for $\theta_\xi \neq \bar{\theta}_\xi$, provided the relative dephase $\Phi_{\xi,\xi'} = \varphi_\xi - \varphi_{\xi'}$ acquired by the beams, are within the cavity linewidths (expressed in radiant):

$$\Delta\left(rad\right)_\xi = \frac{\pi}{\mathcal{F}_\xi} \tag{8.93}$$

[21] The Sellmeier coefficient used in the present calculation are the nominal one used in the PKTP project. This choice is justified by the fact that the modification of $\bar{\theta}_\xi$ corresponding to the A_α variations imposed to give reason of the experimental $T_{\rm deg}$ are negligible.

In (8.93), $\mathcal{F}_\xi$ is the cavity finesse at λ_ξ and π corresponds to a FSR. For the used cavity at degeneration:

$$\begin{aligned} \Delta\left(rad\right)_p &= 52 \text{ mrad} \\ \Delta\left(rad\right)_{s/i} &= 18 \text{ mrad} \end{aligned}$$

It is simple to show (cfr (8.92) and (8.91) for expression of $\Phi_{\xi,\xi'}$) that for $\theta \gtrsim 1.2 mrad$, $\Phi_{s/i,\,p} > \Delta\left(rad\right)_p$ so that the signal/idler beam is shifted outside the pump resonance and the NOPO is driven out of triply resonance condition. For the same angle the IR resonances can still be considered as for $\theta_s = \theta_i = 0$ ($\Phi_{s,i} \ll \Delta\left(rad\right)_{s/i}$). The walk-off effect corresponding to crystal disalignment of the present order of magnitude is completely negligible compared with the beam spot size.

The extreme sensitivity of the system to crystal misalignment, introduces a great hindrance to the triply resonance fulfillment; small changes in crystal orientation can seriously compromise the reliability of the entire NOPO setting procedure. In order to overcome this problem, the combined action of temperature and crystal orientation tuning will be exploited. Work along this direction is still in progress. Once the triply resonance will be reached the measurement of the OPO output will be performed by means of a single homodyne detector, to reconstruct the state covariance matrix as explained in previous chapter.

Conclusions

The subject matter of this Thesis is the study of optical parametric oscillators (OPO) below threshold as sources of non classical radiation. In the first part of the Thesis a degenerate OPO (DOPO) has been examined with signal and idler beams having the same frequency and polarization. When the cavity extra losses are not negligible, the DOPO output beam is in a squeezed thermal vacuum state (STV) with noise reduction on the phase quadrature. The DOPO output properties are examined by means of an homodyne detector able to measure the state quadratures at different phases. The acquired data are analyzed by looking directly at the statistics or by means of the quantum homodyne tomography via pattern function, able to reconstruct the state properties without any hypothesis a priori on it. The experimental set up for the DOPO and homodyne implementation is accurately described, by stressing the strategies used to optimize them. Results relative to the detection of the DOPO output for different cavity losses and distances from threshold are reported. Operating the OPO away and close to the threshold, the measured density matrix elements deviate in a more or less pronounced way from those of a vacuum squeezed thermal Gaussian state. These deviations from the Gaussian state are confirmed by directly analyzing the distribution functions of the quadratures $X(\theta)$ for 100 values of θ. Plotting the Kurtosis (K_θ) of each distribution as a function of θ for different distances from the threshold it is found an oscillatory behaviour with K_θ maximum(minimum) for the anti–squeezed (squeezed) quadrature. In general the maximum $K_{\theta\,\max}$ decreases by moving away from the threshold. A theoretical model explaining the observed behaviour in terms of threshold fluctuations is reported. The DOPO output is computed for small fluctuations of parametric gain and cavity detuning respectively due to residual noise in the laser pump amplitude and in the cavity length control and the detection effect is considered. The kurtosis is calculated by means of an iterative procedure. First results of numerical simulations are reported, showing a good qualitative agreement with the experimental findings.

A scheme for measuring the optical transmittivity of a sample by using squeezed vacuum radiation is also illustrated. Main advantage of this method is a number of photons hitting the sample during the measurement some orders of magnitude smaller than that relative to standard techniques based on intensity measurements of coherent beams.

The core of the method consists in the measurement, via homodyne detection, of the variance ΔX_θ^2 of a generic quadrature of a squeezed vacuum field, generated by a below threshold OPO and passing through the sample under investigation. The accuracy of the method is compared with that based on absorption of coherent beams (with and without a squeezed vacuum component) as a function of sample transmittivity, number of data and detection bandwidth. In the case a low number of photons interacting with the sample during the measurement is required, the proposed method is the most accurate. An experimental test of the procedure is reported. X_θ is obtained by scanning the interval $\theta \in (0,\, 2\pi)$ so allowing a complete reconstruction of the state Wigner function. Since it is essential to the scheme, the assumption of Gaussian statistics for the squeezed vacuum field is checked. The experimental findings show that, for photon fluxes of the order of few pW (at 1064 nm), the accuracy is of the order of the quantum limit, that is the method does not suffer substantially from other technical noise sources.

In the second part of the thesis the case of non degenerate parametric oscillator (NOPO) below threshold is treated. The signal and idler from a seeded NOPO below threshold are spatially separable and form an EPR pair, the entanglement properties depending on the NOPO parameter. The correlation between them can be measured in terms of the covariance matrix. A simple scheme is suggested to reconstruct the covariance matrix of two-mode states of light using a single homodyne detector plus a polarizing beam splitter and a polarization rotator. The scheme requires the local measurements of 14 different quadratures pertaining to five field modes. It can be used to fully characterize bipartite Gaussian states and to extract relevant informations on generic states.

Eventually the problem of the experimental implementation of a NOPO based on commercial pump laser source and periodically poled KTP (PKTP) crystal is discussed. The PKTP is designed in order to generate cross polarized and frequency degenerate signal and idler, by using as pump beam the output @532nm of a duplicate Nd:Yag source. The results of the first tests together with the procedure for finding the frequency degeneration crystal temperature are reported.

References

[1] R.E. Slusher, L.W. Hollberg, B.Yurke, J.C.Mertz, J.F. Valley, "Observation of squeezed states generated by four wave mixing in an optical cavity", Phys. Rev. Lett. **55** 2409 (1985)

[2] A. Yariv,"Quantum Electronics", Wiley (III ed.) (1988);

[3] D. Walls and G. Milburn, "Quantum Optics", Springer-Verlag (1994);

[4] H. J. Kimble, M. Dagenais, and L. Mandel "Photon Antibunching in Resonance Fluorescence", Phys. Rev.Lett. **39**, 691695 (1977).

[5] Special Edition on "Squeezed States of the Electromagnetic Field" of J. Opt. Soc. Am B 4, n. 6, H. J. Kimbleand D. F. Walls eds. (1987).

[6] C. Fabre, Giacobino, Heidmann, Reynaud."Noise characteristics of a non-degenerate Optical Parametric Oscillator. Application to quantum noise reduction" J. Phys. France. **50** 1209 (1989)

[7] L. Wu, H. Kimble, J. Hall, and H. Wu. "Generation of squeezed states by parametric down conversion" Phys. Rev. Lett. **57** 2520 (1986).

[8] Jiangrui Gao, Fuyun Cui, Chenyang Xue, Changde Xie, and Peng Kunchi. "Generation and application of twin beams from an optical parametric oscillator including an α-cut KTP crystal" Opt. Lett., **23** 870 (1998).

[9] A. S. Lane, M. D. Reid and D. F. Walls "Quantum analysis of intensity fluctuations in the nondegenerate parametric oscillator" Phys. Rev. A **38**, 788 (1988);

[10] P. R. Tapster, S. F. Seward, and J. G. Rarity "Sub-shot-noise measurement of modulated absorption using parametric down-conversion" Phys. Rev. A **44**, 3266 (1991);

[11] A. Porzio, F. Sciarrino, A. Chiummo, M. Fiorentino and S. Solimeno; "Twin beams correlation and single beam noise for triply resonant KTP OPOs"; Optics Communications **194** 373 (2001);

[12] A. Porzio, C. Altucci, P.Aniello, C. De Lisio, S. Solimeno. "Resonances and Spectral Properties of Detuned OPO pumped by Fluctuating Sources" Appl. Phys. B, **4**, S313 (2002)

[13] A. Porzio, A. Chiummo, F. Sciarrino and S. Solimeno; "Twin-beams statistics for strong pumping"; Zeitschrift fur Naturforschung **56a**, 224 (2001);

[14] C. D. Nabors and R. M. Shelby, "Two-color squeezing and sub-shot-noise signal recovery in doubly resonant optical parametric oscillators" Phys. Rev. A **42**, 556 (1990);

[15] J.J. Snyder, E.Giacobino, C.Fabre, A.Heidmann and M.Ducloy "Sub shot noise measurements using the beat note between quantum-correlated photon beams", JOSA B **7** 2132 (1990);

[16] A. Porzio, C. Altucci, M. Autiero, A. Chiummo, C. de Lisio, and S. Solimeno, "Tunable twin beams generated by a type–I LNB OPO", Appl. Phys. B **73**, 763, (2001);

[17] U. Leonhard,"Measuring the Quantum State of Light", Cambridge Univ. Press (1997);

[18] Carlton M. Caves, "Quantum-mechanical noise in an interferometer", Phys. Rev. D **23**, 1693 (1981);

[19] P. Grangier, R. E. Slusher, B. Yurke, and A. LaPorta "Squeezed-light enhanced polarization interferometer" Phys. Rev. Lett. **59**, 2153 (1987);

[20] E. S. Polzik, J. Carri, and H. J. Kimble, "Spectroscopy with squeezed light ". Phys. Rev. Lett. **68**, 3020 (1992);

[21] M.J. Collett and C. W. Gardiner,"Squeezing of intracavity and travelling-wave light fields produced in parametric amplification" Phys. Rev. A, **30**, 1386 (1984);

[22] M. J. Collett and D. F. Walls, "Squeezing spectra for non linear optical systems" Phys. Rev. A, 32, 2887 (1985).

[23] M. J. Collett and R. Loudon,"Output properties of parametric amplifiers in cavities" J. Opt. Soc. Am. B, 4, 1525 (1987).

[24] P. Kinsler, P.D. Drummond, " Quantum dynamics of the parametric oscillator" Phys. Rev. A **43** 6194 (1991)

[25] S. Chaturvedi, K. Dechoum, P.D. Drummond, "Limits to squeezing in the degenerate optical parametric oscillator", Phys. Rev. A, **65**, 033805 (2002)

[26] V. D'Auria, A. Chiummo, M. De Laurentis, A. Porzio, S. Solimeno, and M. G.Paris, "Tomographic characterization of OPO sources close to threshold," Opt. Express **13**, 948 (2005)

[27] V. D'Auria, C. de Lisio, A. Porzio, S. Solimeno, Matteo G.A. Paris, "Transmittivity measurements by means of squeezed vacuum light", *submitted to Journ. Opt. B*

[28] A.Einstein, B.Podolsky, N.Rosen, "Can quantum mechanical description of physical reality be considered complete?" Phys. Rev. **47**, 777 (1935);

[29] P.D. Drummond, M.D. Reid, "Correlations in nondegenerate parametric oscillation. II. Below threshold results", Phys. Rev. A, **41**, 3930 (1990);

[30] Z.Y.Ou, S.F. Pereira, H.J.Kimble, "Realization of the Einstein-Podolsky-Rosen Paradox for Continuous Variables in Nondegenerate Parametric Amplification" Appl. Phys. B, **55**, 265 (1992);

[31] Z.Y.Ou, S.F. Pereira, H.J.Kimble, "Realization of the Einstein-Podolsky-Rosen Paradox for Continuous Variables" Phys. Rev.Lett., **68**, 3663 (1992)

[32] S. L. Braunstein, P. van Loock, quant-ph/0410100, Rev. Mod. Phys. **77**, (2005), in press;

[33] J. Eisert, D. E. Browne, S. Scheel, and M. B. Plenio, Ann. Phys. **311**, 431 (2004); J. Eisert, M.B. Plenio, Int. J. Quant. Inf. **1**, 479 (2003);

[34] A. Ferraro, S. Olivares, and M. G. A. Paris, *Gaussian States in Quantum Information* (Bibliopolis, Napoli, 2005).;

[35] T. C. Ralph and P. K. Lam, "Teleportation with bright squeezed light" Phys. Rev. Lett. **81**, 5668 (1998).

[36] X. Y. Li, Q. Pan, J. T. Jing, J. Zhang, C. D. Xie, and K. C. Peng, "Quantum dense coding exploiting bright Einstein-Podolsky-Rosen beams" Phys. Rev. Lett. **88**, 047904 (2002)

[37] T. C. Ralph. "Continuous Variables Quantum Cryptography" Phys. Rev. A, **61** 010303 (2000).

[38] M. Hillery. "Quantum Cryptography with Squeezed States" Phys. Rev. A, **61** 022309 (2000).

[39] S. F. Pereira, Z. Y. Ou, H. J. Kimble. "Quantum Communication with Correlated nonclassical States." Phys. Rev.A **62** 042311 (2001).

[40] L.Mandel, E.Wolf "*Optical coherence and Quantum Optics*" Cambridge University Press (1995).

[41] J. Lee, M.S. Kim, and H. Jeong, "Transfer of non classical features in quantum teleportation via a mixed quantum channel" Phys. Rev. A **62**, 032305 (2000); D. Wilson, J. Lee, and M.S. Kim, quant-ph/0206197;

[42] J. S. Prauzner-Bechcicki, J. Phys. A **37**, L173 (2004);

[43] S. Olivares, M. G. A. Paris, A. R. Rossi, Phys. Lett. A **319**, 32 (2003); A. R. Rossi, S. Olivares, and M. G. A. Paris, J. Mod. Opt. **51**, 1057 (2004);

[44] A. Serafini, F. Illuminati, M. G. A. Paris, S. De Siena,"Entanglement and purity of two modes gaussian states in noisy channels" Phys. Rev A **69**, 022318 (2004);

[45] M. G. A. Paris, A. Serafini, F. Illuminati, S. De Siena, "Purity of gaussian states measurements scheme and time evolution in noisy channels" Phys. Rev. A **68**, 012314 (2003);

[46] A. Serafini, M. G. A. Paris, F. Illuminati, S. De Siena, J. Opt. B **7**, R19-R36 (2005).

[47] V. D'Auria, A. Porzio, S. Solimeno, S. Olivares and M.G.A. Paris, "Characterization of bipartite states using a single homodyne detector", Journ. Opt. B. Opt. **7,** S750 (2005).

[48] John D. Bierlein, and Herman Vanherzeele. "Potassium tytanil phosphate: properties and new applications" J. Opt. Soc. Am. B, **6** 622 (1989)

[49] S. Feng, O. Pfister, "Quantum interference of ultrastable twin optical beams", Phys. Rev. Lett., 203601 (2004)

[50] Martin M. Feger, G. A. Magel, Dieter H. Jundt and Robert L. Byer, "Quasi-phase-matched second armonic generation: tuning and tolerances", **28**, 2631 (1992)

[51] M. O. Scully, M. S. Zubairy "Quantum Optics" Cambridge University Press (1997);

[52] B.L. Schumaker, "Quantum Mechanical Pure States with Gaussian Wave Functions", Phys. Rep. **135**, 317 (1986)

[53] R.Graham, H.Haken, "The Quantum Fluctuations of the Optical Parametric Oscillator. I", Zeitschrift für Physik, **210,** 276 (1968);

[54] P. Marian, "Higher-order squeezing and photon statistics for squeezed thermal states", Phys. Rev. A, **45**, 2044 (1992);

[55] U.Leonhard, M.Munroe, T.Kiss, T.Richter , M.G.Raymer, "Sampling of photon statistics and density matrix using homodyne detection" Opt. Comm. **127** 144 (1996)

[56] G.M. D'Ariano, "Homodyning as universal detection", **arXiv:quant-ph/9701011 v2** (1998);

[57] G.M. D'Ariano, M.G.A. Paris, "Added noise in homodyne measurement of field observables", Phys. Lett. A **233** 49 (1993);

[58] G.M. DAriano and M.G. A. Paris, "Adaptive quantum homodyne tomography", Phys Rev A **60** 518 (1998).

[59] G. Boyd and D. Kleinman, "Parametric interaction of focused gaussian light beams", Journ. Appl. Phys. **39** 3597 (1968);

[60] Robert C. Eckardt, C. D. Nabors, William J. Kozlovky, Robert L. Byer;"Optical parametric oscillator frequency tuning and control", J. Opt. Soc. Am. B **8**, 646 (1991)

[61] J. A. Giordmaine and R. C. Miller, "Tunable coherent parametric oscillation in $LiNbO_3$ at optical frequencies" Phys. Rev. Lett. **14**, 973 (1965)

[62] Hans-A. Bachor "A Guide to Experiment in Quantum Optics" Wiley-VCH, (1998)

[63] R. Drever, J. Hall, F. Kovalski, J. Hough, G. Ford, A. Munley, and H. Ward. "Laser phase and frequency stabilization using an optical resonator" Appl. Phys. B **31** 97 (1983);

[64] Breitenbach G. e Schiller "Homodyne Tomography of Classical and non Classical light" Journ. Mod. Opt. **44** 2207 (1997).

[65] K. Yosida, "Functional Analysis", Springer-Verlag, Berlin (New York) (1988)

[66] V. D'Auria, C. De Lisio, A. Porzio, S. Solimeno, M. Paris "Effects of pump and cavity fluctuations on the statistics of OPO fields" (*in preparation*)

[67] V. V. Dodonov, O. V. Manko, V. I. Manko, "Photon distribution for one-mode mixed light with a generic Gaussian Wigner function", Phys. Rev. A, **49**, 2993 (1994);

[68] Y.Zhang, H.Su, C.Xie, K.Peng, "Quantum variances and squeezing of the output field from NOPA", Phys. Lett. A, **259**, 171 (1999);

[69] F.E. Harrison, D.F. Walls, "QND measurement of intensity difference fluctuations", Opt. Comm., **123**, 331 (1996)

[70] K.Fradkin et al., "Tunable midinfrared source by difference frequency generation in bulk periodically poled KTiOPO4", App. Phys. B, **74,** 914 (1999)

[71] Antonino Chiummo,"Quantum and Classical Features of Optical Parametric Oscillators in Continuous Wave regime", PhD thesis (2005)